Capacitive Spatial Exteroception in Minimally Invasive Continuum Robots

Zur Erlangung des akademischen Grades eines

Doktors der Ingenieurwissenschaften

von der KIT-Fakultät für Informatik
des Karlsruher Instituts für Technologie (KIT)

genehmigte

Dissertation

von

Carl Christian Marzi

Tag der mündlichen Prüfung:	24. Juli 2024
1. Referentin:	Prof. Dr. Franziska Mathis-Ullrich
2. Referent:	Prof. Dr.-Ing. Tamim Asfour

KIT Department of Informatics
Karlsruhe Institute of Technology
Am Fasanengarten 5
76131 Karlsruhe

DOI: 10.5445/IR/1000175268.

Bei der Arbeit an dieser Dissertation konnte ich mich zu jeder Zeit auf die Unterstützung meiner Familie und meiner Freunde verlassen. So selbstverständlich das klingt, hat diese Arbeit mir das Glück, welches ich damit habe, besonders aufgezeigt.

Das erfolgreiche Abschließen dieser Arbeit wurde möglich gemacht durch die sehr gut ausbalacierte Betreuung meiner Doktormutter Franziska Mathis-Ullrich. Sie gab mir Raum und Mittel diese Arbeiten durchzuführen, stand für Feedback und Rat zur Verfügung und half mit Nachdruck wo nötig.

Danke euch für diese Unterstützung!

Abstract

Capacitive Spatial Exteroception in Minimally Invasive Continuum Robots

Minimally invasive interventions contribute essentially to the reduction of perioperative trauma in modern therapy and diagnostics. Such an intervention reduces the injury afflicted to healthy tissue and allows the patient a faster recovery. Despite their benefits for the patient, clinicians are challenged with the drawbacks entailed in such interventions: Direct line of sight is not available anymore, and manipulation of tissue is impeded as the access to the situs and the dexterity of the utilized tools is restricted. Robotic surgery offers the possibility to counteract these drawbacks by providing actuated instruments with the ability to restore and extend the surgeon's capability to manipulate tissue inside the body of the patient. Robotic systems could already be established in fields of surgery, in which the situs can be accessed on linear trajectories. For more complex interventions deeper in the body, linear trajectories can be impractical. Therefore, research investigates the application of continuum robots for minimally invasive procedures. Continuum robots allow for non-linear access and high dexterity at the distal part of the instrument or robot. Pure telemanipulation of such highly actuated systems would confront surgeons with yet another challenge of complex steering and further increase the required learning curve. Therefore, automation of such robotic systems is required and in the focus of research.

For the automation of minimally invasive robotic systems, spatial information is crucial. Only such information allows a robot to interact with or avoid the minimally invasive environment it is enclosed in. Thus, robotic systems require suitable sensing modalities which enable them to be controlled safely. This thesis investigates the application of capacitive sensing for the in situ acquisition of spatial information in continuum robots and the utilization of such information to leverage the automation of diagnostic and therapeutic interventions. Thereby, the thesis aims to answer the question of how capacitive spatial sensing can be utilized in a closed-loop controlled system for automation in minimally invasive interventions.

To investigate this question, a novel robotic system is developed that meets the requirements for an application in endoscopy as an example of a minimally invasive context. As a second contribution, a method to apply capacitive sensing in a minimally invasive intervention is investigated. The resulting sensor is capable of deriving localization information and providing it to a surgeon or an automated system. As a third method, the sensor and the robotic system are combined in a joint setup and a method for proximity control is presented. Such an endoscopic controlled system is evaluated for its capability to center itself in a hollow organ. Such a capability could be applied to provide a robotic endoscope with an optimized view and to reduce the risk of injuring sensible tissue.

The continuum robot presented in this work provides a small footprint and minimizes the number of motors through a novel antagonistic actuation. In a position accuracy evaluation, it

demonstrated a maximum error of 1.8 % of its length. The developed sensor could provide centering information with an average accuracy of up to (7.2 ± 3.2) % of the environment's radius. Integrated into the robot, the closed-loop controlled system could demonstrate an average error of (9.62 ± 0.38) mm in a dynamic evaluation and prohibited contact with the environment up to 98 % of the experiment time.

The presented methods still offer challenges in improving their accuracy. Therefore future investigations should research the optimization of the hardware setup and the calibration of the robot and the sensor. For a transfer to the clinic and in vivo studies, the behavior of the sensor in the presence of humidity must be further investigated. With such challenges addressed, these three presented contributions: The continuum robotic system, the capacitive proximity sensor, and the proximity control algorithm can be applied in minimally invasive surgery and support a minimally invasive intervention through automation. The resulting capabilities could improve the work of clinicians and benefit patient outcome.

Keywords: *Continuum Robot, Minimally Invasive, Proximity, Sensor, Endoscopy, Capacitive Sensing, Control*

Zusammenfassung

Kapazitive Räumliche Exterozeption in Minimalinvasiven Continuumrobotern

Minimalinvasive Eingriffe tragen wesentlich zur Verringerung des perioperativen Traumas in moderner Therapie und Diagnostik bei. Eine solche Intervention reduziert Verletzung von gesundem Gewebe und ermöglicht dem Patienten eine schnellere Genesung. Trotz ihrer Vorteile für den Patienten, sind Ärzte mit den Nachteilen solcher Eingriffe konfrontiert: Die direkte Sicht auf den Situs ist nicht mehr gegeben, und die Manipulation von Gewebe ist erschwert, da der Zugang zum Situs und die Beweglichkeit der verwendeten Werkzeuge begrenzt sind. Die robotergestützte Chirurgie bietet die Möglichkeit, diesen Nachteilen entgegenzuwirken, indem sie aktuierte Instrumente zur Verfügung stellt, welche die Möglichkeit des Chirurgen, Gewebe im Körper des Patienten zu manipulieren, wiederherstellen und erweitern können. Robotersysteme konnten bereits in Bereichen der Chirurgie etabliert werden, in denen der Situs über einen linearen Zugang erreicht werden kann. Für komplexere Eingriffe, tiefer im Körper sind lineare Zugänge jedoch oft nicht realisierbar. Daher untersucht die Forschung den Einsatz von Kontinuumsrobotern für minimalinvasive Eingriffe. Kontinuumsroboter ermöglichen einen nichtlinearen Zugang und eine hohe Bewegungsfreiheit am distalen Ende des Instruments oder Roboters. Reine Telemanipulation solcher hochgradig aktuierten Systeme, würde Chirurgen jedoch vor die zusätzliche Herausforderung der komplexen Steuerung stellen und die benötigte Lernkurve noch weiter erhöhen. Daher ist die Automatisierung solcher robotergestützten Systeme erforderlich und Schwerpunkt von Forschung.

Für die Automatisierung minimalinvasiver robotergestützter Systeme sind räumliche Informationen essentiell. Nur solche Informationen ermöglichen es einem Roboter, mit der minimalinvasiven Umgebung, in der er sich befindet, zu interagieren oder ihr auszuweichen. Daher benötigen robotergestützte Systeme passende Sensormodalitäten, die eine sichere Bewegung möglich machen. Diese Arbeit untersucht den Einsatz von kapazitiver Sensorik zur in situ Erfassung von räumlichen Informationen in Kontinuumrobotern und die Nutzung solcher Informationen zur weiteren Automatisierung diagnostischer und therapeutischer Eingriffe. Dabei zielt die Arbeit darauf ab, die Frage zu beantworten, wie kapazitive, räumliche Sensorik in einem geregelten System für die Automatisierung in minimalinvasiven Eingriffen genutzt werden kann.

Um diese Frage zu untersuchen, wird ein neuartiges robotisches System entwickelt, das die Anforderungen für eine Anwendung in der Endoskopie, als Beispiel für einen minimalinvasiven Kontext, erfüllt. Als zweiter wissenschaftlicher Beitrag wird eine Methode zur Anwendung kapazitiver Sensorik in einem minimalinvasiven Eingriff untersucht. Der resultierende Sensor ist in der Lage, Lokalisierungsinformationen abzuleiten und sie einem Chirurgen oder einem automatisierten System bereitzustellen. Als dritte Methode werden der Sensor und das robotische System in einem gemeinsamen Aufbau kombiniert und eine Methode zur Näherungs-Regelung vorgestellt. Das so geregelte, endoskopische System wird bezüglich seiner Fähigkeit evaluiert,

sich in einem Hohlorgan zu zentrieren. Eine solche Fähigkeit könnte angewendet werden, um den Sichtbereich eines robotischen Endoskops zu optimieren und das Risiko für die Verletzung empfindlicher Gewebe durch Kontakt zu reduzieren.

Der in dieser Arbeit präsentierte Kontinuumsroboter weist einen kleinen Footprint auf und minimiert die Anzahl der Motoren durch eine neuartige antagonistische Aktuierung. In einer Evaluierung der Positioniergenauigkeit zeigte er einen maximalen Fehler von 1.7 % seiner Länge. Der entwickelte Sensor konnte Zentrierungsinformationen mit einer durchschnittlichen Genauigkeit von bis zu (7.2 ± 3.2) % des Radius der Umgebung liefern. In den Roboter integriert, konnte das geregelte System in einer dynamischen Evaluierung einen durchschnittlichen Fehler von (9.62 ± 0.38) mm nachweisen und den Kontakt mit der Umgebung während bis zu 98 % der Versuchsdauer verhindern.

Die vorgestellten Methoden bieten weiterhin Herausforderungen zur Verbesserung ihrer Genauigkeit. Daher sollte zukünftige Forschung die Optimierung des Hardwareaufbaus und die Kalibrierung des Roboters und des Sensors untersuchen. Für einen Transfer in die Klinik und zu in vivo Studien muss das Verhalten des Sensors in Anwesenheit von Feuchtigkeit weiter untersucht werden. Mit der Adressierung solcher Herausforderungen können die drei präsentierten Beiträge: Der Kontinuumsroboter, der kapazitive Näherungssensor und der Algorithmus zur Näherungsregelung in der minimalinvasiven Chirurgie angewendet werden und einen minimalinvasiven Eingriff durch Automatisierung unterstützen. Die resultierenden Fähigkeiten können die Arbeit von Ärzten erleichtern und das Outcome für den Patienten verbessern.

Stichwörter: *Kontinuumroboter, Minimalinvasiv, Näherung, Sensorik, Endoskopie, Kapazitive Sensorik, Regelung*

Contents

1 Introduction

This thesis investigates the integration of capacitive exteroception into a novel minimally invasive continuum robot to evaluate the benefits of such a combination for automation in minimally invasive surgery.

To motivate this investigation, the following chapter introduces the need for such a system and lists the problems that the approach aims to address. Section 1.2 introduces the derived research questions, followed by a look ahead at the contributions to the field of research provided by this thesis. Section 1.4 shortly introduces the structure of this thesis.

1.1 Motivation

To improve patient outcome and recovery time, modern medicine applies concepts of minimally invasive surgery (MIS) wherever possible. Robotic surgery offers the potential to fundamentally support and push this development [1, 2]. To reach deeper regions in the patient's body, on non-linear, less invasive access trajectories, flexible instruments are already applied and their automation is investigated [3, 4]. MIS benefits the patient in terms of less injury to healthy tissue, faster recovery time, and better long-term outcome. For surgeons and medical staff, however, MIS brings additional challenges [5]:

1. **Reachability** is lowered by accessing the situs through narrow passages and channels. Healthy organs can obstruct the direct line of sight and restrict access with tools.
2. Instruments become more complex, their operation more challenging and their usage requires a longer learning phase. The **cognitive and physiological load** on the surgeon increases, ergonomy is decreased and often more staff and time is needed for an intervention.
3. **Perception** at the situs is restricted. Endoscopic images provide a limited field of view, sense of touch is only possible through instruments, and therefore, less reliable or not available at all.

Medical engineering addresses these challenges through the advancement of technical features in medical instrumentation. Research on flexible instruments aims to address point 1: In contrast to conventional rigid instruments, flexible instruments can bypass critical anatomical structures, located in the direct line of sight, provide more freedom in the direction from which the situs can be accessed, and increase the maneuverability to operate at the situs.

However, flexible instruments amplify point 2: They are harder to control and result in an even higher load and strain for the surgeon and her team. This can be counteracted with the automation of instrument actuation. Instead of manual control, instruments are equipped with electrically controlled actuators, and control input from the surgeon is input through ergonomic

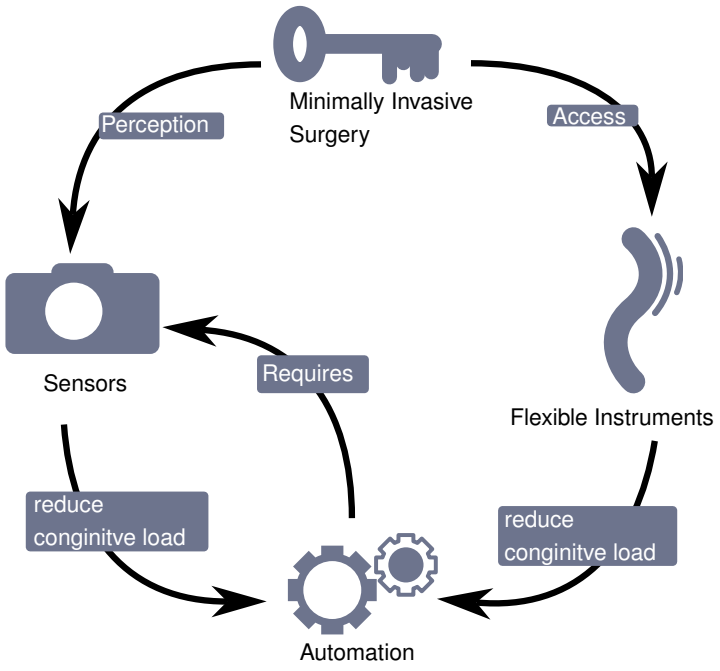

Figure 1.1 – Illustration of dependence matrix for challenges in minimally invasive surgery.

consoles or gamepad-like controllers. In this way, surgical robotics is established in the operation room (OR) [6, 7]. The combination of point 1 and point 2 leads to the conclusion that such robotic systems must not only consist of automated rigid instruments and highlights the need for continuum robotic systems. As is shown in Section 3.1.2, surgical robots with rigid instruments are well-established in modern surgery. Continuum robotic systems, however, are still in focus of research.

Point 3 can be addressed by integrating in situ sensors into a minimally invasive instrument. Through them, perception of the situs can be translated from the distal part of an instrument to the surgeon. Furthermore, digitized information from the situs can serve for documentation and will be of increasing interest for the rising demand for information from data-driven methods, in diagnostics and therapeutic methods [2]. But not only surgeons will benefit from sensing integrated into a minimally invasive system. For an aforementioned minimally invasive continuum robot, such sensor feedback will also provide valuable information required for the control of these robotic systems.

Figure 1.1 visualizes the dependencies of MIS and automation. The challenges of MIS require flexible instruments and in situ sensing. The resulting increased cognitive load can be addressed by automation in surgery.

In summary, to address the three mentioned challenges of minimally invasive surgery, a sensorized continuum robot, equipped with skills to gather spatial information at the situs, is of essential benefit. Even though a lot of research is conducted in this field, combined systems focusing on both, sensory and actuation aspects, and showing how this can be leveraged for automation in MIS are very rare (as will be presented in Chapter 3).

The aim of this thesis is to elaborate methods for setup and control of a continuum robot with integrated exteroceptive sensing, for automation in MIS. This work investigates the potential of capacitive sensing for the acquisition and utilization of spatial exteroceptive information. The integration of sensing modalities at the very situs in a minimally invasive setting is challenged by strict spatial requirements made for minimally invasive instruments and by the

demanding environment of surgery. In this thesis, capacitive sensing is explored as a candidate for exteroceptive sensing, offering space-saving and flexible integration as well as facile yet versatile sensing modalities [8].

1.2 Research Questions

Based on the current research challenges of MIS described above, this thesis addresses the following superordinate research question:

Superordinate Research Question:

How can capacitive sensing and continuum robotics form a closed loop controlled system, which can utilize the capacitive sensing as exteroceptive input for automation in MIS?

Three subordinated questions are derived from the main research question. As a base for sensor integration, a robotic platform is required. As motivated above, a continuum robotic system allows to leverage the advantages of a flexible body to provide distal dexterity. Still, such a robotic setup is subject to research. In a first approach, this thesis will therefore investigate the following question:

Research Question Q1:

How can a continuum robotic platform be designed to be suitable for minimally invasive interventions but also fulfill requirements for sensor integration and sensor-based control?

Capacitive sensing is applied in various fields in an industrial context. In medical interventions, its application is limited to closed sensor systems such as force sensors. In such a context, methods for proximity sensing are not yet researched. Thus, this thesis aims to provide an answer to the question:

Research Question Q2:

How can capacitive sensing be applied to provide exteroceptive information such as proximity and contact to a minimally invasive instrument or a robotic system?

The first two research questions approach the standalone challenges for the realization of actuation and sensorization. Yet, to combine both and create a closed-loop controlled system, this thesis further investigates the question:

Research Question Q3:

How can capacitive sensing and a continuum robot control be integrated into closed-loop control, and how can a method for controlling such a system be formulated?

In this thesis, one chapter is dedicated to each of these questions. The methods developed in Chapter 4, 5, and 6 each focus on one of these sub-questions and contribute the answers to the respective field of research as an extension of the state of the art.

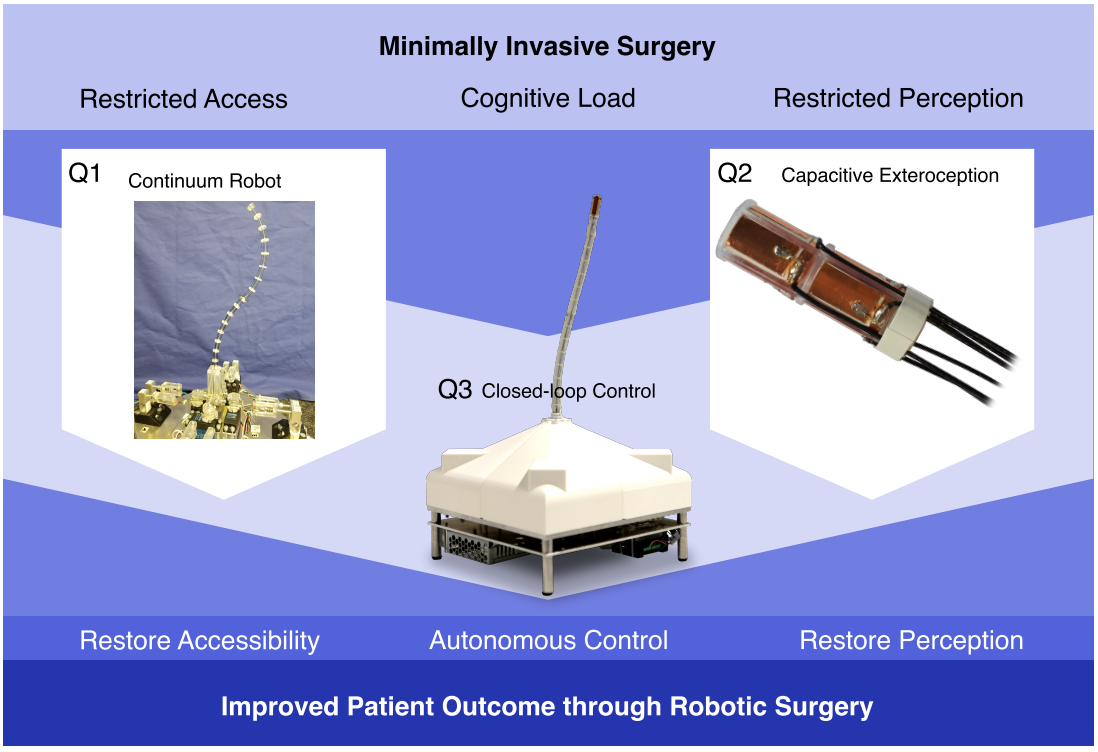

Figure 1.2 – Summarizing illustration of the research questions and contributions of this thesis. This thesis contributes a tendon-driven continuum robot (CR), a sensor for in situ capacitive spatial sensing, and, as a combination of both, a closed-loop controlled endoscopic continuum robot.

1.3 Contributions

The field of research, this thesis contributes to, is sensing and control for the autonomy of MIS. In this field, spatial information is mostly derived solely from image-based modalities. This thesis contributes a method for the design and control of a continuum robotic system, which integrates capacitive exteroception and can center itself in a dynamic environment of a minimally invasive intervention. Corresponding to the research questions, the overall contribution can be divided into contributions for spatial sensing in minimally invasive surgery, continuum robot design, and closed-loop control of continuum robots:

An Antagonistically Actuated Continuum Robot In the field of continuum robot design, a novel antagonistic principle for tendon actuation is presented and published in [9]. The design minimizes the number of motors required and provides a four degrees of freedom (DOFs) continuum robotic setup with tendon force feedback on a small footprint. It offers a continuum robotic body, sufficiently long and thin for minimally invasive interventions, such as colonoscopy. The system serves as a research platform for continuum robotic applications in minimally invasive surgery.

Published in [9]:

C. **Marzi**, F. Buck, and F. Mathis-Ullrich. "Continuum Robot Actuation by a Single Motor per Antagonistic Tendon Pair: Workspace and Repeatability Analysis". In: *at - Automatisierungstechnik* 71.7 (2023), pp. 528–536. DOI: 10.1515/auto-2023-0066. URL: https://doi.org/10.1515/auto-2023-0066

A Proximity Sensor for Minimally Invasive Procedures The developed method for exteroceptive proximity sensing contributes to the field of sensing in MIS. In this field of research, means for distal distance measurement are rare, rely on external imaging, or are restricted to a front-facing field of view. Through the applied capacitive proximity sensing, a sensor is presented that features the low integration volume required for application in minimally invasive instruments and robots. The method for sensor setup and the processing of the sensor data for localization information in a minimally invasive scenario is published in [10]. To demonstrate the in vivo applicability and versatility of the sensing principle, it was applied to a contact sensor which was integrated into a magnetic flexible endoscope. This integrated system was evaluated in an in vivo trial [11].

Published in [10, 11]:

C. **Marzi**, H. Alagi, O. Rau, J. Hampe, J. G. Korvink, B. Hein, and F. Mathis-Ullrich. "Capacitive Proximity Sensor for Non-Contact Endoscope Localization". In: *2022 International Conference on Robotics and Automation (ICRA)*. May 2022, pp. 9614–9620. DOI: 10.1109/ICRA46639.2022.9811734

N. Greenidge, J. Martin, C. **Marzi**, D. Chathuranga, B. Scaglioni, K. L. Obstein, F. Mathis-Ullrich, and P. Valdastri. "Restoring the Sixth Degree of Freedom in the Robotic Manipulation of Mesoscale Magnetic Devices Using the Oloid Shape". In: *IEEE Robotics and Automation Letters* (2024). Currently prepared for publication.

A Proximity Controlled Endoscopic Continuum Robot The third contribution is a control method, that brings together both previously presented contributions. The sensor's localization information is used as control input for a centering controller. This controller applies a continuum robot model and inverse kinematics to calculate motor commands for robot control. Applied to the continuum robotic setup, an endoscopic system can be demonstrated, which is equipped with the ability to center itself autonomously in a dynamic minimally invasive environment [12].

Published in [12]:

C. **Marzi**, M. Themistocli, B. Hein, and F. Mathis-Ullrich. "Proximity Servoed Minimally Invasive Continuum Robot for Endoscopic Interventions". In: *IEEE Transactions on Medical Robotics and Bionics* (2024), pp. 1–1. DOI: 10.1109/TMRB.2024.3464127

Combined, these contributions aim to reduce the restrictions of access and perception in minimally invasive surgery and leverage new robots that could reduce the cognitive load surgeons are exposed to. Figure 1.2 summarizes the research questions and contributions graphically. These contributions broaden the range of spatial sensing and autonomy modalities, available for future surgical robots. The contributions focus on minimally invasive interventions to improve surgery for the surgeon and the patient.

1.4 Thesis Structure

Chapter 2 *"Medical Fundamentals"* aims to provide the reader with information to help get an insight into current clinical practice and to understand the clinical needs, addressed in this

thesis. Section 2.1 reports how minimally invasive procedures are currently conducted. On the one hand for surgical interventions in Section 2.1.1, and on the other hand for endoscopic interventions in Section 2.1.2. Section 2.2 reviews methods and imaging modalities for the acquisition of spatial information for orientation and navigation in MIS. Section 2.3 summarizes the chapter and points out the challenges of MIS interventions, addressed within this thesis.

Chapter 3 *"Medical Automation with Continuum Robots"* covers the fundamentals and technical state of the art, on which the presented methods are based and to which they can be compared. It provides insights into the three technical fields of research of this thesis: *Continuum Robots*, *Exteroceptive Sensing in Minimally Invasive Surgery*, and *Capacitive Sensing*. Section 3.1 *"Continuum Robots"* starts with an overview of the broad field of continuum robots and introduces characteristics and parameters for classifications (Section 3.1.1). The topic is then narrowed down to systems, relevant to the thesis' scope. The following sections give an overview of systems certified for use in clinical practice (Section 3.1.2). Afterwards, research on advanced methods and systems for application in medicine is presented (Section 3.1.3). Additionally, Section 3.1.4 provides an overview of the kinematic modeling and closed-loop control for automated continuum robotic systems. As a foundation for the sensory method of this thesis, Section 3.2 *"Exteroceptive Sensing in Minimally Invasive Surgery"* provides insight into the possibilities for spatial sensing at the situs in minimally invasive applications. Here, distance- (Section 3.2.1) and force-sensing (Section 3.2.2) are mainly regarded. Section 3.3 *"Capacitive Sensing"* concentrates on the fundamentals of capacitive sensing in general (Section 3.3.1) and presents research on its application in sensors for proximity and distance in Section 3.3.2, as well as contact and force in Section 3.3.3.

The following three chapters (Chapter 4 to 6) each present one of the main methods this thesis contributes to the field of research. The robot and sensor system are initially developed independently and then combined to allow for closed-loop control. Each chapter starts with a short introduction to review the problem the respective method addresses. In the end each chapter discusses the respective method in a concluding chapter discussion.

Chapter 4 *"Antagonistic Continuum Robot"* presents the design and evaluation of the robotic subsystem of this thesis. Its requirements are derived from the medical field of application (Section 4.2). On this basis, the robot's development and setup are reported in Section 4.3. To evaluate workspace and repeatability, experiments were conducted and are presented in Section 4.4.

Chapter 5 *"Capacitive In Situ Spatial Sensing"* introduces methods for two capacitive sensor types: One as an add-on sensor for proximity sensing in a minimally invasive instrument or robot (Section 5.2). The other is a multi-contact sensor, integrated into a magnetic capsule robot (Section 5.3). Both systems are evaluated experimentally, the proximity sensor in a phantom experiment, and the contact sensor in an animal trial.

For the combination of sensor and robot, Chapter 6 *"Proximity Controlled Continuum Robot"* first introduces necessary adaptions to the sensor and robot hardware for the combination (Section 6.2), then the processing algorithm for sensor data and robot control is introduced in Section 6.3. The system was evaluated in a dynamic phantom setup, as reported in Section 6.4.

Chapter 7 *"Discussion"* reflects on the combined results and their consolidated significance in the fields of application (Section 7.1). Limitations are presented (Section 7.2) and the contributions and answers to the research questions are reviewed in Section 7.3

Finally, Chapter 8 *"Conclusion"* sums up the thesis' findings in a take-home message. Section 8.2 translates the identified limitations of the methods into possible working points for

optimization and presents thoughts and lessons learned for future investigations in this field of research.

2 Medical Fundamentals

The following chapter aims to explain the necessary medical fundamentals for a profound understanding of the technical challenges that this thesis addresses. It serves for defining terms in the areas of application and should help to relate to the situation in the OR, understanding the problem settings and challenges from the application's point of view.

2.1 Minimally Invasive Procedures in Medicine

Minimally invasive techniques in medical interventions aim to reduce the patient's trauma. The following chapters highlight the application of such techniques in surgery and diagnostic interventions. This section addresses medical practice, therefore focus is laid on systems with approval by notified bodies such as Conformité Européenne (CE) or Food and Drug Administration (FDA), or recent developments from established manufacturers are addressed. Systems developed by research labs in earlier stages of evaluation are presented under technical aspects in Section 3.1.2 *Continuum Robots in the Clinic*.

2.1.1 Minimally Invasive Surgery

Minimally invasive surgery (MIS), often also called keyhole surgery, is a class of surgical procedures that are united by the approach of reducing the number or length of incisions in the epithelia of a patient. This is in contrast to open surgery, where the skin and overlaying tissue are moved aside to lay open the full extent of the surgical situs and gain a direct line of sight. Open surgery requires such large incisions to provide the surgeon with sufficient view and workspace on pathological organs and tissue. To be able to reduce this open space, MIS requires specialized instruments, which enable accessing the situs through an incision of a few millimeter length. In most cases, one such instrument is an endoscopic device, serving to overcome the occluded line of sight to the situs, by incorporating distal optics and providing an image of the situs to the instrument's proximal end (see Section 2.1.2 for details). To enable manipulation, instruments such as forceps, electrocauters, and graspers are designed to incorporate a long, narrow shaft transferring the motion or energy from a handpiece to a miniaturized end-effector [13].

Figure 2.1 shows exemplary laparoscopic tools a) and a flexible gastroscope b). Their design aims to use natural orifices or only small incisions of 3 mm to 12 mm length to insert the instrument. In a typical laparoscopic intervention, the operating surgeon bi-manually operates two instruments such as graspers and scissors while an assistant coordinates endoscope placement [14, 15].

To further reduce the access trauma, a subclass of MIS, Natural Orifices Translumenal Endoscopic Surgery (NOTES) aims to access natural openings of the body, such as the mouth,

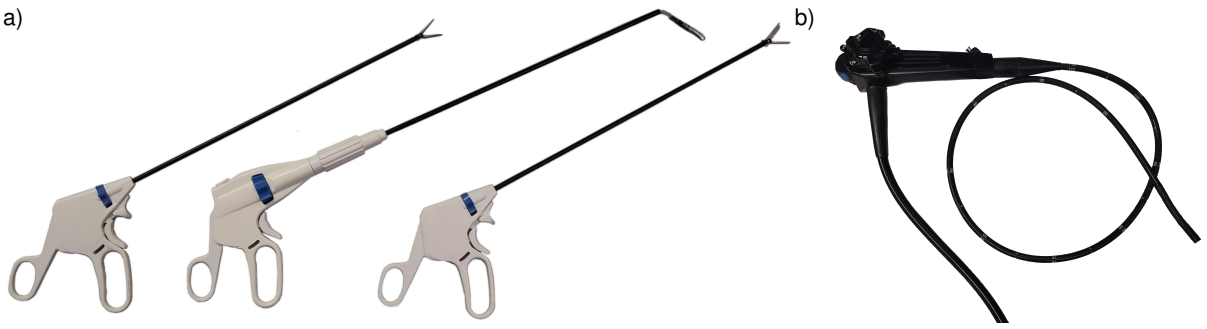

Figure 2.1 – a) Examples of laparoscopic instruments. b) A flexible gastroscope.

urethra, anus, or vagina, to get as close to the situs as possible before penetrating tissue. This way, only a minimal working channel through healthy tissue is required for surgery, and trauma is minimized [16].

Another method of MIS overcomes the restricted view through fluoroscopy. This can be applied in interventions where the situs is located at a structure that is well visible in fluoroscopy, such as spine surgery [17]. Another application is given by cardiovascular surgery, where contrast agents can visualize the vessel structure. Here, minimally invasive interventions comprise the usage of catheters and guidewires. Typical interventions are the treatment of aneurysms (i.e., widening of a blood vessel with risk of rupture) or atherosclerosis (i.e., accumulation of plaque with impeded blood flow and risk of a stroke). Here, wire-guided catheters are inserted into the body and navigated to the situs while fluoroscopic imaging provides position feedback. When the catheter has reached the situs, it can be used to introduce tools for treatment such as stents or balloons [18, 19].

The primary advantages of MIS are reduced trauma to the skin and organs, as well as reduced loss of blood during surgery. As a result, time to recovery and pain management can be improved significantly. As fewer inner organs are openly exposed, the risk of surgical site infections is also reduced. For the patient, smaller scars result in improved cosmesis after surgery. The faster recovery time even allows the use of outpatient laparoscopic interventions (i.e., a patient can leave the hospital on the same day as the intervention) [13].

While it brings benefits for the patient outcome, MIS also comes with additional challenges. The requirement of less injury often results in specialized instrumentation which requires complex handling and additional training. This afflicts medical apprentices with additional cognitive load and more training before being able to conduct such interventions. But also experienced surgeons are exposed to more challenging interventions and uncomfortable postures required for instrument handling. The latter also causes the risk for surgeons to suffer from strain injury when practicing surgery [14]. The additional complexity often also comes with minimally invasive interventions to typically take longer than an equivalent open surgery. This increases costs and reduces personnel availability. Lastly, the surgeon loses direct haptic feedback of the situs, as contact forces can only be felt as transferred through the instruments. Haptic feedback can be crucial for some interventions, such as cancer treatment, where the surgeon can differentiate malignant tissue from healthy tissue by perceiving its elasticity. But also in cases where tissue haptics do not play a primary role, it is regarded as relevant for surgeons' orientation [5, 20].

Nevertheless, the combined effort of advancements in medical practice and research, as well as medical instrument engineering has helped MIS to completely replace open surgery in some standard applications [13]. MIS can be applied in various fields of surgery and has become a standard procedure in fields such as general surgery, gynecology, urology, and cardiothoracic

surgery [5]. For many other fields of surgery, minimally invasive methods are established as well and are further investigated and evaluated. The tendency to convert further interventions to MIS continues.

This also led to the establishment of robotic systems into the clinical daily routine [1, 21]. The most widespread robotic system in clinical practice is Intuitive Surgical's Multiport Surgical System *da Vinci* [22], with approximately 1,875,000 surgical procedures performed in 2022 [23]. Its major use case is laparoscopic surgery, such as cholecystectomy. It consists of up to four robotic arms on a patient cart. Each arm holds a laparoscopic instrument and is inserted into the patient's body through a separated port, restricting its motion to a remote center of motion (RCM). To gain manipulability inside the body, its distal tips incorporate cable-driven *wrists*, which allow for deflection in 2 DOFs. Similar systems - also approved for surgery - are available as well, but not yet represented in clinics in likewise numbers: *REVO-I*, a robotic system by the South Korean Meere Company, also comprises a robotic cart with multiple arms and is approved for by the South Korena FDA [22], Avateramedical's *Avatera platform* was CE-approved in 2019, and Medicaroid Corporation's *Hinotori system*, which has been filed for approval in Japan in 2023. Also, Johnson & Johnson has announced a OR-table mounted robot system *Ottava* with up to six arms [24].

Other systems deviate from the single cart approach and install each robotic instrument on its separate robotic cart, which allows for more flexibility for placement and modularity. Examples of such systems are Medtronic's *Hugo RAS*, which gained CE approval in 2021 [1, 24] (former project name *Einstein* [25]), the *Senhance* Surgical Robotic System by TransEnterix, with CE and FDA approval in 2016 [1], and Cambridge Medical Robotics Ltd's *Versius Robot* (UK) [1, 25].

2.1.2 Gastrointestinal Endoscopy

Endoscopy denominates the usage of thin tube-like imaging instruments with optics at their distal tip, to transfer the situs' image to their proximal end. Such instruments allow to be inserted through a small opening in a patient's body, and can often be moved inside the body to depict various parts of the situs. Consequently, endoscopes play a crucial role in almost all minimally invasive surgical interventions. Due to its visualization capabilities, endoscopes also find a wide range of applications not only in surgical but also in diagnostic interventions. The following paragraphs will highlight the most common fields of application and point out their clinical needs and requirements.

Gastrointestinal endoscopy is the endoscopic examination of the digestive tract. Due to the soft and complex nature of its hollow organs, flexible instruments are required to navigate. Gastrointestinal endoscopy can be divided into upper and lower gastrointestinal endoscopy. Its fields of application and concerned anatomy are depicted in Figure 2.2. In upper gastrointestinal surgery, access is gained through the mouth and it serves for examination of the esophagus, stomach, and duodenum (Esophago-gastro-duodenoscopy (EDG)). In lower gastrointestinal endoscopy the anus is used for access and it serves for the examination of the rectum and colon (i.e., colonoscopy).

Typical indications for gastrointestinal endoscopy are suspicion of lesions in the mucosa or adenoma surveillance for cancer screenings. Before the intervention, the patient is required to be fasting and laxatives can be administered to ensure the bowels are emptied. Additionally, in special cases, (e.g. constipation) an *enema* can be conducted. Therefore, water is injected into

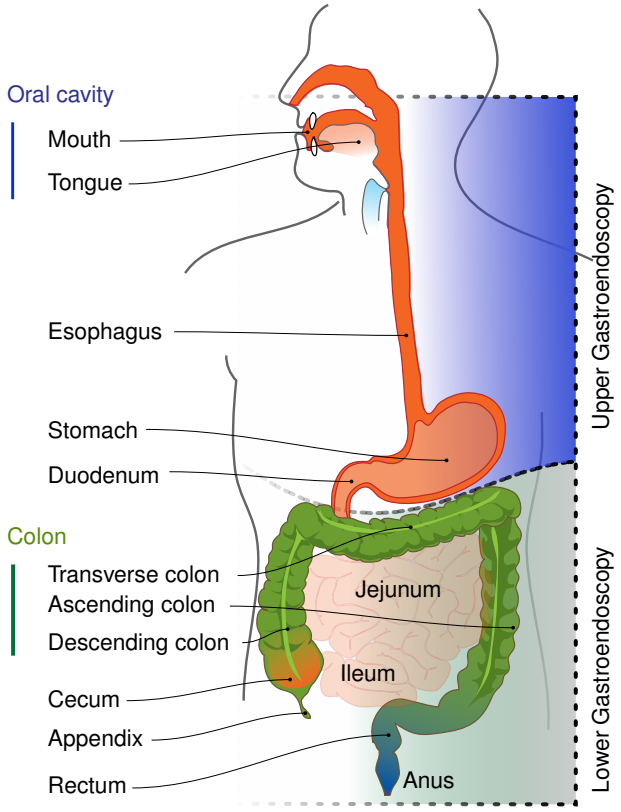

Figure 2.2 – Fields of application for endoscopic interventions in the gastric tract. Based on the examined organs, the mouth (upper gastroendoscopy) or the anus (lower gastroendoscopy) is used for access.

the colon to flush out residual waste. To improve motion and vision, the colon is inflated with CO_2 in colonoscopies. The complication rate of colonoscopies is very low, as shown by the rate of 0.058 % for serious complications in colorectal cancer screenings in Germany from 2003 to 2008 [26].

Gastroendoscope Design To illustrate the current design and features of contemporary flexible endoscopic devices, the following paragraph summarizes the evolution of flexible gastroendoscopes and their current form in medical practice. Typical gastrointestinal endoscopes comprise a flexible body. For advancement and adoption of the field of view, the tip can often be deflected via Bowden cables. Rotation and insertion are performed manually, using control wheels at the instrument's proximal handpiece. Due to its flexible body, rigid optics, as they were used in early straight endoscopic devices, can only be used to a very limited extent [27]. To overcome this issue, in the 1950s, first devices were developed in which bundles of optical fibers were embedded in the endoscope [28]. Distal optics project the image onto the distal end of the fibers. The total inner reflection in each fiber transports color and intensity information of the distal image. At the proximal end of the fiber and the endoscope, this image is then projected onto an eyepiece or imaging chip (video endoscopy) [27]. This method however restricted the image resolution to the number of fibers incorporated. Furthermore, internal losses in the fiber and an overlaid pattern from the fiber shape reduce image quality in this approach. With the technological advancement in imaging hardware, camera size could be reduced sufficiently to be able to fully integrate the optics and imaging chip into the endoscope's distal tip. This is also referred to as *chip-on-the-tip* and the preferred imaging modality in recent flexible endoscopes, as it also provides more space along the instrument's body [29]. In a similar development, the first endoscopes utilized light guides to transport the light required for endoscopic imaging

from a proximal light source to the situs. In modern systems, the advancing development of light emitting diode (LED) technology allows to integrate miniaturized light sources directly into the endoscope's distal tip. These LEDs are now strong enough to provide sufficient illumination while minimizing dissipated heat, which could otherwise endanger the surrounding tissue. As not only a light source's dissipated heat can harm tissue but also the light energy required for imaging can lead to burns, recent gastroscopes incorporate adaptively controlled illumination that minimizes the light intensity for a given scene [30]. Most gastroscopes comprise additional channels: A smaller channel for insufflation or aspiration, as well as a larger working channel for additional diagnostic or therapeutic instrumentation [30, 31].

Auxiliary Features As the main task of gastrointestinal endoscopy is the screening of the colon's or stomach's mucosa, various supporting features can be integrated aiming to facilitate this task. As the colon wall exhibits strong folds, examination with a front-facing field of view holds the risk of missing obstructed adenomas. To reduce this risk gastroenterological endoscopes can incorporate balloons or "whiskers", helping with centering the tip of the endoscope and straightening folds of the colon, to allow for the best view of its surface. Such a system is EndoAid's EndoRings or the Endocuff VISION from Olympus [30, 32]. They feature elastic levers, attached to an endoscope's tip, which help flatten the folds and improve sight on the colon's wall. Further measures include the incorporation of specialized or additional optics, enhancing the field of view. For a maximized field of view, fisheye lenses [30] or additional cameras facing side- or backward [30] can be used. Other systems provide highly flexible distal sections allowing for 180° deflection at a small bending radius enabling them to "take a look back" [30].

To extend from purely visual diagnostics, gastroendoscopes can be equipped with specialized instruments and sensors such as Ultrasound (US) or Optical Coherence Tomography (OCT) for additional imaging modalities. Such modalities are for example biopsy needles, chromoendoscopy with or without combination with spray dyes to mark lesions [27, 29], fluorescence imaging [29], confocal laser endoscopy and endocytoscopy [30].

To improve ergonomics for the surgeon and facilitate the handling of endoscopes, robotic functions have been introduced into modern products and continue to be developed. Especially with the integration of therapeutic tools, instrument handling becomes too complex for manual steering. Thus, robotic, endoscopic systems are mostly teleoperated through a console or a handheld remote [29, 33, 34]. Details on such systems will be provided in Section 3.1.2 *Continuum Robots in the Clinic*.

Capsule Endoscopy For a complete overview of gastroenterological endoscopy, also capsule endoscopes need to be mentioned. As they are out of the scope of this work, only a brief overview and hints for continued reading are provided. Capsule endoscopy serves especially to examine deeper regions or the full length of the gastrointestinal tract. Systems can be classified in their capabilities of motion control: Many systems purely rely on passive locomotion from the intestines peristaltic (e.g., PillCam (Given Imaging, Israel), or EndoCapsule (Olympus Corporation, Japan)). Others allow for partial locomotion or reorientation, which can be externally [35, 36] or internally actuated [37, 38]. Images can be recorded on the capsule itself or transmitted wirelessly to a receiver outside of the body [39]. While some systems are still tethered for power supply and data interfaces (and are retracted after an intervention) [36, 40], others provide on-board power supply and wireless interfaces [37, 41]. Further information can be found in the reviews [33, 42, 43].

2.2 Sensing Modalities for Navigation in Endoscopy

For navigation in a minimally invasive intervention, surgeons require information on the spatial relations inside the patient's body. Based on such information, an endoscope is controlled and advanced. While the knowledge of the underlying anatomy is a key factor, the individual anatomy differs from patient to patient, especially for pathological tissue and organs. For this reason, most interventions are preceded by preoperative imaging, not only for diagnostic purposes but also for planning and navigation of the intervention.

Flouroscopy One of the most common imaging modalities used for navigation is fluoroscopy. X-rays are projected through the patient's body or body part onto a receptor screen. The rays are dampened depending on the tissue they pass and respectively create an image of the structure on the screen. As conventional X-ray can only provide a projected two-dimensional image of the anatomy, Computed Tomography (CT) enhances this imaging modality by taking multiple images from various directions and computing 3-dimensional or tomographic images. Soft tissue and bone strongly differ in their absorbance, which facilitates imaging of bone structure. To examine images of other organs, such as blood vessels or parts of the gastric tract, contrast agents such as barium sulfate or sodium methylglucamine diatrizoate can be applied [44, 45]. Depending on the application, they can be injected or administered orally. The respective organ is visualized in 2D or 3D and the images provide spatial information that allows for navigation of an endoscopic device. Fluoroscopy can also be applied intraoperatively. However, due to its ionizing radiation, exposure time for patients and medical staff is a crucial limiting factor. Therefore, it is mainly used in catheter interventions where endoscopic feedback is not feasible.

Magnetic Resonance Imaging Magnetic Resonance Imaging (MRI) is based on the magnetic excitation of atomic spins. The spin release response can be recorded and the signal be processed into a tomographic image. This imaging modality does not come with hazardous radiation, but it employs strong magnetic fields and consequently large setups. This limits the imaging modalities' availability due to economic and space factors and results in it being almost exclusively employed for preoperative imaging. Intraoperative use is also strongly inhibited by interference through metallic objects, such as would especially be the case for robotic systems [46].

Visual Imaging Intraoperatively, visual feedback is the most relevant source of information. In laparoscopic interventions, the abdomen is inflated with CO_2, creating a comparably large space to navigate and operate. Due to multiple instruments being in use, special attention needs to be given to collision avoidance. For camera guidance, good communication, and situation awareness play an essential role for surgeons and endoscopic assistants. The desired field of view strongly depends on the situation. It can be required to focus on details of the situs' tissue, one or multiple instruments, or on a large field of view to provide an overview of the whole situs. In diagnostic endoscopy, surgeons control the endoscope themselves, but camera control becomes more challenging due to the use of a flexible instrument and navigation through the soft tissue.

Haptics As through the use of MIS instruments, haptic feedback is dulled or lost completely, collisions are harder to detect and hold an increased risk. Especially in flexible endoscopy,

where almost no force from the instrument's distal tip can be transmitted to the surgeon, collision with the organ's wall can result in perforation [47]. Another risk in flexible endoscopy, i.e., endoscopy, is loop formation. As the surgeon follows the winding shape of the colon, the endoscope can take a looped shape. In such a shape, the inner tissue can be constricted by the endoscope, potentially damaging it. Therefore, research approaches investigate the loop-detection in flexible endoscopes [48]. An alternative method is the usage of inflatable balloons attached to the endoscope, which can serve for the reduction of risk of perforation, for locomotion, and an improved view on the colon wall [30, 49, 50].

2.3 Challenges in MIS and Endoscopy

Even though MIS has been established as the gold standard in many fields of modern surgery, open challenges and improvements are manifold. Surgeons still require a long learning phase to handle minimally invasive instruments. And even after training, success (e.g., polyp detection rate) correlates with the years of experience [51]. Conducting a minimally invasive intervention can afflict stress and fatigue on the operator of such instruments [14, 43]. As minimally invasive instruments are often complex, their sterilization is often time-consuming, costly, and carries the risk of cross-infections [52]. Therefore, disposable designs are of interest in recent developments to provide single-use minimally invasive devices [52, 53].

Most reviews agree on the increasing importance of robotic surgery, due to its advantages in reduced invasiveness, reduced control complexity, and surgeon's improved ergonomics [7, 54]. Yet, efforts are required to reduce the port size, introducing the term *needlescopic* as an expression of the intention of aiming for needle-sized endoscopic systems [13]. Further technological developments aim to improve navigation through the combination of multimodal imaging technologies with other pre- and intraoperative patient data [54].

In contrast to laparoscopy, no robotic system has yet managed to be introduced as a standard for flexible endoscopy. Challenges remain the complex control and the lack of sensory information through the instrument's or robot's flexible body. Recent research indicates, that this can be addressed if suitable sensor technologies are available. Loop detection in flexible endoscopes was already successfully tested in the OR [25, 48]. Pullens et al. could demonstrate the benefit of sensor-based lumen centralization [55, 56]. With their system, based on image processing, they could improve the intubation time and polyp detection rate of novice endoscopists [57, 58].

Motivated by these findings, this thesis researches the application of intraoperative spatial sensing for a flexible robotic system. In endoscopic applications, such sensor information can improve navigation and support autonomy features to relieve the endoscopist and improve patient outcome.

3 Medical Automation with Continuum Robots

After reviewing the standard of care regarding minimally invasive and endoscopic interventions, this chapter examines the technical state of the art, which this thesis builds upon and to which it compares. In the first section (Section 3.1), the state of the art of continuum robotic systems is provided. Then, in Section 3.2, an overview of methods for providing exteroception and applying it for CR control, is given. As this work's aim is to provide CR exteroception based on a capacitive method, fundamentals and the state of the art of capacitive sensing, in general, are presented in Section 3.3.

3.1 Continuum Robots

In chapter 4 the design of the robot developed in this work is introduced. To contextualize the methods, applied to its design, the following sections provide an overview of CR classification and technologies for CR actuation (Section 3.1.1), recent systems in the clinic (Section 3.1.2), in research (Section 3.1.3) and introduce methods for control (Section 3.1.4) of CRs.

3.1.1 Overview and Technologies

Conventional robots consist of discrete joints, connected by serial or parallel configurations of rigid links, to form an actuated structure, with multiple DOFs. Typical commercially available robot arms for industrial applications consist of such a serial set with up to 7 DOFs. In contrast, the term *continuum robot* describes robotic setups, which base their ability for motion on the elastic deformation of their solid body structure rather than distinct joints [59]. As such a deformation occurs distributed over the complete solid body, a continuous bending is present, instead of identifiable discrete joints. Such an actuated continuum structure can be regarded as a serial manipulator with the number of links and joints going towards infinity [3]. As an intermediate form, the terms *serpentine* or *snake-like robots*, denominate robotic systems with similar characteristics of long, slender, and highly actuated bodies, but still countable, discrete joints. While they still exhibit serial, discrete (and often passive) joints, their number of joints is often large and the length of links is kept short. Such an assembly creates a vertebrae-like structure that can be actuated similarly to continuum robots [60]. This allows to approximate the continuous bending of a CR and to use such systems in similar applications. As a visual aid, Figure 3.1 provides a graphical differentiation of the three presented classes.

Another class of robots, that is often mentioned regarding continuum robotics is given by *soft* or *compliant* robotic systems [61]. While the classes continuum robots and compliant robots show a large overlap of systems presented in research, it should be pointed out that they address

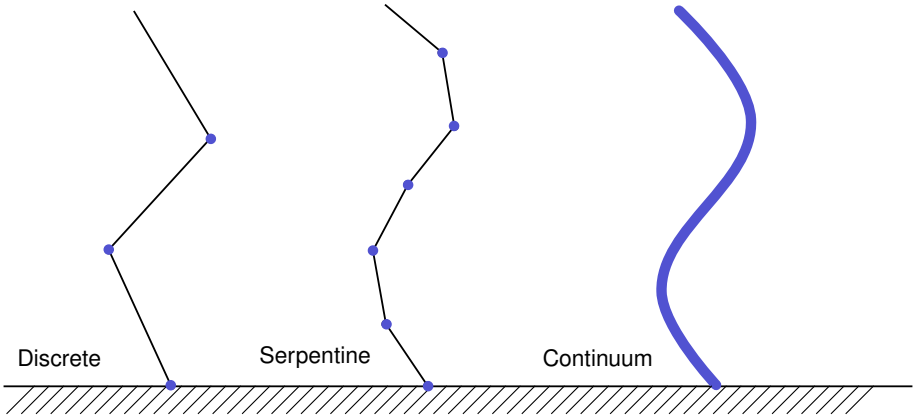

Figure 3.1 – Distinction of a discrete joint, serpentine, and continuum robot. Drawing based on content from [3, 59]

different properties of a robotic system. Compliant robotics focuses on the mechanical property (i.e., compliance) of the robots' links but also compliant joints. Continuum robotics focuses on the aspect of a method of actuation, based on continuously distributed joints, hereby the compliance of the whole actuated structure can be the crucial factor to allow for such actuation. Therefore, compliant robot is often the more generic term [61]. Soft robotics focuses on the implementation of compliant robot structures, often from materials such as silicone or rubber, and the harnessing of such softness for application benefits. This does not refer to a method of actuation, but often, continuum robotic methods need to be applied for the control of soft robots.

There are various characteristics by which CRs can be distinguished and classified, as shortly defined by the following list and detailed below.

- **Origin of actuation:** CRs can be separated in being *intrinsically* or *extrinsically* actuated. This refers to the origin of the robot's motion in relation to its structure. Actuators can be located inside of the continuum structure (intrinsically actuated) or outside of it and forces for motion are transmitted through the robot body (extrinsically actuated). Often this relates to the location of where the last conversion of energy to motion happens.
- **Actuation technology:** While intrinsic or extrinsic actuation provides a bipartite characterization of actuation. It can be further differed by the technology of actuation. As shown below, various methods can be applied to gain control over a continuum structure [62].
- **Field of application:** While most general purpose robots are discrete manipulators and serial robot arms, CRs often focus on specialized applications, where their properties are of special benefit. Therefore, many CRs are designed with a special application in mind and can be distinguished by such. Typical applications which motivate the usage of CRs are medical interventions [63, 64], inspections of complex machines (e.g. air turbines, or nuclear power plants) [65], harvest [66], space [67] or underwater robotics [68].

Various methods for the actuation of continuum robots have been developed and are currently being researched. The following listing provides an overview of technologies available for the actuation of continuum and serpentine robots and references some examples and reviews. Figure 3.2 illustrates the listed actuation principles graphically. This list serves as a reference for comparison of the methods presented later and will only shortly address tendon-driven systems. As such are the focus of this work, they are introduced in further detail below and in section 3.1.3.

- **Tendon-Driven (extrinsic):** An elastic backbone is deflected by a pulling force on tendons attached to the robot's distal end. The backbone's restoring force restores the neutral pose when the tendon is relaxed. More details on this actuation principle are given below and in Section 3.1.3.
- **Multi-Backbone (extrinsic):** Multi-Backbone setups rely on deformable parallel central rods, which can transmit not only tension but also compression in the axial direction. When these rods are moved in relation to each other, an end-spacer connecting them experiences a bending moment. This allows to steer the robot's tip [69, 70].
- **Concentric Tube (extrinsic):** In this setup, a set of hollow tubes are placed inside of each other. Typically these tubes are from a highly elastic material, such as Nickle Titanium Alloy (NiTi). The outer tubes are manufactured with a higher stiffness than the inner ones, e.g. by exhibiting a thicker wall. By imprinting the tubes with curved shapes, the outer tubes force their shape on the inner ones, while inserted. When extended from the outer tube, an inner tube takes its native shape. By nesting multiple such tubes in one another and actuating them extrinsically, multiple DOFs can be implemented [71, 72].
- **Steerable Needle (extrinsic):** This actuation is used for robots, traversing tissue. A beveled tip of a needle with an elastic body creates a deflection moment and brings the needle on a curved path. By rotating the needle axially, the direction of deflection can be steered [73].
- **Magnetic Actuation (extrinsic):** This actuation relies on stimuli from an external magnetic field. A magnet integrated into a robot structure experiences forces or moments from the external fields and gradients. Through a compliant robot structure, the respective part of a robot can be deflected and moved. The external field can be induced by robotically actuated permanent magnets [74] or arrangements of magnetic coils [75]. Magnetic actuation allows for actuation continuum robots but also tethered and untethered capsule robots (see below) [76].
- **Fluidic (intrinsic):** Another method to drive a CR is by incorporating chambers in an elastic structure, which expand when pressurized by a fluid (e.g., air, gas, or liquids). When being pressurized, these chambers extend and result in bending or elongation of the continuum structure. As a result of the actuation principle, such robots are often made from highly elastic materials such as silicone, they are a typical implementation of a soft robotics system [77–79].
- **McKibben (intrinsic):** A special variety of pneumatic actuators are McKibben actuators. These are tube-like chambers which can be pressurized with an additional braided filament wrapped around the camber. This filament influences the chamber's direction of motion when pressurized. They can be parameterized to result in either shortening or elongation when pressurized. This concept is not only used for continuum robots [80] but also for actuation of biomimetic robots, as they allow for mimicking of a muscle and tendon actuation of a skeleton, as in animal or human physiology [81, 82].
- **Growing Vine (intrinsic):** Another variant of pneumatic actuation is a robot's implementation as an extendable tube. This technology is based on a large inflatable tube with a thin wall that is folded inside out when pressurized. This way the robot's tip extends forward. During this process, the structure can adapt to the structure of the environment. It can be steered by incorporating sections of varying stiffness or additional pressurized pouches [83, 84].

- **Hydro Jet (intrinsic):** Here, actuation of a robot's tip is achieved by repulsion of a liquid media (e.g. water) from nozzles at the robot's tip. By controlling the flow from the nozzles, the direction and speed of robot deflection can be controlled. This is a specialized method for actuation, only suitable for a few applications. However, as medical interventions often rely on irrigation, such an actuation technology can be beneficial in such cases [85, 86].
- **Solid State Actuators (intrinsic):** Various materials induce a mechanical deformation when exposed to external stimuli, such as heat or an applied voltage. Such effects simplify actuator miniaturization and are therefore well suited for control of a continuum robotic structure. Common materials used in such applications are Shape-Memory Alloys (SMAs), such as NiTi which can be tuned to obtain a heat-based shape memory effect [87–89]. Alternative options are Shape-Memory Polymers (SMPs) [90] and Electroactive Polymers (EAPs) [91] which can induce motion when heat or voltage is applied. Also light based induction of motion has been researched [92]. Furthermore, the well-researched and commercially applied piezoelectric effect can be used for micro- and macroscopic actuation [93]. Depending on the design of such a solid-state actuator, it can be applied to form a discrete joint actuation or continuum actuator.
- **Micromotor (intrinsic):** Similar to conventional serial manipulators, multiple serial motorized joints can be used to actuate a long, thin structure. As per the definition above, this falls into the category of a serpentine robot. In such intrinsically actuated robots, the challenge of miniaturization of the motors comes into account to be able to form a slender robot structure [3, 94].
- **Capsule (both possible):** Capsule robots can be regarded as a separate class of robots instead of a subclass of continuum robots. Nevertheless, they are listed here, on the one hand, due to their relevance especially for gastroscopic applications, and on the other hand due to mixed form robotic systems with capsule and continuum robotic aspects. In a gastroscopic context, capsule robots are robotic systems, small enough to fit into natural orifices of the gastric tract, where they are either passively transported by the peristaltic motion of the bowels or exhibit various degrees of locomotion, either by being self-propelled or through externally applied forces such as magnetic fields. Capsule robots can also be tethered for power data interfaces, which requires retraction after an intervention [42].
- **Variable Stiffness (intrinsic):** This is another actuation technology that cannot provide a standalone mean of actuation. As the name suggests, it summarizes methods, which allow to control the stiffness of parts of the robotic structure. In combination with one of the presented actuation technologies, or by involving external forces from the robot's environment in robot control, this can provide additional DOFs for a robotic system. Various methods for controlling a structure's stiffness have been researched, such as interlocking structures, jamming particles, and application of solid-state actuators [95–97].

Extending the technologies presented here, various works present mixed technology systems aiming at combining advantages from multiple technologies.

Tendon Driven Continuum Robots are one of the most common forms of CRs. It consists of an elastic backbone, which is divided into sections by spacer disks, attached to it. Tendons for actuation are guided along its body, through holes in the spacer discs. A single segment of such a robot is terminated by an end-spacer, to which the tendons are attached. By applying

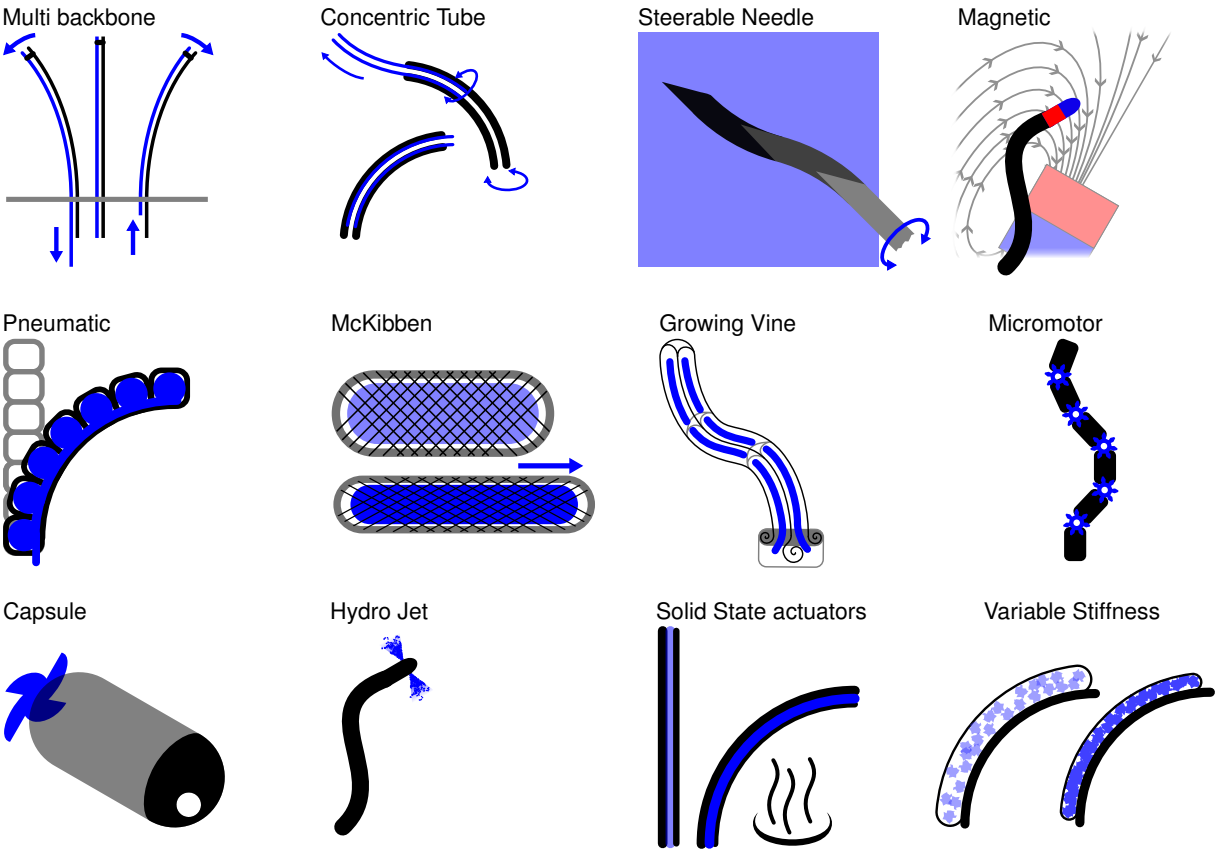

Figure 3.2 – Overview of actuation technologies for continuum robotic systems.

tension on one of the tendons, a bending moment is exerted on the backbone and it bends towards the tensioned tendon. The elasticity of the backbone creates a restoring moment and the robot structure takes a position at the equilibrium of both moments. Typically, a single tendon allows for bending in a single direction, from the neutral, upright position. Thus, bending in an arbitrary direction requires at least three tendons, distributed around the backbone. Typical implementations often work with two pairs of opposing tendons, as this allows for independent actuation of a full DOF by one pair of tendons. By serially stacking multiple segments, this concept can be extended to more DOFs. Advanced implementations are researched to increase the number of DOFs in a single segment: Extendable backbones can be used to introduce translational DOFs [98–100]. Helical tendon routing allows for an axial twist of a continuum robotic segment [101, 102]. Further details on the setup and implementation of such tendon-driven systems will be given in Section 3.1.3. An overview is provided in Figure 3.3.

Various CR implementations replace the elastic backbone of a tendon-driven continuum robot with a series of rigid elements, connected by passive joints or hinges. This way a serpentine robot, rather than a CR, is formed but with very similar actuation and behavior.

In the following, continuum robotic setups for application in medicine are introduced. The mechanical concepts and their implementation are presented and evaluated to provide reasoning for the design of the system of this work, presented in Chapter 4.

3.1.2 Continuum Robots in the Clinic

The so far presented surgical robots, often apply conventional rigid link manipulators. These provide high accuracy and reliability for robotic systems in medical interventions and can be

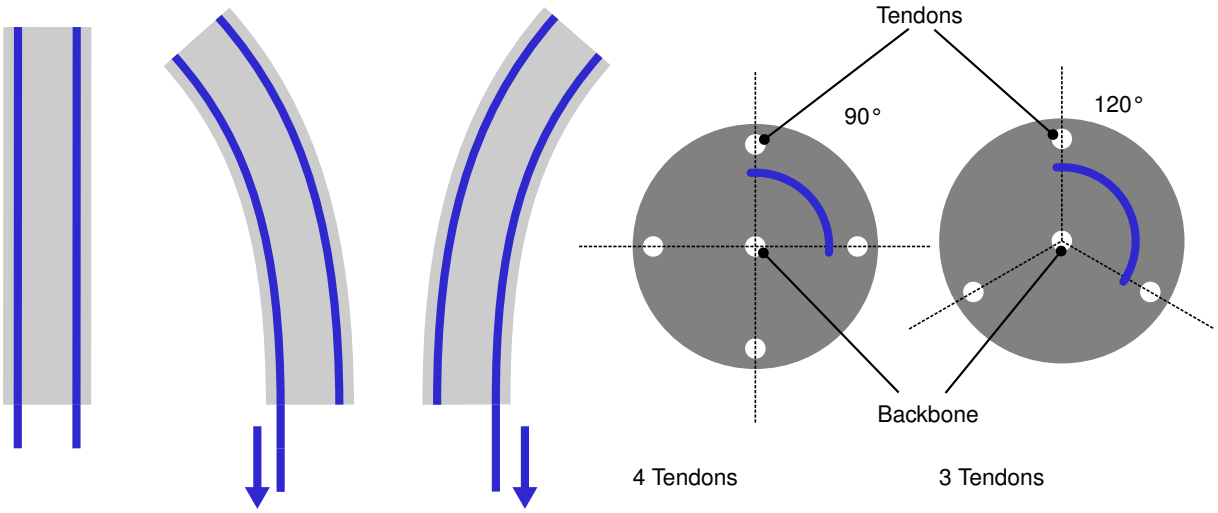

Figure 3.3 – Working principle of a tendon driven CR. Typical spacer configurations for four and three tendons are displayed on the right side.

efficiently developed and controlled. However, due to their bulky setup, they can hardly implement DOFs inside of the body. This means motion is restricted to the DOFs which can be transferred through the minimally invasive access port used for surgery. Rigid rod-like instruments are inserted and their motion is restricted to pivotal motion, insertion, or withdrawal. This restriction is referred to as RCM constraint and a typical factor, limiting the dexterity of surgical robots. Means to overcome this limitation are implementations of proximal "wrists", as they are present in the da Vinci system. However, this still only provides a very limited or local increase in dexterity and manipulability. Applying continuum robotics for surgery aims to facilitate access to the situs, even on non-linear trajectories. Furthermore, it aims to improve dexterity and manipulability by increasing the number of DOF available inside of the patient. This could already be implemented commercially, in the systems presented in the following. Section 2.1 shortly introduced FDA or CE approved robotic systems with rigid instruments. Even if not so widely established in medical practice, some robotic systems with continuum robotic characteristics have been developed and approved for application in the OR as well.

Conventional surgical robotic systems rely on a separate port for the access of each instrument and camera used. *Single port* systems follow the approach of introducing all instruments through one rigid shaft inserted through a single port. As this constrains all instruments to the same RCM, continuum robotic approaches are applied to the distal parts of the instrument to gain additional and independent DOFs. Such systems are often applied for general surgery, gynecology, and urology [1]. Single port systems, which have been commercialized are summarized in the following list:

- **Da Vinci SP**, Intuitive Surgical (US). The system comprises three instruments and a flexible endoscope. It gained FDA Approval in 2018 [1].
- **SPORT surgical system**, Titan Medical (CA). The system introduces two instruments and two cameras through a port of 25 cm diameter [25, 103].
- **Anovo**, Momentis Surgical (Israel). Its field of application is transvaginal surgery. It contains two flexible robotic instruments, each with 2-DOF bending and rotation [1].
- **SHURUI SP**, Surgerii Technology Co, (China). This Single-port multi-tool system is applied for ovarian cystectomy. It is actuated by a multi-backbone approach [104].

- **SurgiBot**, TransEnterix (US). It is based on an earlier development *Spider*, it incorporates two continuum robotic instruments, and a rigid straight one, as well as a 3D camera. However, it could not gain FDA clearance [25].

To eliminate the restrictions of RCM-constraints, other systems are implemented with a fully flexible body. While this enables navigation in more complex structures such as the lung or the digestive tract, such technology often limits the number of instruments that can be implemented. Presented commercial systems of such kind are:

- **Da Vinci Ion**, Intuitive Surgical (US). A Robotic Bronchoscope of 3.5 mm outer diameter. It includes a camera and a needle for biopsies. Navigation is supported by a 3D mapping system based on robot shape sensing and preoperative data [1, 103].

- **Monarch**, Auris Health (US). A Robotic Bronchoscope, teleoperated by a gamepad-like controller. The system is based on a variation of the concentric tube and tendon-driven robot, where an inner tube and an outer sheath are both controlled by tendons [105]. It includes a camera for the detection of nodules in the lung [1, 106].

- **NeoGuide Endoscopy System**, NeoGuide Endoscopy (US). Now acquired by Intuitive Surgical. This system is a highly actuated endoscope. It obtained FDA-approval in 2006. It comprises a body with 16 actuated segments [25, 30]. A successful clinical trial was conducted in 2007 [107]. It features a kinematic model for shape reconstruction and loop detection [25].

- **Flex robotic system**, Medrobotics Corporation (US). It features an endoscopic robotic system for head and neck surgery. Two forceps channels are attached along the endoscope's body. The system exhibits a length of 25 cm [31].

- **Invendoscopy E200 system**, Invendo Medical (Germany). A disposable robotic endoscope, steered via a handheld joystick controller. It gained FDA clearance in 2016. The system provides 35 mm bending radius, 170 cm length and a 3.1 mm working channel [25, 29].

- **Aer-o-Scope**, GI-View (Israel). Another single-use endoscope system. It gained CE and FDA approval in 2016. It supports examination in deeper regions of the colon by featuring a self-propelling tip, comprising inflatable balloons. These serve on the one hand for flattening folds in the colon, and on the other hand for closing a section of the colon, which is then pressurized to propel the endoscope's tip forward [43, 49, 50].

Instead of designing a fully robotic system from scratch, some manufacturers develop systems to automate conventional flexible endoscopes. This brings the benefit of being able to rely on established procedures regarding sterilization and usage while still providing the benefits of facilitated control for the surgeon. Examples of such systems are:

- **Avicenna Roboflex**, Elmed (Turkey). The system adapts to conventional endoscopes to allow for robotic control, from a surgeon's console. The system was CE approved in 2013 [1, 29].

- **EndoDrive**, ECE Medical Products (Germany). An adapter for conventional endoscopes, providing motorized advancement and axial rotation. Tip deflection is conducted manually, using the endoscope's conventional controls [29].

3.1.3 Medical Continuum Robots in Research

Section 3.1.2 presented robotic systems that are already approved or in the process of gaining approval for the application in surgery. The following section presents systems which also focus on an application in surgery but are part of ongoing technical research. The applied methods for actuation, sensing, and control are presented as fundamentals of the methods presented in this thesis. Mainly tendon-driven systems are regarded, as such actuation, is the most commonly applied and close to the actuation of manual flexible endoscopes. Furthermore, this work's robotic system is based on tendon actuation. Thus, the review of these systems allows to compare the method presented to its state of the art.

Generally, a tendon-driven CR requires at least three tendons per segment to enable full bending in all directions. However, many CR systems employ actuation with four tendons. This allows to regard bending along one axis (i.e., x- or y-axis) as independently actuated by one pair of tendons. This actuation concept is shown in Figure 3.3. In such a setup, bending from neutral (i.e., upright position) to the positive direction is taken over by one tendon, and bending in the negative direction is conducted by the other tendon. When one tendon is shortened to introduce bending, the opposing one needs to be lengthened. Such an *antagonistic* actuation allows to independently control the tendon displacements for the x and y components of a desired CR bending direction. Typically, a tendon is displaced by being wound around a drum. A motor rotates this drum, which shortens or lengthens the tendon, depending on the direction of rotation. Intuitively, this would require four motors for the actuation of a CR segment (i.e., four tendons). This can result in a high number of motors required for the actuation of a continuum robotic system. E.g. a system with three segments requires a large set of actuators with 12 motors as presented in [108]. Due to the fact, that the tendons of an antagonistic pair move contrary to each other, a common motor can be used to actuate both tendons. In such a setup, both tendons are coiled around the drum in opposite directions. This way, when one tendon shortens the other lengthens. Amanov et al. implement this concept in their proposed CR, with motivation for application in medicine [99]. Yeshmukhametov et al. utilize this concept to actuate a CR for the harvest of fruit [66, 109].

Antagonistic approaches face the challenge of slack, as two tendons are actuated together. As a visual aid, this is illustrated in Figure 3.4. For a given robot deflection, the displacement l_{short} of the shortened tendon is larger, than the displacement l_{long} required by the opposing tendon:

$$l_{\text{short}} \geq l_{\text{long}} \tag{3.1}$$

As both antagonistic tendons are actuated together, the displacement of the tendons introduced by tendon drum rotation is equal for both tendons (i.e., l_{short}). Without countermeasures, this results in a reduction of tension on the lengthened tendon, which can result in tendons entangling or losing their guidance on pulleys. To overcome this issue tensioning mechanism can be incorporated into a CR (see [110]) or the pulley radius can be varied, as presented in [111].

To increase a CR's dexterity, research investigates how more DOFs can be introduced into a continuum robot structure. Therefore, many works introduce two or three independently controlled, serial segments [66, 109, 110, 112, 113]. Other works investigate how a single segment can incorporate more than just two bending DOFs by introducing extendable segments. This way, the two bending DOFs of a single segment can be extended by a translational DOF. Gaining a translational DOF in a continuum robot is of special benefit for medical interventions, as a robot or instrument needs to be inserted into the body. To achieve this, CRs can be installed on

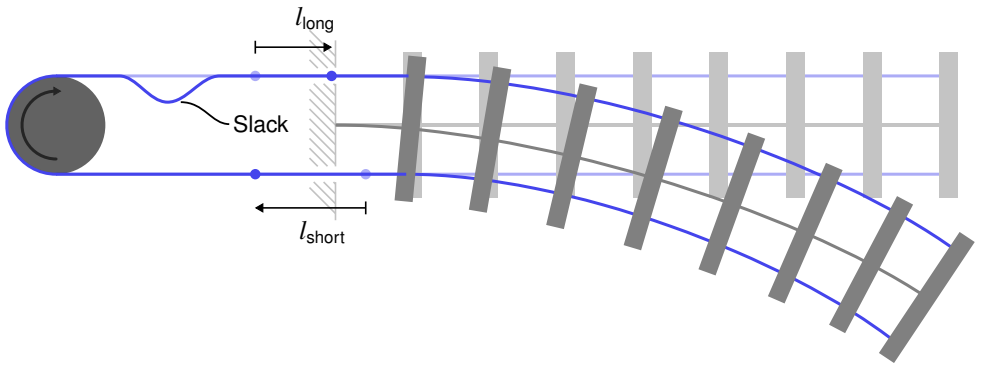

Figure 3.4 – Visualization of slack in antagonistic actuation. As the upper tendon requires less displacement than the lower one, the relaxed (i.e. upper) tendon experiences slack.

a linear axis or a robotic arm [66, 113–115]. Alternatively CRs are researched to be extensible by winding their body on a spool [116], by extending their backbone with magnetic spacers [98, 117] or by online assembly [100].

Another method to increase the number of DOFs in a CR's segment is to incorporate the ability to twist the body, via a helical tendon routing. Typically, a continuum robot cannot achieve a rotation of its tip around its backbone's axis. However, by routing tendons helically around the backbone, a moment can be induced. This also allows for non-planar bending of a single segment [101, 102, 118]

The presented methods for CR actuation aim to facilitate various interventions. A CR system presented by Hong et al. is designed for a minimally invasive intervention in the Maxillary Sinus (hollow structure in the skull, inferior to the eye) [113, 114]. Their system features a grasper and camera at its tip and exhibits a two-segment CR with only 4 mm diameter. This is required to allow for the complex access trajectory through the nose. The system also applies variable stiffness based on an interlocking structure to improve the manipulation of tissue.

Kume et al. developed an endoscopic system for application in gastrointestinal endoscopy. They integrated therapeutic tools, such as forceps, knife, and biopsy needles to conduct endoscopic submucosal dissection in an ex vivo porcine model. Their system is based on an externally actuated conventional flexible endoscope, with the additional tools attached to its proximal tip [119, 120]. Liang et al. could conduct a similar study in an in vivo experiment on a pig with a system that fully integrated the therapeutic tools in the instrument's 10 mm outer diameter [121]. A system by Troncoso et al. provides three distal segments actuated by four motors each, which allows it to be applied for throat surgery by attaching tweezers, and diathermy cutters next to a camera [108].

3.1.4 Modeling and Control of Continuum Robots

Modeling and controlling a continuum robot has been reported as one of the major challenges to be overcome for extensive applicability of CRs [122]. As justification and fundamentals for the control method, presented in this thesis, an overview of control methods for CRs is provided.

Figure 3.5 visualizes the modeling process of a CR. Modeling a CR is the task of mapping a robot's actuator space $\mathbb{Q}$ to its task space $\mathbb{T}$. A robot's actuator state $\boldsymbol{q} \in \mathbb{Q}$ such as the robot's motor positions, results in a task space representation $\boldsymbol{p} \in \mathbb{T}$ (e.g., the robot's Tool Center Point (TCP) pose $\mathbb{T} \subset \mathrm{SE}(3)$). To allow for such a mapping, an intermediate representation

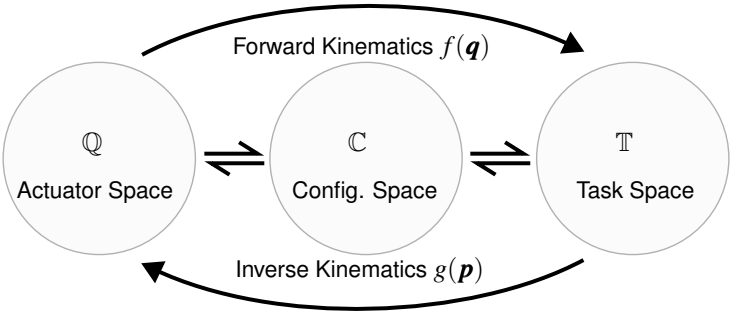

Figure 3.5 – Modeling process for continuum robot control. Graphic adapted from [65, 122, 124–126]

of the robot configuration can be required, the respective space is the robot's configuration space $\mathbb{C}$. The robot configuration $\boldsymbol{c} \in \mathbb{C}$ contains parameters describing the state of the robot model. Depending on the model, the number of parameters (dimensionality of $\mathbb{C}$) can differ significantly. A robot model $f(\boldsymbol{q})$ maps from actuator space to task space: $f : \mathbb{Q} \mapsto \mathbb{T}$. For the control of a continuum robot, the inverse mapping $g : \mathbb{T} \mapsto \mathbb{Q}$ is required, to determine control commands for a given task space goal [63, 123].

As a method to accurately represent the physical behavior of a continuum robot, Cosserat-rod theory can be applied [127]. Hereby, the robot backbone is modeled as a 1D thin and long rod, subject to bending, shear, and twist moments. As such a model takes forces into account, means to incorporate tendon-force sensing into a CR are of interest in continuum robotic research [99, 128, 129]. Alternatively, the forces can be modeled based on the actuator position, which, however, results in lower precision. The Cosserat-rod model sets up the differential equations for the forces and moments in the system. To simplify the differential equations, typical implementations assume moments only to affect the robot at the end spacer locations, where tendons are terminated. As solving the set-up differential equations can be computation-heavy, such models are often less suitable for fast control of a continuum robot [122].

A solution to overcome this limitation is a constant curvature assumption. In a first approximation, the backbone shape can be modeled as exhibiting constant curvature over its full length [124]. This allows a CR's segment to be fully described by a bending direction ϕ and a curvature κ. Such a model can be set up as a closed-form forward model and is suitable for fast implementations of inverse kinematics. The gain in computation speed comes at the cost of losses in accuracy, as the assumed constant curvature only provides a limited approximation. Therefore, variants have been developed that try to counteract these limitations [122]. An example is the piece-wise constant curvature model, which offers additional accuracy by dividing a segment into several pieces that exhibit constant curvatures, that can differ from each other [62]. Further modeling approaches can rely on another shape-based representation (e.g. a spline), approximate the CR by multiple rigid link bodies, or by lumping parameters along the robot shape [122].

Inaccuracies in the robot model or external influences can render a purely model-based forward control imprecise and unreliable. Therefore, a lot of research engages in equipping CRs with proprioceptive sensors providing feedback on the sensor's task space state. Such sensors allow to model the current robot state not just from actuator space but include sensory information, possibly taking external influences into account. Based on such sensing, the robot configuration can be controlled in a proprioception-based feedback loop. Typical sensors that can be applied for continuum robotic proprioception are Fiber-Bragg-Gratings (FBGs) implemented in thin optical fibers, which can easily be embedded in the robot body. They allow for the determination of the amount of stress at the gratings' locations and derive the robot shape

[130, 131]. Further methods utilize external sensing and imaging modalities, which are often already present in a surgical context. This can be intraoperative imaging (e.g. CT, MRI, US) and electromagnetic tracking. In image-based methods, the challenge lies in 3D robot shape reconstruction from the respective images [130]. In electromagnetic tracking, uniform precision and sensing setup configuration can be a challenge [130]. Other modalities include inductive, Hall effect, and stretch sensors [62].

Control of a continuum robot can also be achieved by data-driven models. Various approaches try to sample, actuator, and task space training data, to train neural networks-based approaches to approximate the inverse kinematics [125, 126]. As training data, real-world recordings or simulation results from precise, but computationally costly simulations can be utilized. In such control approaches, challenges lay in data acquisition, adaption to structural changes, and efficient model inference for real-time control [123].

3.2 Exteroceptive Sensing in Minimally Invasive Surgery

With a CR set up, and control implemented, various works look into the automation of surgical tasks or invasive diagnostic applications. To achieve this, sensory information on the situs is required, for motion control, especially, spatial information is needed. In the following, research is presented, that investigates methods for exteroceptive sensing, integrated into minimally invasive systems with a special focus on technologies that can be applied or have been demonstrated in continuum robotic systems, to leverage motion control and automation.

3.2.1 Proximity and Distance

As therapeutic and diagnostic interventions deal with delicate tissue and organs, distance to such objects is crucial information for navigation inside a patient's body. Cheng et al. in [132] and Liu et al. in [133], both present continuum robotic systems, which are equipped with optical fiber distance sensors. Such sensors allow for lateral distance measurement at the robot's tip. The working principle of fiber distance sensors is visualized in Figure 3.6. Light is projected from the distal end of an optic fiber onto an opposing surface. Here, it is reflected and partially cast back into the fiber. The amplitude of the returning light correlates with the distance of the reflecting surface. Thus, an intensity measurement allows to estimate the sensor's distance from an object. In [132], three optical fiber sensors are integrated into a pneumatically actuated continuum robot and used to determine the robot's distance from the wall of a tubular environment (i.e., representing the colon). A control strategy is presented to keep the robot centered in such an environment. Liu et al. utilize the same sensing principle in a tendon-driven CR. Here, four fiber distance sensors are embedded in the sensor's tip and used for distance control to an object in motion (i.e., the beating heart). Optical fiber sensors can present obvious advantages as they exhibit a thin body (often with sub-millimeter thickness) and prove to be ideal for facile integration in a continuum robotic system. Their directivity and signal strength can be optimized by suitable cutting angles [134]. Yet, they are disadvantageous in their susceptibility to varying reflectance of the sensed object and - especially in a medical context - debris in the path of light.

Distance information can also be derived from a camera integrated into a CR system [135]. As a vision system is the fundamental component of any endoscopic instrument and serves for

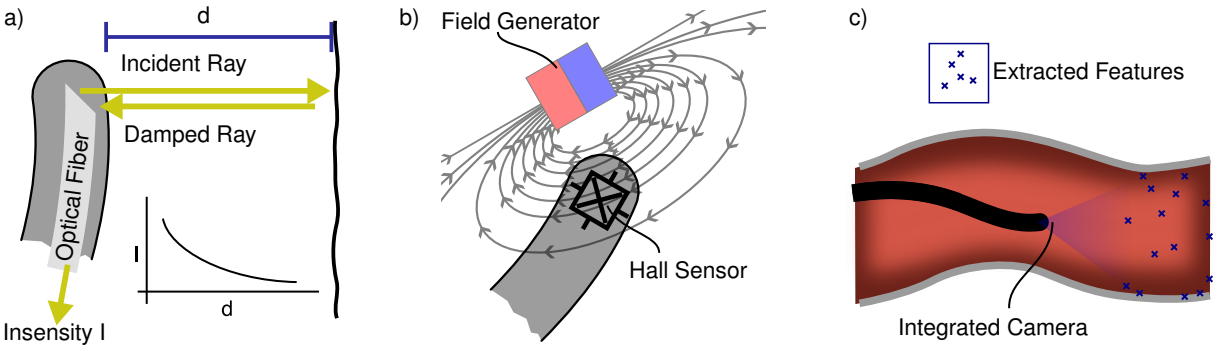

Figure 3.6 – Overview of exteroceptive sensing modalities in CRs and their working principle. a) Optical distance sensing based on the intensity of a reflected ray of light. b) Localization in a magnetic field using hall sensors. c) Localization based on an integrated camera.

a surgeon's orientation and navigation, it is obvious to utilize this information in automated systems. To determine the direction for advancement and for centering in the colon, recent research investigates depth estimation from monocular images as they mostly are available from endoscopic systems [56, 57, 136, 137]. Visual localization can be based on Simultaneous Localization and Mapping (SLAM) [138]. Here, image features in subsequent images are detected and correlated. From the disparity, the environment is reconstructed and the imaging origin is localized in this environment. Applied on an endoscopic CR this can serve to map the situs and localize the robot's tip with the integrated camera, as demonstrated in [139–143]. This also brings the advantage, that a map of the situs can be created which can, for example, serve for documentation of detected polyps [144]. However, SLAM often relies on a static environment, where changes outside the field of view, can render a created map unreliable.

In microsurgery, such as ophthalmic procedures, the instruments are too small to integrate cameras. Thus, an external image e.g. from a microscope can be utilized to estimate the instrument's distance to the environment. In [145] the instrument and its cast shadow from microscope illumination were tracked to estimate the instrument's distance to the retina.

Besides visual imaging methods. Also US [146] or OCT images [147] can be integrated in CR systems. As such imaging modalities mainly provide information on the inner structure of tissue, they are less suitable for measurements of distances through air or gas. They are rather used to determine the distances to an organ or a boundary surface through tissue. In special cases, magnetic sensors can be used to sense the distance of metallic clips in tumors used during surgery or can be applied for the search of shrapnel [148, 149].

In an industrial context, Time-of-Flight (TOF) distance sensing is a popular candidate for distance measurements. While Abah et al. present a continuum robot with TOF based distance sensing, their system is not intended for medical application. The outer diameter of 15.8 cm demonstrates the challenge of miniaturization which impedes the integration of TOF into CRs [150]. Nevertheless, initial approaches to integrate TOF into a rigid endoscope, using light guides, could indicate that such a technology might be available in the future [151].

3.2.2 Contact and Force

Contact and force sensing is of special interest in MIS, as conventional surgical procedures often rely on a surgeon's ability to touch and feel tissue. Through MIS this information is lost (see

Section 2.1.1). To restore the availability of such information through minimally invasive instruments, sensors are integrated into medical instruments and can provide this information back to the surgeon. For rigid minimally invasive instruments, research efforts investigate the integration of force sensing distally, proximally, and in the shaft of a minimally invasive instrument [152]. Proximal integration of sensors often benefits from less spatial constraints compared to distal sensor integration. However, proximal sensing often involves complex models to estimate distal forces and can provide less accuracy due to additional disturbances, transduced through the minimally invasive instrument's structure [153]. To measure distal forces on a minimally invasive instrument, conventional force-torque sensors (FTSs), based on resistance strain gauges, have been miniaturized to be applicable to the distal end of a laparoscopic gripper [153–155]. In such FTSs, strain gauge sensors measure the displacement of an elastic structure. From the deformation and calibration, the forces and moments applied to this structure can be derived. Noh et al. transfer such a design from rigid instruments and robots onto a CR [156]. Instead of strain gauge sensors, optical displacement sensors can be applied. For miniaturization, such sensing can be implemented with optical fibers [157, 158] or transducers can be integrated directly into the CR structure [156]. Optical fibers with FBGs allow measurement of a displacement on multiple locations along the fiber. This principle can also be utilized for the detection of forces and moments applied to surgical instruments [159] and to CRs [160, 161]. In the latter, FBGs are not only used for proprioceptive shape sensing (see Section 3.1.4) but can also serve for exteroception of forces.

To characterize not only a binary signal of contact or a linear force, but to provide information on the structure of a surface, more complex sensors can be integrated into minimally invasive robots. Such as the *Haptic Vision Sensor* developed by Fagogenis et al. Such a sensor consists of an elastic contact surface, filmed from the backside by an integrated camera. A controlled lighting environment allows structural information to be derived from the reflection pattern. The sensor is integrated into a minimally invasive, concentric tube robot to navigate to the heart [162].

Even capacitive sensing can be applied for force sensing in minimally invasive instruments. This is reported in Section 3.3.3 with more details.

3.3 Capacitive Sensing

Electrical capacitance is the property of an electric circuit to store charge. To utilize this effect for various applications, capacitors are available as parts for circuit design. However, all conductive (e. g. charge-bearing) parts in an electric assembly can be assigned a residual capacitance. The extent of such a capacitance strongly depends on spatial relations and materials of a circuit. Thus, capacitive measurement allows the characterization of a circuit regarding such factors. In this thesis, this concept is utilized to derive proximity and contact information of a robotic setup and its environment. As fundamentals for such methods, the following sections present the general principle of sensing capacitance (Section 3.3.1), how it is applied in proximity sensing (Section 3.3.2), and contact sensing (Section 3.3.3) applications, with focus on robotics.

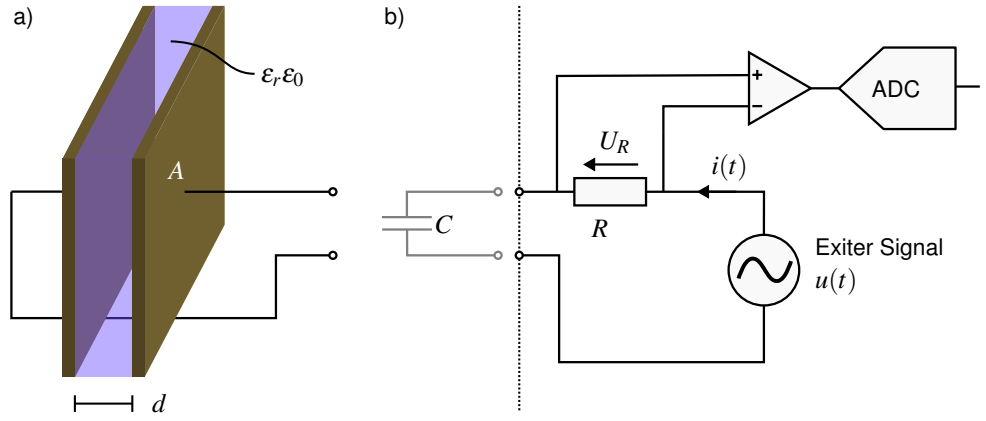

Figure 3.7 – a) Visualization of a parallel plate capacitor with electrode area A and a plate distance of d. b) Basic measurement circuit schematic. An alternating voltage $u(t)$ is applied to the capacitor setup C and the current $i(t)$ is sampled over a shunt resistor R.

3.3.1 Capacitive Sensing Principle

One of the most basic forms of a capacitor setup is the parallel plate capacitor, visualized in Figure 3.7a [163]. Two square, parallel plates from a conductive material (i.e., electrodes), are charged by a voltage U_0. Both electrodes are dimensioned equally, with an area A, and an intermediate spacing of d. When the distance is relatively small, compared to the capacitor plate's length, i.e., $d \ll \sqrt{A}$, the setup's capacitance C can be determined by

$$C = \varepsilon \frac{A}{d}. \tag{3.2}$$

In this equation, $\varepsilon = \varepsilon_0\varepsilon_r$ is the material-dependent factor of *permittivity*. For the setup described above, it is assumed, that the space between both capacitor plates is homogeneously filled with one material. The material's permittivity is a product of the natural constant *vacuum permittivity* $\varepsilon_0 = 1.112\,650\,055\,45 \times 10^{-10}\,\mathrm{F\,m^{-1}}$ [164] and the material factor, the *relative permittivity* ε_r. Table 3.1 provides some examples of the relative permittivity of some exemplary inorganic materials and tissues.

To measure the capacitance of a circuit, a sinusoidal voltage $u(t) = \hat{U}\sin(\omega t)$ of an angular frequency ω and amplitude $\hat{U}$ is applied. In an alternating current circuit, a capacitance C can be expressed as a complex impedance $Z = 0 - j\frac{1}{\omega C}$ (where j denotes the complex number) [163]. A current $i(t) = \hat{I}\cos(\omega t)$, with amplitude $\hat{I}$ is induced and the voltage can be expressed as $u(t) = Zi(t)$. From this, the relation of the voltage's and current's amplitudes can be used to determine the capacitance as in

$$\hat{U} = \hat{I} \cdot |Z| \Leftrightarrow C = \frac{\hat{I}}{\omega\hat{U}} \tag{3.3}$$

The principle from Equation 3.3 can be used in a simple schematic as presented in Figure 3.7b, to measure a setup's capacitance. An exciter signal is applied to the setup under test and the resulting current is measured as a voltage U_R over a shunt resistor R by an Analog Digital Converter (ADC). The sampled voltage U_R can be converted to the current through R, which, in combination with the known exciter signal, can be used to estimate the capacitance present.

Adding to the simplified schematic in Figure 3.7b, real-world measurement circuits comprise additional parts for the usage of multiple channels and switching of measurement modes

as well as analog filtering, amplification, and digital processing of the signal. Further additions aim at additional features, such as a selectable exciter frequency and shielding options for the electrodes. For the application of capacitive sensing for proximity and tactility, changes in capacitance in the range of 100 fF to 10 pF have to be measured [166]. In this range, parasitic capacitances from Surface-Mounted Device (SMD) parts on the measurement circuit, such as analog switches, introduce relevant errors. To overcome such errors, and provide capacitive sensing on eight channels, Alagi et al. present a sensing circuit that integrates reference capacitors and a measurement bridge in a capacitive measurement [166]. By comparing the reference signal and the capacitive input signal (both including identical analog switches), the introduced error from the parasitic capacitances of the measurement circuit can be suppressed to a large extent. The measurement circuit presented by Alagi et al. is used in the methods presented in Chapter 5 and Chapter 6.

3.3.2 Proximity and Distance

A capacitive measurement can be utilized to estimate distances. Such sensing methods make use of the capacity's dependency on the distance d (see Equation 3.2). When the capacitor's plates move away from each other, the capacitance increases. A typical proximity sensing setup comprises a sensing electrode, subject to excitation. It is modeled by one plate of the parallel capacitor (Figure 3.7a). The other plate is represented by an approaching object or surrounding environment. This kind of capacitive sensing modality is referred to as *self-capacitance* sensing [167]. Its principle is visualized in Figure 3.8. To allow for such a representation, the object to be detected needs to be conductive to represent the capacitor's plate and allow the sensing electrode's electrical field to couple to its surface. Nevertheless, such a scenario diverges strongly from the idealized parallel plate capacitor and Equation 3.2 is unsuitable for directly solving for the distance d. Still, such a measurement can be utilized, as the correlation of measured capacitance to distance persists. Realistic scenarios comprise complex geometry with many unknown parameters, especially in robotic use cases. Therefore, an analytical solution for a closed-form formula, which maps capacitance to distance can hardly be applied. Instead, calibration experiments on the applied setup allow to empirically quantify the relation between distance and capacitance. In the literature presented in the following, such an empirical mapping of the capacitance is often referred to as *proximity* instead of *distance* to account for the lack of a theoretical model of the underlying physics.

Capacitive proximity sensing is an attractive candidate for providing distance information, as it allows for simple setups. As transducers simple electrode setups can be utilized which only require conductive surfaces in almost arbitrary shapes. This allows for facile implementation of highly customized sensing setups, suitable for various use cases [169, 170]. Capacitive sensing is not only versatile regarding electrode geometry, but it also supports their implementation from various materials. As the only requirement for the electrode material is its conductivity,

Table 3.1 – Static Relative Permittivity of Exemplary Materials and Tissues. Data from [165]

Material	ε_r	Tissue	ε_r
Air	1.1	Blood	5260
Polyethylene	2.3	Bone	1.05×10^5
Silica	2.4	Tooth	1.05×10^5
Water	80.2	Fat Tissue	1.00×10^7
Hydrogen peroxide	128	Liver	3.01×10^7

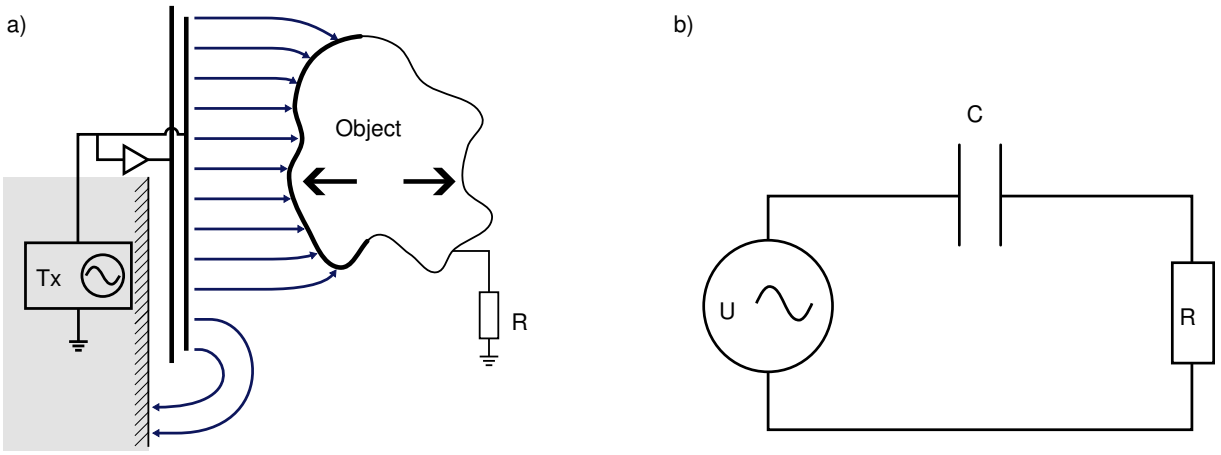

Figure 3.8 – Visualization of the concept of capacitive proximity sensing. a) An electric field spans between a sensing electrode and an object. b) The equivalent schematic representing this scenario. Adapted from [168, 169]

the manufacturing of soft or printed electrodes is also possible [8, 171]. Capacitive proximity sensing experiences limitations when it comes to sensor range, which is typically limited to the range of the size of its electrodes. To overcome such issues, capacitive sensing is often combined with long-range sensors (e.g., optical sensors) [169].

Robotic applications of capacitive proximity sensing can be found in industrial robotics, where capacitive sensing is applied for contact avoidance. Several works aim to cover robots with a hull or skin to prevent collisions with workers or objects [166, 172–174]. Another interest of research is to leverage proximity information for robot motion control in industrial [175–177] or Human Robot Interaction (HRI) scenarios [178]. Capacitive proximity sensing is also an attractive candidate for fine-grain control of grippers and prosthetic and robot hands [179]. Here, fingertips are sensorized to allow for the determination of object shapes and grasping poses.

3.3.3 Contact and Force

With capacitive sensing, tactile sensing can also be realized. This modality is based on a very similar sensing concept as capacitive sensing. One variety of such a setup incorporates both electrodes of the capacitor setup (see Figure 3.7a and integrates an insulating, elastically deformable medium in between both. This allows the outer electrode to be shifted towards the inner one when experiencing a normal force. This shift can be detected and quantified as a change in capacitance. Depending on the characteristic of the elastic medium, and the expected forces, the relation of force and distance can be assumed to be linear or requires a more complex regression and calibration. This way thin force transducers can be manufactured with a highly customizable geometry for integration in robotic systems. Another concept to realize tactile sensing is to rely on a capacitive setup's variation of the overlapping area A (as in Equation 3.2). When a parallel capacitor's plates are shifted laterally, in a first approximation, only the overlapping area accounts for the setup's capacitance. In combination with an elastic medium or structure connecting both, this can be used to create a sensing setup, receptive to shear forces. By combining multiple such elementary (shear or normal force) measuring units with suitable mechanical structures, up to full 6-DOF FTS can be realized, as shown below. Figure 3.9 visualizes different concepts for different tactile modalities based on capacitive sensing. In MIS tactile feedback is often restricted or lost through the usage of long and rigid instruments, pivot-

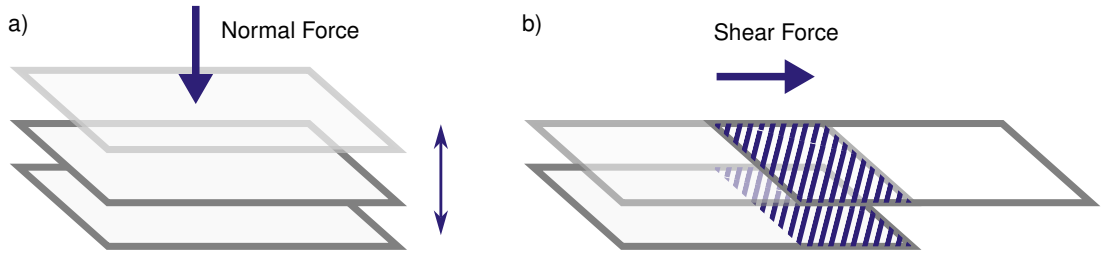

Figure 3.9 – Two fundamental principles for capacitive tactile sensing. a) On the one hand, a variation of the capacitor's distance d (in Equation 3.2) can be utilized. b) On the other hand, a variation of the overlapping surface (shaded area). The induced change in capacity allows for the conclusion of the normal or shear force applied. The combination of such elemental units allows for more complex sensors with multiple DOF.

constrained motion, or flexible endoscopes. Therefore, it is in the interest of research to provide in situ force sensing to minimally invasive instruments. While there are approaches to introduce such sensing on a proximal part of the instrument or inside its shaft, this comes with limitations due to a less direct measurement method. Distal integration, however, struggles with strict requirements regarding a feasible volume for integration [152, 180].

With capacitive sensing technology, minimally invasive graspers can be equipped with a distal sensor to determine gripping forces and moments [181–184]. The possibility to implement such sensors as thin layers enables force sensing in such space-restricted applications as MIS. Kim et al. further develop this sensor concept to a 3-axial force sensor [185] and also to a full 6-DOF FTS [186]. Such sensors can then be applied for minimally invasive palpation examination [187–189], e.g., for the detection of lung nodules [190]. For application in continuum robots, Lo presents a concept for a capacitive sensor that can be integrated into the tip of a continuum robot and provides force feedback for an ablation needle at the robot's TCP [191]. The sensor measures the needle's displacement with capacitive electrodes integrated in the robot's tip and derives forces applied to the needle.

Capacitive force sensing is also in the interest of robotic applications on grippers and humanoid hands. In this field of research, capacitive tactile sensing allows to acquire information on gripping forces and contact points, which is highly relevant information for grasping [167, 192], in-hand manipulation [193] and hand-over tasks [194]. Due to the low integration volume of the transducers, also dense arrays of such sensors can be designed [195].

The two presented capacitive sensing concepts for proximity and tactility are also well-suited to be integrated into a combined sensor. To achieve this, a multilayered structure as presented in [196] can be utilized. It allows for proximity and tactile sensing with often neglectable additional volume for integration compared to a single modality sensor.

4 Antagonistic Continuum Robot

Accessing the surgical situs in minimally invasive settings can be challenging. To address this issue, this chapter investigates the lack of accessibility in a minimally invasive setting. Therefore, a robot platform is to be developed which enables to bring spatial sensors to the situs. In this chapter, the system's actuation is addressed and the developed robot is presented and evaluated. The initial section will briefly repeat the motivation for such a minimally invasive CR. Section 4.2 will go into detail on the requirements for such a system. In the following section, the methods for the design of such a system are described. This design was substantially supported by the Master's theses of Thomas Scherr and Felix Buck. Based on their work, the robot design could be published in *at-Automatisierungstechnik* in 2023 [9]. Section 4.4 presents the robot's workspace and repeatability analysis, which is then discussed at the end of this chapter. For look-up and overview purposes, Table 4.1 provides a reference of all symbols used in this chapter, with constant values for the robot design denoted.

Table 4.1 – Overview of the symbols introduced in this chapter and the CR's design parameters

Symbol	Parameter	Symbol	Value	Parameter
$M_{X1}, M_{Y1}, M_{X2}, M_{Y2}$	Robot Servo Motors	l_0	260 mm	Backbone Length
$T_{(X+)1}, T_{(X-)1}, T_{(Y+)1}, T_{(Y-)1}$	Tendons Segment I	n_S	16	Number of Spacers
$T_{(X+)2}, T_{(X-)2}, T_{(Y+)2}, T_{(Y-)2}$	Tendons Segment II	n_{Seg}	2	Number of Segments
θ	Servo Angle (general) [rad]	d_S	9.9 mm	Spacer and Robot Diameter
d	Tendon Displacement	t_S	1.5 mm	Spacer Thickness
d'	Lengthened Tendon Displacement	r_{TD}	6.0 mm	Tendon Drum Radius
l_L	Lengthened Tendon Length	r_T	3.5 mm	Tendon - Backbone Distance
l_S	Shortened Tendon Length	d_{bb}	1.0 mm	Backbone Diameter
d_S	Slack	h_{sub}	58 mm	Substruction height
r	Backbone Bending Radius	a_{BP}	230 mm	Base plate side length
κ	Backbone Curvature			
ϕ	Backbone Angle			
F_T	Tendon Force			
F_{LC}	Load Cell Force			
$\boldsymbol{q} = [\theta_{X1}, \theta_{Y1}, \theta_{X2}, \theta_{Y2}]$	Current robot configuration			

4.1 Introduction

MIS constraints the motion for used instruments to a few ports chosen for access. From such a port, conventional instruments can only access the situs on linear trajectories, and their motion is restricted to pivoting, axial rotation, and insertion/extraction. Surgical CRs are investigated to create minimally invasive systems that provide additional, distal DOFs inside the body of a patient and improve the accessibility of the situs. This renders the manipulability in MIS closer to the situation in open surgery and provides the surgeon with more flexibility to operate. Examples for such CRs are presented in [98, 99, 102]. However, they often consist of large, bulky setups with various separate peripherals required for operation. Furthermore, to allow

for advanced research on CRs for MIS, an experimental setup should be equipped with force measurement on each tendon. Combining such characteristics in a continuum robotic setup has hardly been addressed by literature so far. Therefore, this chapter investigates the design of a CR that incorporates force sensing for each tendon, and provides all means for operation in a compact volume, by minimizing the number of motors required for actuation. The system is designed with an application in MIS, and later integration of proximity sensing in mind.

4.2 Requirements for a Minimally Invasive Continuum Robot

Chapter 2 and Chapter 3 point out how gastroendoscopic devices benefit from robotic features or even require them to integrate advanced diagnostic and therapeutic functionalities. For the overall goal of this thesis, a robot platform is required, which fits in a research setting, allows integration of capacitive sensing, and can demonstrate spatial sensor-based automation. To keep close to a possible application, it should mimic the properties of a typical endoscopic device. For the proof of concept in this work, colonoscopy is chosen as a motivator as here spatial restrictions allow for the least trade-offs for the sake of miniaturization. In the following, the requirements for the developed robot are listed:

Actuation Priniciple For the proposed application, the robot's actuation setup should be kept simple. Especially the robot's distal parts support the system's pursued use case in MIS, where they enable a potentially disposable design of the robot's invasive parts. To keep the system cost-efficient, the design must minimize the number of required actuators. While the system is not designed for in vivo use, it should still address practical challenges, like sealing the robot body from liquid and humidity.

Dimensions The robot should represent an actuated tip of a gastroendoscopic system. To minimize sedation and pain, an endoscope's diameter is kept as small as possible while still being able to integrate its functionalities and working channels. While for some of the robotic approaches in research, this results in diameters of up to 25 mm, most standard instruments' diameters remain below 10 mm. Therefore, the latter upper limit is also required for the system to be designed. The system's segment length should mimic the length of a typical endoscope's deflectable tip. As only an endoscope's proximal part should be modeled by the continuum robotic system, an upper limit of 15 mm is aimed for one segment's length.

Degrees of freedom Most flexible endoscopes provide a tip that is deflectable in only one or two directions, as more DOFs would overwhelm an endoscopist's manual steering capabilities. The new design should allow to research additional benefits through robotic control which is not affected by such limits. The robot's design should support at least two controllable segments, with two-DOF bending for each.

Proprioceptive Sensing The review of literature on robot control (see Section 3.1.4) points out benefits in accuracy of force-based kinematic models for CR control. Therefore, the design should not only allow to position-control the displacement of a tendon but also monitor each tendon's force, thus allowing for the application of force-based closed-loop control models.

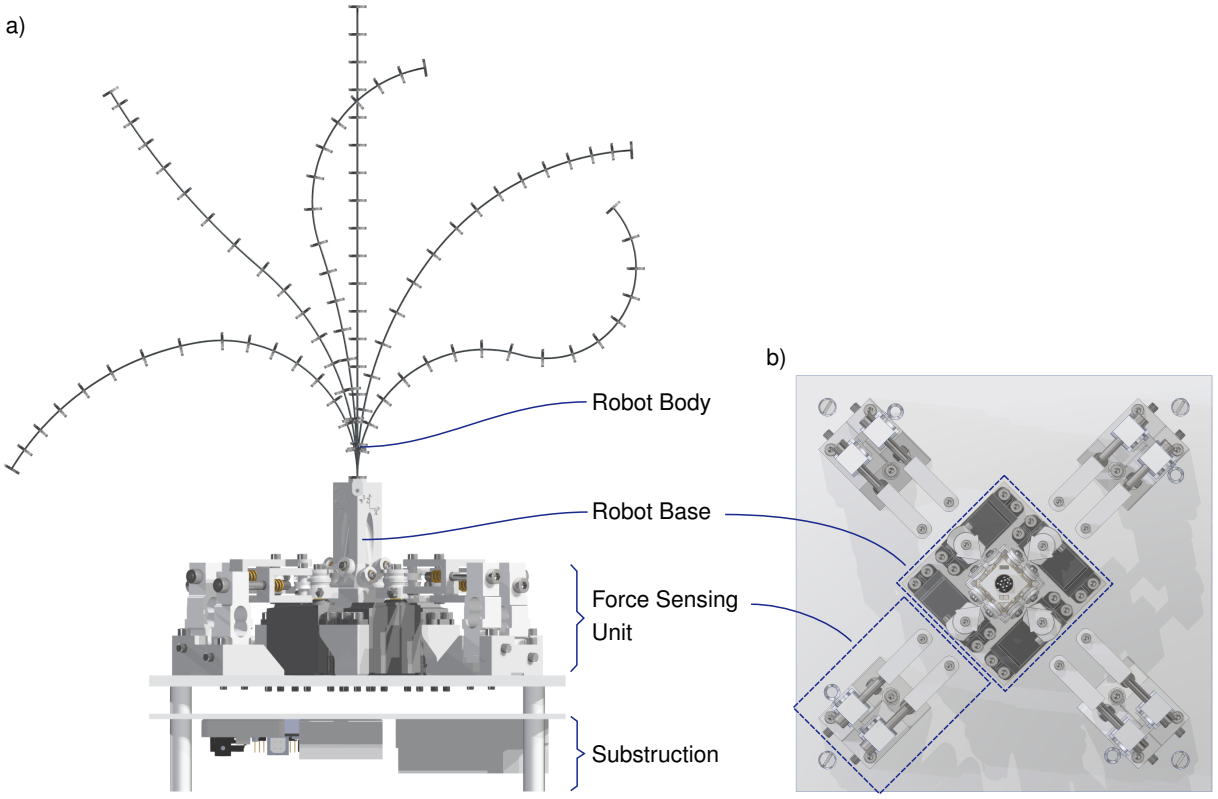

Figure 4.1 – a) The design of the developed robot and various configurations of the robot body, viewed from the front. b) A top view of the robot platform.

Versatile Research Setup As the setup is aimed for research purposes, it should still allow for versatility and adaptability of hard- and software. Therefore, further requirements involve a setup which can still be modified and parts exchanged. Additionally, to support the ongoing development of the robot software, indications of the system's states such as signaling LEDs should be available. While the system should be modular, it should still comprise all necessary peripheral parts such as power supply and onboard low-level control. It should provide an interface to high-level control, ideally through the use of standardized APIs used in research such as the Robot Operating System (ROS)[197]. This will facilitate conducting research studies, support the extension of the system, and enable future integration into advanced robotic research systems and setups.

4.3 Robot Design

From the requirements in Section 4.2, the robot's system design is derived and described in the following. The robot is developed as a tendon-driven continuum robot with two segments with eight sections each. Each segment is actuated by four tendons. In combination with the antagonistic actuation principle described below, the setup minimizes the number of actuators to two per segment, while still providing two DOFs per segment. Table 4.1 lists all symbols used in this chapter and denotes the values for the robot's design parameters for the system, implemented in this thesis.

The robot is divided into four subsystems: The **robot body** forms the actuated continuum structure with two segments and 16 sections. The **base** serves as a mount for the robot body, the actuators, and tendon guidance. Four **force sensing units** redirect the tendons from the

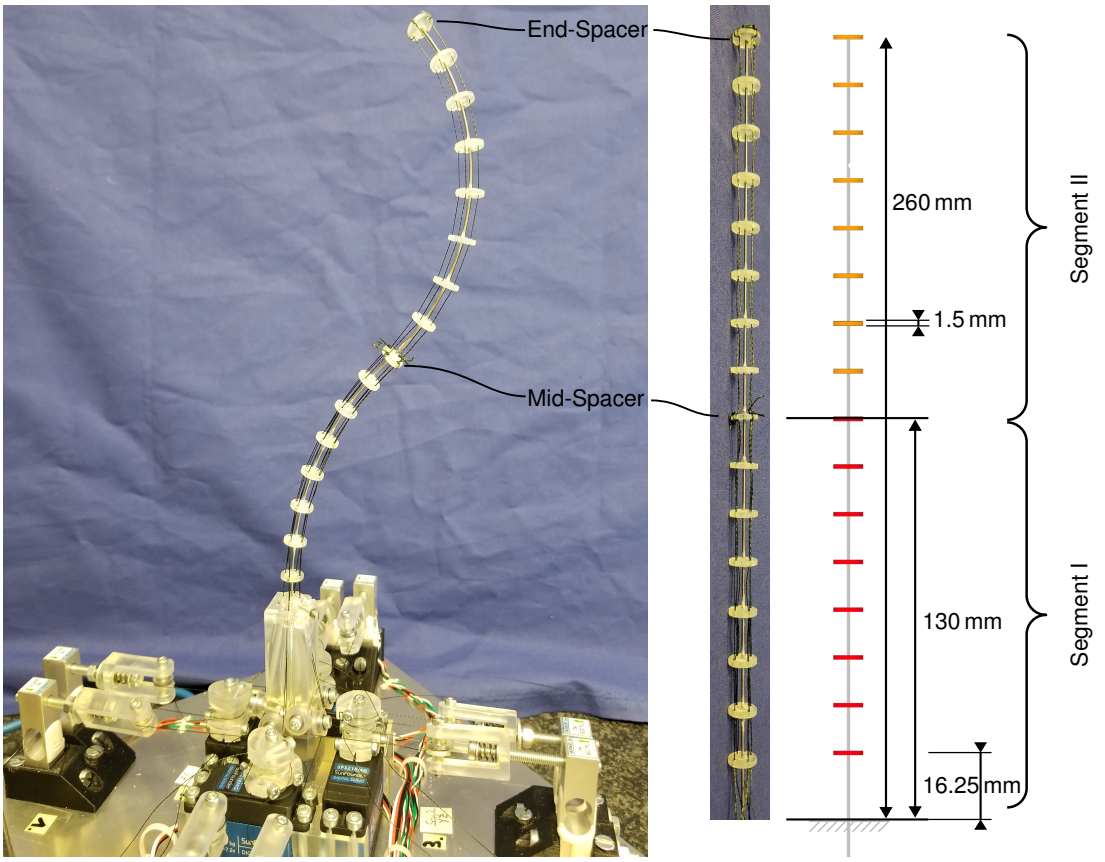

Figure 4.2 – The robot developed in this chapter and its dimensions. The robot body consists of 16 sections, separated by spacer discs. It is separated into two, individually controlled, segments with eight sections each.

actuators into the base and transduce the tendon force. A **substruction** holds control and sensing hardware as well as power supply. Figure 4.1 shows and describes the full robot's design and its subsystems in a Computer Aided Design (CAD) drawing.

The backbone of the robot body consists of a straight $d_{\mathrm{BB}} = 1\,\mathrm{mm}$ diameter NiTi rod with a transformation temperature of approximately $-10\,^{\circ}\mathrm{C}$. This way, the backbone is in its superelastic state (i.e., austenite phase) at room temperature and can provide elastic deformation and restoring force for large deflections without experiencing plastic deformation. Each of the two robot's segments has a length of 130 mm and contains 8 equally distributed sections, divided by spacer discs of thickness $t_S = 1.5\,\mathrm{mm}$. These spacers are 3D-printed by stereolithography (SLA) (Clear Resin, Formlabs Form3, Somerville, Massachusetts, USA) and glued to the backbone. In the following, the proximal segment is denoted as *Segment I*, and the distal segment as *Segment II* (see Figure 4.2). The backbone is placed in the robot base and fastened by a set screw in such a way that the first section exhibits the same length as the other sections. This way a CR is set up with a length of $l_0 = 260\,\mathrm{mm}$ and a maximum diameter of the spacer disk's diameter $d_S = 9.9\,\mathrm{mm}$. The robot's base coordinate system is defined with its origin in the center of the backbone at the point where it exists the robot base. The z-axis is aligned with the robot backbone's axis in the neutral, upright position. X-axis and y-axis are pointing towards the motors and force sensing units.

For actuation, a pair of tendons from braided polyethylene fibers (BeastMaster AX Round Dyneema, Shimano, Osaka, Japan) are attached to a common tendon drum on the robot's actuators. Each segment comprises two pairs of tendons. Each tendon is guided from the tendon drum to the force-sensing units, into a return pulley, and back to the base. A second pulley on

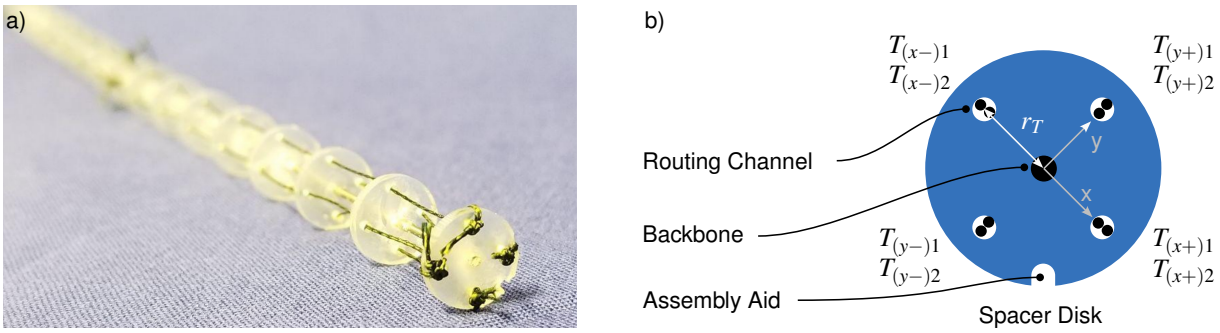

Figure 4.3 – The compliant body of the CR. a) End-spacer with terminated tendons. b) Spacer geometry and routing of the tendons in the spacers with spacer coordinate frame.

the robot's base then directs the tendon upward into the robot's body. Here, the tendons are guided in parallel to the robot's backbone by channels in the $n_S = 16$ spacer discs. The channels are located at a distance of $r_T = 3.5\,\text{mm}$ from the spacer's center. Figure 4.3 shows the spacer discs' design. The tendons for Segment I are terminated in the robot's eighth spacer discs, denoted as mid-spacer. For Segment II, the tendons are terminated in the robot's end-spacer (16th spacer disk). The end-spacer's center marks the robot's TCP.

To displace the tendons, each of the robot's tendon drums is actuated by a position-controlled servo motor (SF3218MG, SunFounder, Shenzhen, China). The motors provide 270° range of rotation and a maximum torque of 2.05 N m. The tendon drum coils the tendons on a radius of $r_{\text{TD}} = 6\,\text{mm}$, on two separate planes of rotation, at a distance of 5 mm to avoid entanglement (see Figure 4.4). Each tendon drum actuates two tendons that are coiled around the drum with opposite sense of rotation. This way, the rotation of the tendon drum around an angle θ results in the shortening of one tendon and the lengthening of the opposing tendon by the same amount (see Figure 4.5). With the servo angle θ denoted in radian, this displacement d given by

$$d = \theta r_{\text{TD}} \tag{4.1}$$

A pair of antagonistic tendons is terminated on opposing sides of the end- or mid-spacer. When a tendon is shorted, the robot body bends towards the side of the shortened tendon. As the opposing tendon is lengthened it provides enough tendon to allow for such bending (see Equation 4.4). Each segment is controlled by two pairs of tendons with orthogonal bending planes to provide each segment with 2 DOFs. The following list gives an overview of how the robot's four motors M_{X1} to M_{Y2} actuate the eight tendons $T_{(\text{x+})1}$ to $T_{(\text{y-})2}$ and affect the bending of the robot's segments, from a neutral upright position. A positive tendon index "$_+$" indicates the tendon which is shorted for bending in a positive direction:

- Segment I (proximal)
  - M_{X1} actuates $T_{(\text{x+})1}$ and $T_{(\text{x-})1}$ to control x-bending.
  - M_{Y1} actuates $T_{(\text{y+})1}$ and $T_{(\text{y-})1}$ to control y-bending.
- Segment II (distal)
  - M_{X2} actuates $T_{(\text{x+})2}$ and $T_{(\text{x-})2}$ to control x-bending.
  - M_{Y2} actuates $T_{(\text{y+})2}$ and $T_{(\text{y-})2}$ to control y-bending.

Figure 4.4 provides visualizations of tendon routing and motor placement. The robot is set up in such a way, that a positive (i.e., counter-clockwise, when viewed from the top) rotation $\theta > 0$

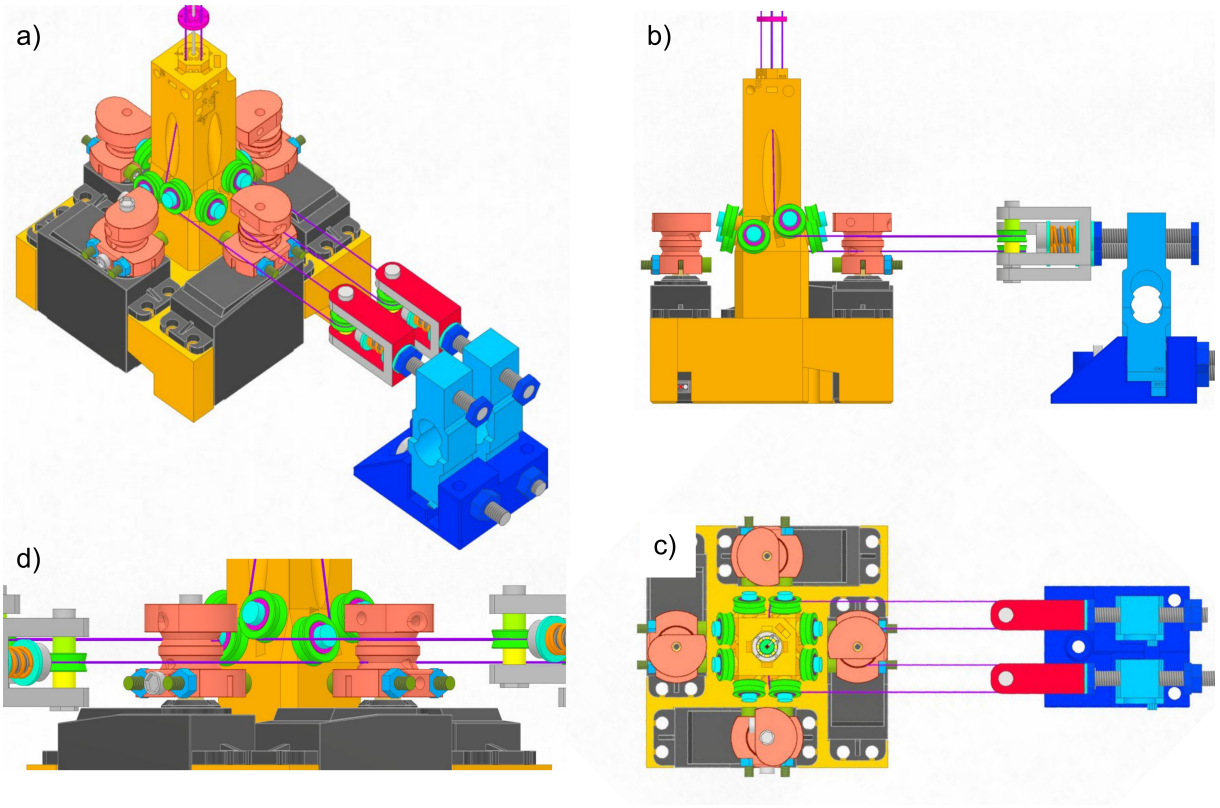

Figure 4.4 – Multiple visualizations of the routing of the tendons for robot actuation. Both tendons of an antagonistic pair of tendons are coiled by one servo motor with an opposing sense of rotation. The tendons are guided through a return pulley where force is measured and slack is picked up. Then another pulley on the robot's base directs the tendon into the robot's body. a) Diagonal view. b) Front view. c) Top view view. d) Front-side view. [9].

of the servos M_{X2} and M_{Y2}, results in $d > 0$ (as given in Equation 4.1) and bending in positive x-direction of Segment II. Due to the symmetry of the setup, M_{X1} and M_{Y1} servo rotation is inverted (i.e., $\theta > 0$ is defined as clockwise rotation) to achieve equivalent relations.

To measure the tendon force, the tendons exert on the CR-body, each sensing unit provides two load cells (Miniature LC TAL220B Sparkfun, Boulder, USA) with a nominal force of 50 N, to measure the force of both antagonistic tendons of one pair individually. The return pulleys in the force sensing units are spring-mounted on the load cell to allow for tensioning of the tendon in case of slack. The load cells and pulley mounts are designed to allow for tendon routing parallel to the load cells measuring direction. This way, tendon force F_T can be estimated from the force measured by the load cell F_{LC} by

$$F_T = 0.5 F_{LC}. \tag{4.2}$$

Figure 4.5 shows the tendon-driven actuation concept for one segment and one DOF. In this thesis, constant curvature bending of the backbone is assumed. A displacement $d > 0$ results in the bending of the robot's backbone at a radius r. From the geometric representation in Figure 4.5, the displacement d required for a given radius is derived from the shortened tendon's length l_S by

$$d = l_0 - l_S = l_0 - 2n_s(r - r_T)\sin\frac{l_0}{2n_S r}. \tag{4.3}$$

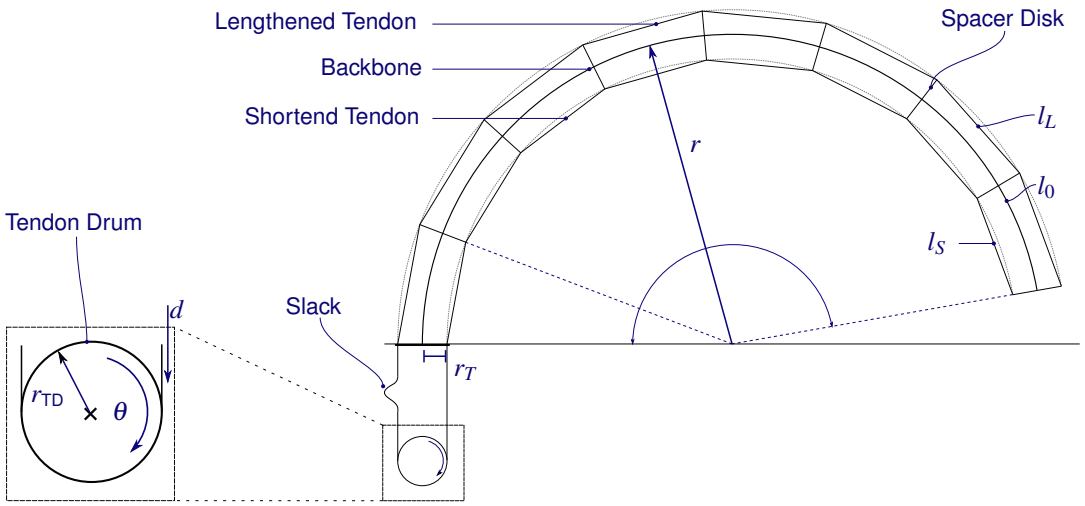

Figure 4.5 – Antagonistic actuation principle of the tendon-driven continuum robot. The illustration shows the actuation of a single DOF, with slack visualized. The backbone of length l_0 is bent when a displacement d is induced by the tendon drum rotation θ. The resulting robot bending radius r depends on the tendon drum radius r_{TD} and the tendon distance from the backbone r_T as shown in Equation 4.3 [9].

In the same configuration, the lengthened tendon requires a minimum additional length of d' to allow for such a bending. This can be calculated from the lengthened tendon length l_L by

$$d' = l_L - l_0 = 2n_s(r + r_T)\sin\frac{l_0}{2n_S r}. \tag{4.4}$$

Slack arises for the lengthened tendon, as the displacement d from the tendon drum exceeds the required displacement d' for lengthening. From Equation 4.3 and 4.4 the amount of slack d_S is quantified by

$$d_S = d' - d = l_0 - n_S r\sin\frac{l_0}{2n_S r} \geq 0 \tag{4.5}$$

for a given segment configuration (i.e., r in this case). In the presented robot system, this slack is compensated by the force-sensing unit's return pulleys. They are mounted on spring-driven tensioning mechanisms (see Figure 4.4). From Equation 4.3, it can be seen, that the shortened tendon defines the robot's shape. Therefore, in the following, d is used as a representation of the actuator state, describing the shortening of the (+)-tendon for $d > 0$ and a shortening of the (-)-tendon for $d < 0$ with d being determined by Equation 4.1.

The robot's substruction serves as a mount for the robot's subsystems and as a housing of peripheral components. A rectangular aluminum plate of $a_{\text{BP}} = 230\,\text{mm}$ side length and 5 mm thickness, provides mounting threads for the robot base and the force sensing units. Further holes allow for the feedthrough of cables from the load cells and servo motors. A second mounting plate below provides further threads for underside mounting of peripheral electronics. A distance of 10 mm between both mounting plates allows for cable management and modularity. The substruction is mounted on four 40 mm long posts with rubber feet for stable placement.

Peripherals required for the operation of the continuum robot are a microcontroller for servo control, measurement electronics for force measurement, and power supply. The servo motors are controlled by an Arduino Uno (Arduino S.r.l., Monza, Italy). A custom shield provides connectors for the servo motors and eight addressable RGBW-LEDs mounted on the robot's

base. The robot's firmware implements signaling sequences on turn-on and turn-off signals over a serial interface. The load cells are read out by 4-channel Wheatstone bridges (PhidgetBridge 4-Input, Phighets, Calgary, Canada) with a Universal Serial Bus (USB)-Interface. Two of these provide the raw data for all tendon forces to a connected computer. A 50 W power supply provides a supply voltage of 5 V to all electronic components. This way, the robot setup comes with all required means for its operation and only interfaces to a single 230 V outlet and USB for connections to a computer for high-level control.

The robot's four servo motors are controlled by the Arduino, which provides a serial connection over USB to a connected computer. The robot's high-level control should allow to be interfaced via ROS (version `noetic`). Therefore, the `rosserial`[1] package is used. It provides a firmware for the microcontroller (i.e., the Arduino) and a ROS-client on the computer. This allows sending ROS-messages from the microcontroller to a ROS-network and vice versa. For the designed robot, four subscribers are implemented, which accept position commands for each servo motor. The Arduino converts these messages to pulse width modulation (PWM) signals which control the servo's position.

The load cells' resistances are sampled and analog-digital converted as voltage ratios by the Wheatstone bridges on the robot's substruction. These voltage ratios are uncalibrated raw values, proportional to the tendon's tension. These values are transmitted to a computer via USB by a driver provided by the manufacturer. A ROS-wrapper was developed, which publishes these raw values to the ROS-network. A custom calibration node calibrates the raw values to provide absolute force readings to the ROS-network. To determine calibration parameters, the node provides a calibration routine, which samples a ground truth from a commercial, calibrated force gauge (PCE-DFG N 10, PCE Instruments, Meschede, Germany) with a resolution of 5 mN. The raw values and ground truth are fitted to a linear calibration function, which is used to map the raw values to a force.

4.4 Workspace Analysis

In the following evaluation, the robot's motion capabilities are to be characterized. A first demonstration provides a general qualitative impression of the robot's dexterity. Then, a workspace analysis is conducted, in which the workspace is sampled for maximum actuator configurations. For an evaluation of the robot's accuracy, a repeatability analysis is conducted.

The two segments of the robot each comprise two DOF. This allows bending of both segments in two axes. Figure 4.6 demonstrates the actuation capabilities for the robot's configuration. The robot's neutral position is its upright position, when all servos are at $\theta = 0$, as in Figure 4.6a. Figure 4.6b shows Segment I in a bent position while Segment II remains neutral, Figure 4.6c shows both segments bent in equal direction, while in d) the robot is "S"-shaped by opposite bending of both segments.

For a qualitative evaluation, eight robot configurations are defined in the actuator space. These configurations represent permutations of the upper and lower limits for each actuator. The configurations are listed in Table 4.2. The robot is driven to a configuration, and its mid- and end-spacer positions are sampled. This measurement is performed with a passive articulated metrology arm (FARO Platinum, Faro Technologies Inc., Lake Mary, Florida, USA), which features a handpiece for measurement of 3D-points in the metrology arm's base coordinate system.

[1] `http://wiki.ros.org/rosserial`

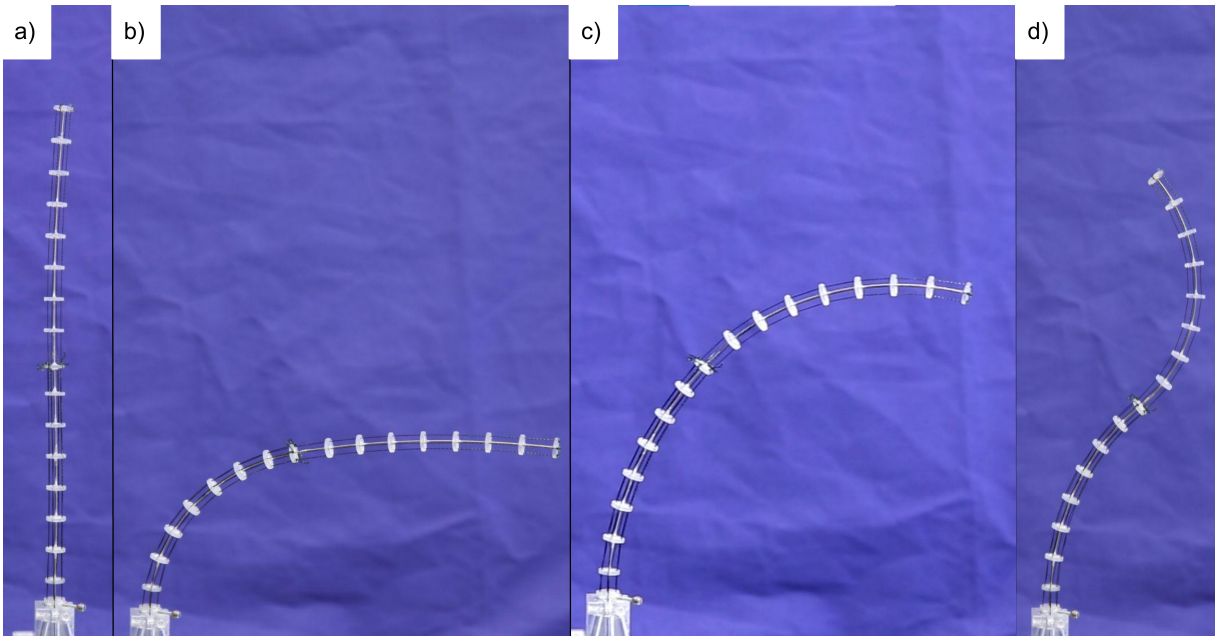

Figure 4.6 – Four major motion capabilities of the designed continuum robot. a) Shows the robot's neutral upright position. In b) Segment I is bent at 90° while Segment II remains straight, c) shows a constant curvature of both segments and d) displays the robot's capability of adopting "S"-Shapes by opposite bending of both segments [9].

Table 4.2 – Robot configurations for workspace evaluation.

Configuration	0	1	2	3	4	5	6	7	8
θ_{X1}	0°	135°	-135°	0°	0°	135°	-135°	135°	-135
θ_{Y1}	0°	0°	0°	135°	-135°	135°	-135°	-135°	135
θ_{X2}	0°	-135°	135°	0°	0°	-135°	135°	-135°	135
θ_{Y2}	0°	0°	0°	-135°	135°	-135°	135°	135°	-135

The 3D position of the handpiece's tip can be sampled on a button press with a precision of 0.037 mm. To determine a spacer's position, four equally distributed locations on the spacer's perimeter are sampled. These measurements are averaged to determine the spacer's center position. To transform the spacer measurements into the robot's base coordinate system, the robot base is also sampled with the metrology arm.

The resulting spacer locations are plotted in Figure 4.7. The figure provides four views of the same data, to allow for a 3-dimensional impression. The sampled spacer positions of each robot configuration are connected by lines to help understand spacer positions belonging to a common robot configuration. In the plots, the robot's origin is positioned at the location $(0,0,0)$. The data shows that the robot workspace extends from −184 mm to 172 mm in x-direction and 172 mm to 178 mm in y-direction. Z-direction range extended from the robot's neutral position at 260 mm to −111 mm below the robot's origin.

Table 4.3 – Robot configuration for repeatability evaluation.

Configuration	P0	P1	P2	P3	P4	P5
θ_{X1}	0°	-8°	-12°	42°	-125°	-9°
θ_{Y1}	0°	31°	-134°	-15°	122°	75°
θ_{X2}	0°	-13°	-6°	-44°	65°	30°
θ_{Y2}	0°	-56°	-63°	95°	54°	126°

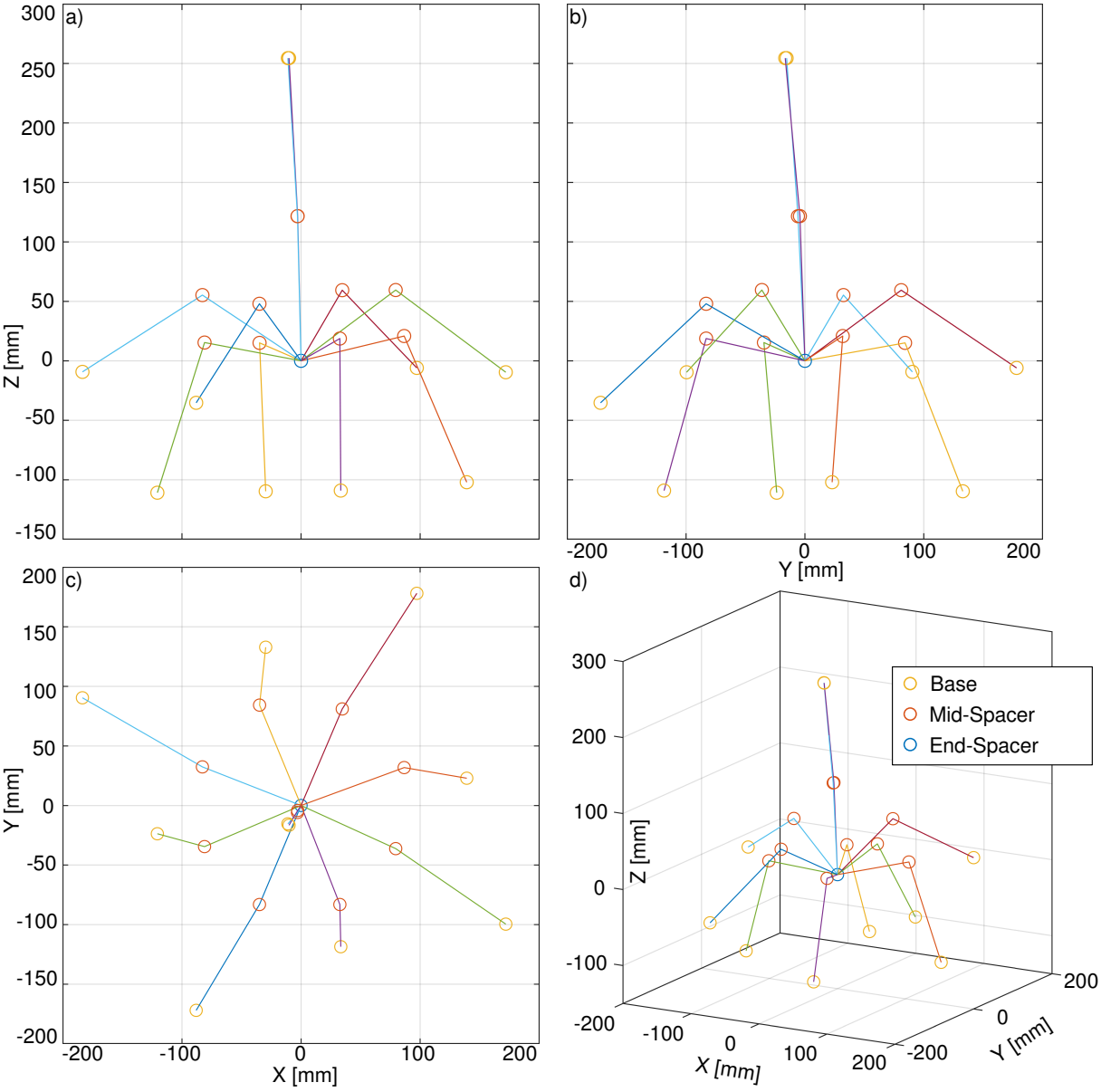

Figure 4.7 – Results of the workspace analysis. The plots show the 3D location data of the robot's base, mid-, and end-spacer. For a 3D impression lateral projects a) and b), top projection c), and a 3D view d) are displayed. Graphic adapted from [9].

To evaluate the robot's accuracy, five random robot configurations are selected and the robot is driven to each of them two times. Mid- and end-spacer positions were measured in each run. The selected configurations are denoted in Table 4.3. For the evaluation, the configurations were set up in the order listed in Table 4.3. At each configuration position measurements are conducted in the same manner as in the workspace analysis. Subsequently, the same five configurations were repeated and measured in the same order again. As a result, for each of the five configurations, two position measurements are available. These are compared to derive a repeatability metric for the robot.

The resulting data is graphed in Figure 4.8. For comparability, the presentation of the data is kept similar to the display of the workspace analysis' results. In the plot, the mean positions of both measurements for one configuration are plotted and connected with lines to represent one robot configuration. As a metric for the robot's accuracy, the distance of both measured positions is evaluated. This error is plotted as blue disks at each location. A disk's diameter

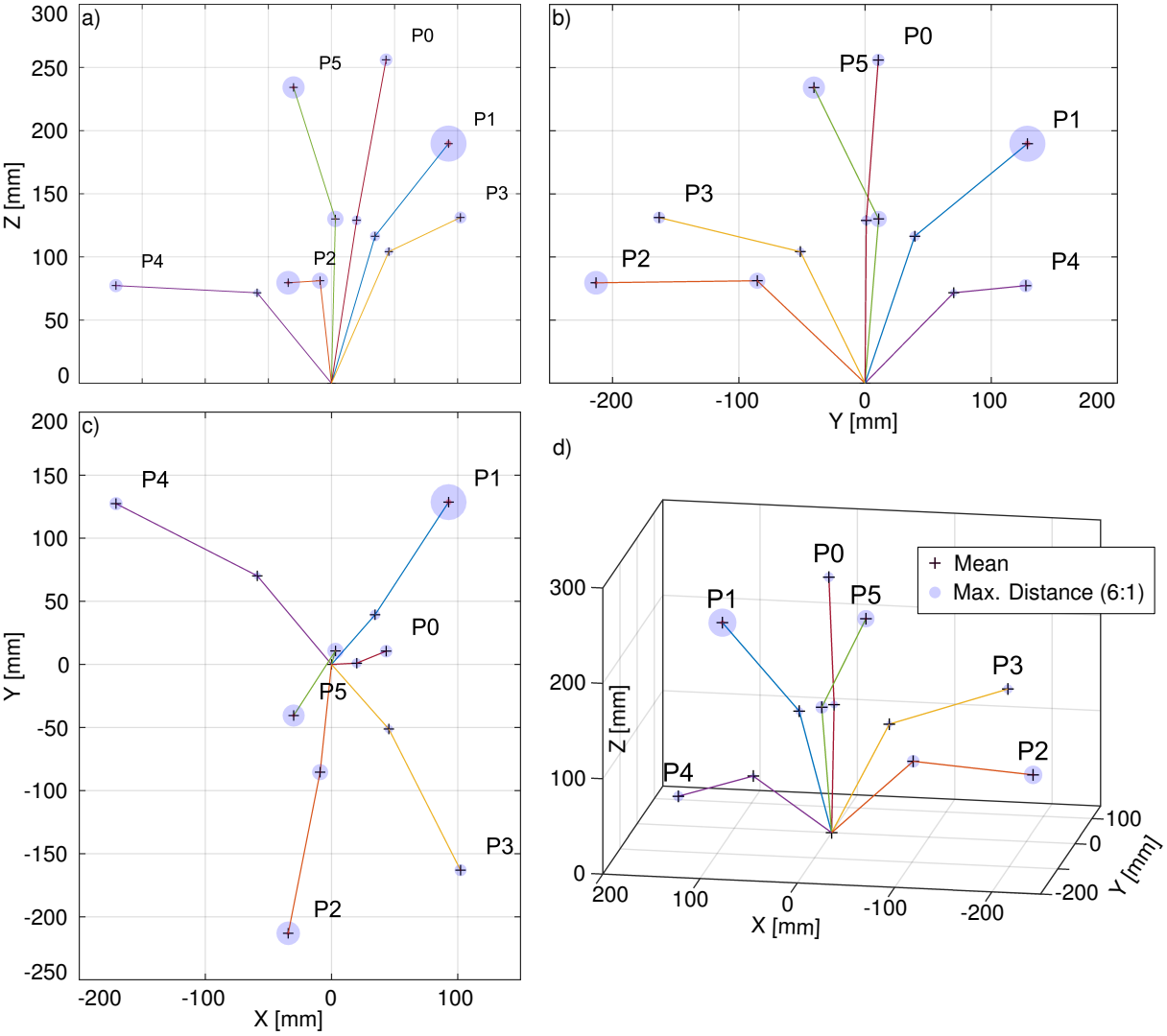

Figure 4.8 – Results of the repeatability analysis. The plots show the mean positions of the robot's mid and end-spacer when assuming configuration P0–P5. The blue circles represent the deviation of a second run (scale by a factor of 6 for better visibility). For a 3D impression lateral projects a) and b), top projection c), and a 3D view d) are displayed. Graphic adapted from [9].

represents the measured error (i.e., the difference of both measurements for a configuration). For better visibility and comparability, the discs are enlarged by a factor of 6. The evaluation resulted in a minimum error of 1.2 mm for the mid-spacers and 1.6 mm for the end-spacers. The maximum error was evaluated to 2.2 mm (mid-spacers) and 4.8 mm (end-spacers). This represents a maximum error of 1.7 % of the robot's length.

4.5 Chapter Discussion

Section 4.2 lists requirements for the robot setup. In the following, the resulting robot is compared to these requirements. As an actuation technology, tendon-driven actuation was applied and a new method for antagonistic actuation was introduced to address the challenge of keeping the footprint small and the volume for integration low. Nevertheless, the robot can provide tendon measurement for each tendon and integrates all required peripherals in its setup. The robot exhibits an outer diameter of 10 mm and a full length of 260 mm, providing a high aspect ratio

(length to width), necessary for MIS. The robot incorporates 4 DOFs, however, the conducted experiments show that the Segment II DOFs are strongly influenced by the actuation of Segment I. To achieve independent bending, a more complex control and model is required which includes M_{X1} and M_{Y1} in the control of Segment II and M_{X2} and M_{Y2} in the control of Segment I. Proprioceptive tendon force sensing is implemented in the system presented, fulfilling the requirement. It can provide eight tendon force measurements to a higher-level controller. The system can be reconfigured (e.g., the robot body or peripherals exchanged) in a facile manner. However, this requires recalibration of the tendon's tension and tuning of the robot's neutral position. To do this, the tensioning mechanism must be manually adjusted for each tendon until a straight upward position can be achieved and no slack is present in the neutral position. On the one hand, further investigations to improve modularity could research suitable tensioning mechanisms, that facilitate tensioning. On the other hand, an automated calibration of the robot using the tendon force sensors could be investigated. Addressing the requirement of a versatile research setup, the control interface to ROS provides versatility of control in various research setups, even for control over a network.

The presented robot implements a novel antagonistic actuation method with only one motor for a pair of tendons. In contrast to [66], the design is optimized for a compact setup, suitable for the OR. While [99] also focuses on medical intervention, their approach allows only for sensing a force difference of both antagonistic tendons. Only the presented method allows for an absolute tendon force measurement for each tendon.

From the results presented in the workspace analysis (see Figure 4.7), a shift of the planes of motion could be observed. Intuitively it would be expected that an exclusive θ_{X1} motion would result in bending solely in the x-z plane. Figure 4.7 indicates, that the axes of motion are rotated at approximately 20°. This could be explained by the manual fabrication process of the robot body and thus introduced imperfections of the setup. While an assembly help is utilized for spacer distancing and alignment on the backbone, the positioning and alignment of the robot body in the base and the introduction of the tendons is still a manual procedure, limited to manual accuracy. It is also possible that displacements of the spacers occur after assembly, as the bonding of the spacers to the NiTi is challenging.

The evaluation only analyses static cases. It could be observed that the structure was prone to overshooting at the end of its motion due to its long and compliant body. Therefore, the robot positions were only acquired after the robot has come to a complete stop. For dynamic use cases, the robot's dynamic characteristics need to be examined, and options for a dynamic model and suitable controllers can be investigated.

The evaluation method for the robot's accuracy and repeatability is time-consuming and results in only a small number of samples for evaluation. For a more thorough evaluation of the robot system, a method for a contactless and automated sampling of the robot's spacer position should be investigated. Here, possibly an image-based tracking system could be applied. As the robot's motion should not be affected, a marker-less solution would be favorable.

To improve the robot's accuracy, future work could investigate the improvement of manufacturing and assembly or the integration of shape sensing for a closed-loop control. A calibration of the robot motion would be useful as well, as the system displayed a systematic error which could be reduced by thorough calibration. However, for application in medical scenarios, often an absolute positioning of a flexible instrument is not a primary concern. An endoscopist controls a flexible endoscope not for positioning it at an absolute position, but rather in a way, that its tip is in an optimal position relative to the direct surgical environment. E.g., this is the

case for the application of therapeutic instruments on the surgical situs, or to provide the best view for a distal camera. Therefore, in the following chapter, a proximity sensor is presented which should provide such spatial information to the surgeon or an automated system. Integrated into the presented robot system, it should enable the CR to be autonomously controlled in relation to its surrounding environment.

5 Capacitive In Situ Spatial Sensing

MIS is lacking in situ sensing which can be integrated without disturbing the surgical workflow and does not significantly increase an instrument's size. Capacitive sensing provides an option for very thin and disposable transducers while still economically efficient. Thus, this chapter introduces a method of creating such a sensor for minimally invasive scenarios. To utilize the sensor information in a minimally invasive scenario, a method for localization, based on capacitive proximity sensing, is introduced. The sensor developed and applied in this chapter is based on works from Hosam Alagi and Prof. Björn Hein, who supported this work substantially. Section 5.2 concentrates on the sensor architecture (Section 5.2.2), its processing (Section 5.2.3 and an evaluation (Section 5.2.4) of a sensor providing proximity feedback and relative localization for a minimally invasive instrument. The kick-off for this topic was given through the prototype, Olivia Rau developed in her Master's thesis, advised by Prof. Jan Gerrit Korvink and supported by medical advice from Prof. Jochen Hampe. With their support, this work could be published successfully at the International Conference on Robotics and Automation (ICRA) 2021 [10]. The experimental research on the electroplating of SLA prints, presented in the discussion (Section 5.4.1) was supported by Jonas Kett through his Master's thesis. Section 5.3 demonstrates the sensor's versatility in an application in a magnetic flexible endoscope for multi-contact sensing. This work was made possible by the support of Nikita Greenidge, James Martin, and Prof. Pietro Valdastri at the University of Leeds and is currently prepared for publication at the IEEE Robotics and Automation Letters (RAL) [11]. As a reference, Table 5.1 lists all symbols introduced in this chapter.

Table 5.1 – List of symbols introduced in this chapter

Symbol	Parameter	Symbol	Parameter
E_S	Sensor Electrode	d_i'	Real Electrode Distances
E_g	Guard Electrode	r_m	Measured Radius
A_e	Electrode Surface	r_m'	Real Radius
Sig	Voltage Source	$\boldsymbol{p} = \begin{bmatrix} p_x \\ p_y \end{bmatrix}$	Position of the Sensor
SW	Electrode Switch	$\boldsymbol{p}_n$	Relative position
f_S	Sensing Frequency	r_P	Cylindrical Phantom's Inner Radius
R	Resistance	$_C$ and $_{EX}$	Indices for copper and ex vivo Phantom
C	Capacitance	n	Number of Experiments
A	Capacitor Surface	E	Error of the Relative Position
d	Capacitor Plate Distance	$E_{\_,m}$	Maximum Error
C_{PP}	Ideal Capacitance	σ	Standard Deviation
ε_0	Vacuum Permittivity	c_i	Contact Value of an Electrode
ε_r	Relative Permittivity	τ_i	Contact Threshold
C_0	Parasitic Capacitances	M_i	Median
i	Sensing Unit Channels	μ_{i1}, μ_{i2}	Means of Gaussian Mixture Model
E_i	Electrode Raw Values	a_i	An Electrode's Confidence
d_i	Measured Distances	q_g	A Pad's Contact Value
g	Contact sensor pad		

5.1 Introduction

MIS challenges surgeons with operating with no direct line of sight to the situs. For navigation, they rely on their anatomical knowledge, preoperative images, and endoscopic images. The latter comes with limitations regarding field of view, resolution, illumination, and depth perception, which results in a minimally invasive intervention being significantly more demanding than open surgery. To restore the lost perception and provide assistive functions, the sensorization of surgical and diagnostic instruments is investigated. Here, the challenges lie in finding sensing methods that satisfy the demanding requirements of MIS, especially regarding size and compatibility with surgical processes and sterilization. Research in this field, however, mostly focuses on the restoration of haptic information. Various works present miniaturized force sensors and their integration into surgical robots and tools [152, 153]. Additionally, the integration of such sensors is mostly demonstrated in rigid instruments, and transferability to flexible tools remains an open research question.

Investigated sensing methods for such sensors are mostly based on strain gauges [154, 155, 195] or optical fiber-based displacement sensors [157, 159]. In force sensing, capacitive methods have been applied as well. Such setups incorporate two electrodes as a displacement sensor on a deformable structure which allows the estimation of a force applied, from a given displacement [183, 191, 198]. However, capacitive sensing is also suitable for proximity sensing. While it is well-established in an industrial context, in MIS, the application of capacitive proximity sensing methods in instruments or robots has not yet been reported.

Capacitive sensing offers a simple and cost-efficient method for proximity sensing, as for a transducer, only conductive surfaces are required. This could leverage the implementation of disposable add-ons such as drapes with proximity sensing capabilities. Therefore this chapter investigates a method to utilize capacitive sensing for proximity sensing in a medical context. To demonstrate its application, a sensor is developed, that provides proximity information that can be used for relative localization of an instrument's distal tip in a closed environment. Such information could be valuable feedback during navigation with a minimally invasive instrument or endoscope and help the surgeon or a robotic system to regain perceptive information on the situs in a minimally invasive procedure.

5.2 Capacitive Proximity Sensor

This chapter introduces methods of applying capacity-based proximity sensing. The concepts of capacitive sensing, introduced in Section 3.3.2, have so far not been applied in a surgical or minimally invasive context. For such a method, a setup is considered, where a sensing electrode and the tissue in its proximity, form a capacitor of capacitance C. Based on the human model, defined in the Electrostatic Discharge (ESD) standard [199], we assume that a patient in the OR is grounded with a resistance of $1500\,\Omega$ and a capacitance of $100\,\mathrm{pF}$. From [173] we adopt, that this can be neglected for the following measurement principle. Based on this assumption, in the following experiments, grounded conductive surfaces are used as phantoms for evaluation and characterization. The modeled scenario is depicted in Figure 5.1. In a first approximation, we model the physical setup of the sensing electrode and tissue as an ideal parallel plate capacitor and apply Equation 3.2: As surface A the electrode's surface is used, the second plate is formed

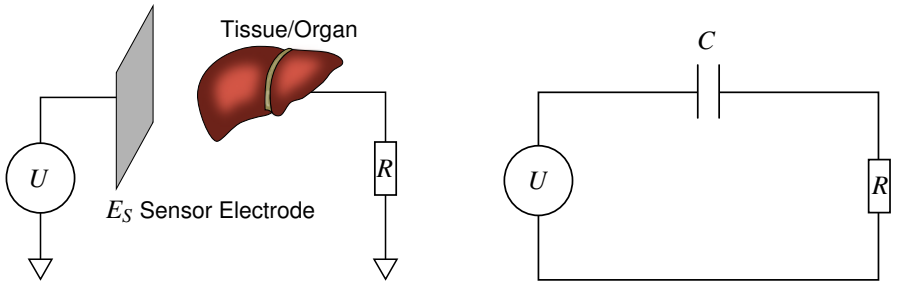

Figure 5.1 – Modeling of the sensing scenario and equivalent circuit. The sensor electrode E_S and an organ are modeled as two plates of a capacitor setup with a capacitance C. A voltage U is applied to the sensing electrode and the organ is assumed to be grounded through a resistor with a resistance R.

by the tissue at distance d. This setup's capacitance C_{PP} is then given by

$$C_{\mathrm{PP}} = \varepsilon_0 \varepsilon_r \frac{A}{d}, \tag{5.1}$$

where ε_0 is the vacuum permittivity, and ε_r is the relative permittivity of the medium in between both plates. It can be seen that, by moving the sensing electrode away from the tissue (i.e., distance d increases), C_{PP} decreases inversely proportional to d. This correlation is the foundation of the proximity sensor's working principle. In a measurement setup, the electrode setup but also the circuit and cables exhibit parasitic capacitance, which adds to the measurement. To account for these effects, the model is extended by a parallel capacitor C_0 combining all parasitic capacitances. A measurement circuit then reads a capacitance of

$$C = C_0 + \varepsilon_0 \varepsilon_r \frac{A}{d}. \tag{5.2}$$

As a realistic measurement scenario diverges significantly from the described setup of an ideal parallel plate capacitor, the parameters of electrode surface A and permittivity $\varepsilon = \varepsilon_0 \varepsilon_r$ of medium between the plates are assumed as unknown but constant. Thus, the uncalibrated measurement setup forms a proximity setup, which can be empirically calibrated to derive distance measurements.

Based on the described method, capacitive sensing allows integration of thin electrodes onto the outer surface of a minimally invasive instrument. To prove this concept, an add-on sensor is developed, which allows for the integration of proximity sensing into an endoscope or minimally invasive tool. The following section also presents a method to utilize the proximity data to provide localization in a minimally invasive environment.

5.2.1 Sensor Requirements

To address the challenge of restricted perception in MIS, and provide data that can be utilized for localization, a sensor technology is required, that can provide distance information in multiple directions, especially outside of an endoscope's field of view. In a minimally invasive setting, a surgical or diagnostic instrument is surrounded by tissue. This circumstance can be exploited to determine an instrument's relative location at the situs. In most cases, this information is more relevant to the surgeon than an absolute position (e.g., the instrument's distal tip in its proximal base coordinate system). This is because in MIS a surgeon needs to manipulate tissue relative to the situs, not relative to a global coordinate frame. Especially in soft tissue interventions such as

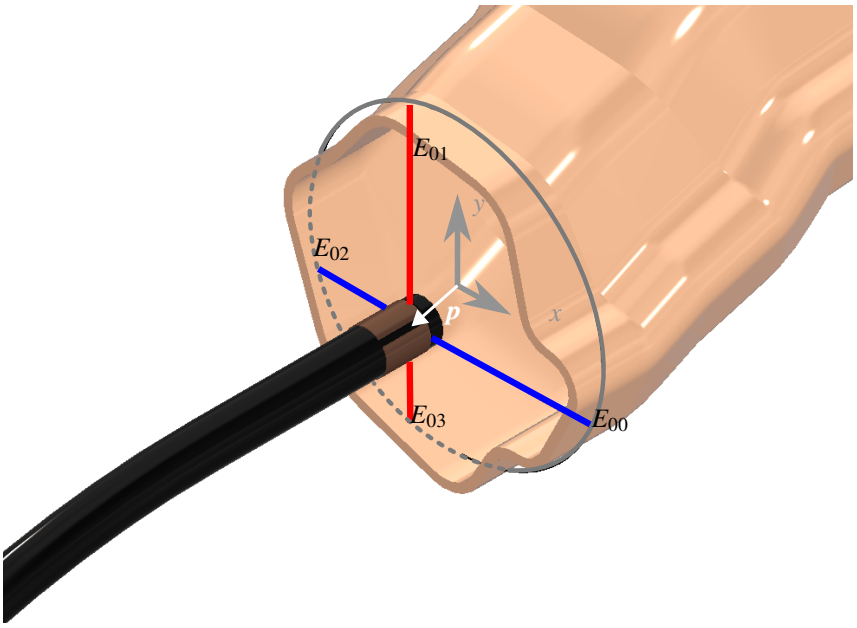

Figure 5.2 – Usage of proximity sensing for localization in a hollow organ.

colonoscopy, the absolute position (e.g., from preoperative imaging) of an organ in the body, can deviate significantly at the time of the intervention. To be applicable in such an environment, such a sensor should fulfill the following requirements:

Size The sensor should integrate well into a minimally invasive instrument. This means the instrument's radius should not increase significantly. This allows to keep an established surgical workflow and avoids additional trauma or pain as a result of sensor integration.

Versatility The sensing method should allow for instrument-independent application. Its principle should apply to any rod-like rigid or flexible instrument. As a demonstration for application, a prototype should be fitted to a commercial flexible endoscope with a tip of 9.2 mm diameter (Video-Gastroscope 13800PKS, Karl Storz, Germany). The sensor should be detachable to allow for usage in other applications and its integration should not require opening the instrument.

Measurement Range Colonoscopy is an endoscopic intervention in one of the largest hollow organs in the human body. As the colon is inflated during the intervention, its inner lumen can assume diameters up to 60 mm during colonoscopy [200]. The sensor should therefore provide sufficient range to cover such a distance.

Number of Electrodes A localization algorithm should determine the instrument's centering in a tubular hollow organ. To achieve this, sensing of at least three distances in a plane of measurement is required.

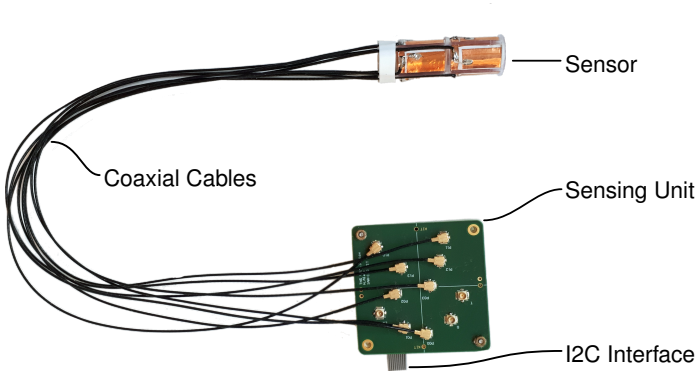

Figure 5.3 – Full sensor system with electrodes, sensing unit, and connecting cables.

5.2.2 Sensor Architecture

Capacitive measurement comes with the challenge of being receptive to several varying influences, such as humidity, parasitic capacitances, or the influence of cabling. To derive useful data, a relative measurement method is suggested. It combines the clinical need for relative localization data and a capacitive measurement principle that is based on a comparative measurement principle to reject common errors on all electrodes.

While three distance readings would be sufficient to reconstruct the radius of a tubular environment (cf. [132]), the suggested approach makes use of four electrodes to provide four proximity readings to the sensor system. This brings the advantage, that two opposing proximity readings can be compared to derive a relative position which remains unaffected by a common error applying to both electrodes. Additionally, four proximity readings also enable the reconstruction of an elliptical environment. The concept for this localization method is visualized in Figure 5.2.

For the implementation of the capacitive sensing, the method presented by Alagi et al. is applied [166, 173]. Figure 5.3 and 5.4 show the implemented sensing unit. To fulfill the requirements defined, the sensor's electrode design is set up as follows. A 3D-printed (Clear Resin, Formlabs Form3, Somerville, USA), tubular scaffold can be attached to a commercially available flexible endoscope. It integrates eight electrodes which are positioned in two rings of four electrodes each. In one ring of electrodes four electrodes are equally distributed over the perimeter of the scaffold (see Figure 5.5). All electrodes are equally sized as rectangles with a surface of $A_e = 11\,\text{mm} \times 6\,\text{mm} = 66\,\text{mm}^2$. The electrodes consist of an outer sensing electrode layer, transducing the capacitive signal and an inner shielding layer, to achieve directivity away from the sensor center. This way, the signal is concentrated on objects in front of each electrode, and a signal from objects approaching from the electrode's side or back is suppressed. The electrodes are connected to the sensing unit by coaxial cables. Figure 5.5 shows the sensor setup and its dimensions.

The sensor is assembled by hand. Electrodes and shields are cut from adhesive copper tape (CFT-50/10M, Tru Components, Conrad Electronic SE, Hirschau, Germany). The shielding layer is placed in the scaffold, then a layer of electric tape is used for insulation, and finally the electrode from copper tape. The electric tape isolates the electrode and shielding layer and serves as a distancer between both. A coaxial cable (MCRF-to-Pigtail 73116-0077, Molex, Wellington, USA) with a diameter of 0.81 mm is used to connect the electrodes to the sensing unit. Such a cable shields the electrode's signals from outer influences over the length of the cable up to the sensing unit. The coaxial cable's outer conductor is soldered to the shielding

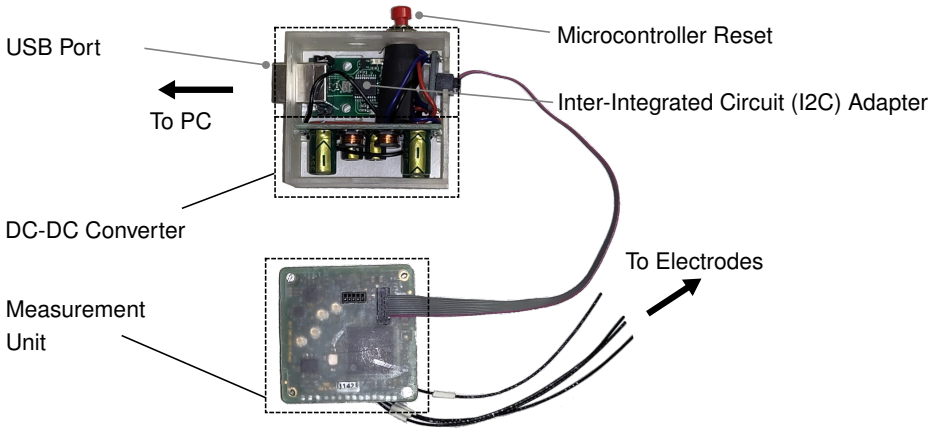

Figure 5.4 – Power and data adapter for the sensor unit. A USB connection provides a data interface to a computer and provides power to a DC-DC converter for ±12 V supply of the sensor.

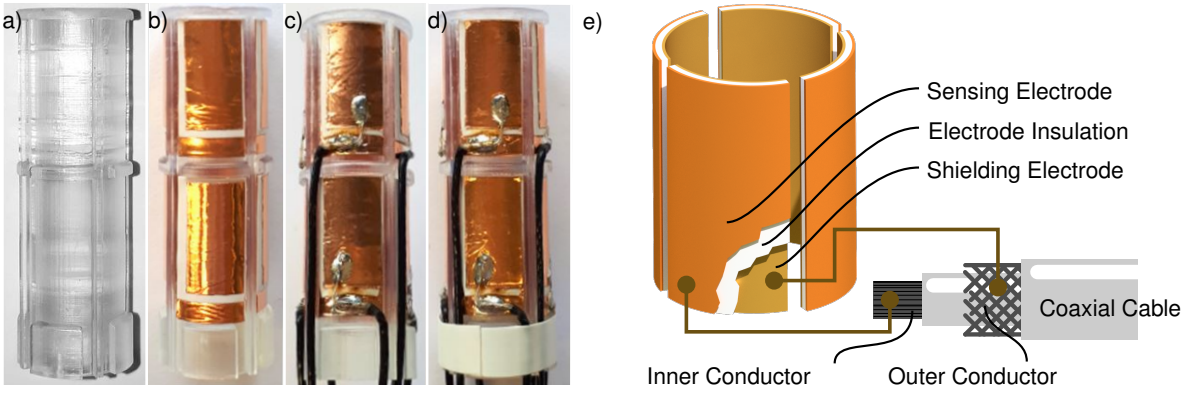

Figure 5.5 – Manufacturing steps and the ready-to-use add-on sensor. a) The 3D-printed scaffold. b) Shielding Electrode, Insulation, and Sensor Electrode in place. c) Coaxial cables soldered to the electrodes. d) Finished sensor with fixated cables. e) Visualization of the electrode arrangement and connection with the coaxial cable.

electrode, the inner conductor is connected to the sensing electrode. The electrode assembly is visualized in Figure 5.5

The sensing unit provides coaxial connectors for electrode readout. Figure 5.6 shows the sensing unit's working principle [166]. An excitation voltage source *Sig*, creates a sine voltage with a frequency of f_S. A software-controlled switch *SW* is configured to iterate through the sensing unit's eight channels $i \in \{00, 01, 02, 03, 10, 11, 12, 13\}$. A voltage follower provides the shielding electrodes with a common shielding signal. On each channel, the time course of the current is sampled as a voltage over a shunt resistor R. A microcontroller (µC) extracts the signal's phase and amplitude. The sampled amplitude is represented as a unitless integer raw value that is proportional to the capacitance. By serially switching through the channels, these raw values E_i are sampled for each of the sensing unit's eight channels. The µC interfaces to an I2C bus, on which this raw data is transmitted.

To transmit the data to a PC an USB-I2C-adapter (RB-Dev-41, Davantech, Attleborough, England) is used. The sensing unit provides a connector for a flat ribbon cable. This cable transmits the sensor's I2C bus, a reset signal lane, and power supply of −12 V and 12 V to the sensing module. To allow for operation from USB alone, a DC-DC converter is integrated into a common housing with the USB-I2C-adapter and provides the required ±12 V as well as the I2C bus to a connector. This combined power and data adapter is pictured in Figure 5.4

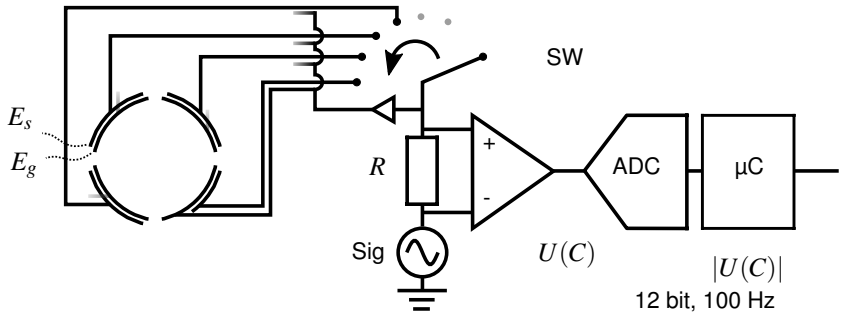

Figure 5.6 – Simplified working principle of the capacitive sensor unit, as presented in [166]. A sinusoidal voltage source induces a current in one of the electrode's channels E_S, as selected by the software-controlled switch SW. This current is measured and converted to a digital value, transmitted, and I2C bus by a µC. A voltage follower provides a shielding signal for coaxial cables and the shielding electrodes.

Through the I2C and USB interface, the sensor raw data can be read out on a computer. Here, a custom ROS1 node allows configuration of the sensing unit and publishes the values to a ROS-network for further processing and usage.

5.2.3 Sensor Characterization and Data Processing

For sensor characterization and calibration, the sensor's raw data is compared to its distance to an object. Therefore, the setup depicted in Figure 5.7 is used. The sensor is mounted on a Stewart Platform (M-850, Physik Instrumente GmbH, Karlsruhe, Germany) which allows high precision movements of 2 µm repeatability. On top of the robot, a mount holds a phantom attached to a FTS (F6D-80e-60, ME-Meßsysteme GmbH, Hennigsdorf, Germany). For sensor characterization, a flat plane phantom is used. It consists of a 3D-printed, 10 cm × 10 cm plane with mounting holes to attach it to the FTS. It is covered with copper foil to form a conductive surface that is grounded with a cable. As introduced earlier, this allows for a sufficient representation of approaching tissue. The sensor is mounted on the robot's TCP in such a way, that the normal at the center of the electrode which is to be characterized, is pointing towards the phantom and is aligned in parallel to the robot's x-axis. The sensor is then driven towards the phantom until the FTS detects a contact. From this point, the sensor is moved backward again (i.e., negative x-direction), while the sensor's raw values and the distance from the phantom's surface are sampled and stored. This way, data tuples are sampled, which allow for characterization of the sensor. Through one such an experiment run, two vertically aligned electrodes can be characterized at once. For the other pairs of electrodes, the sensor is rotated by 90° and the run is repeated. From this characterization, a sensor calibration for each electrode is derived by conversion to a lookup table, which assigns each sensor raw value E_i a distance d_i. Figure 5.8 plots this calibration for the implemented sensor. The sensor's coordinate frame is defined with its origin in the upper sensor ring's center. The z-axis is aligned with the sensor's central axis, the x-axis is directed through electrode E_{00}, and the y-axis through electrode E_{01}. This results in the right-handed coordinate frame visualized in Figure 5.8.

Even though the sensor values have been calibrated to distances, they are regarded as proximity values, as unpredicted errors such as a change in the environment's grounding, humidity, and cabling can affect the sensor's raw value during run time and falsify an absolute distance reading. Under the assumption, that such errors occur equally on all electrodes, a relative measurement concept is applied: Each measured distance d_i is seen as affected by a constant error

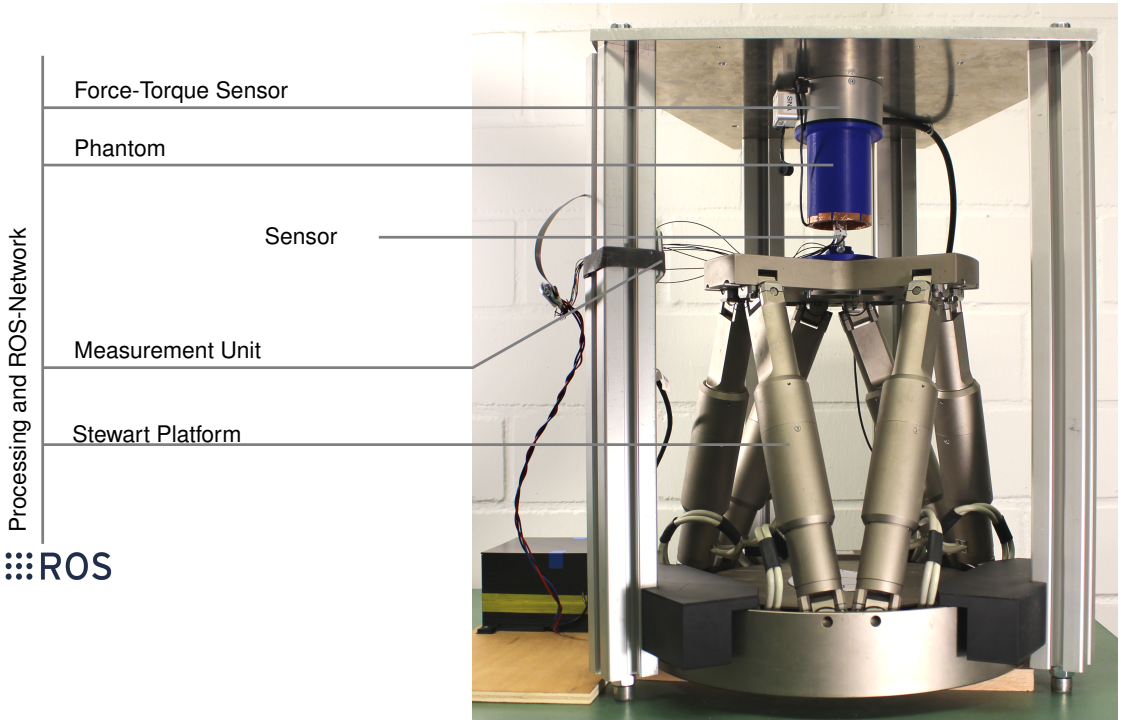

Figure 5.7 – The evaluation and calibration setup used for characterization of the proximity sensor. A Stewart Platform can position the sensor to an evaluation phantom (depicted here) or a calibration phantom. The phantoms are attached to a FTS to allow the detection of contact [10].

resulting in the actual distance d_i' being proportional to the measured distance d_i as in

$$d_i' \propto d_i \tag{5.3}$$

To account for errors, d_i is referred to as *pseudo distance* in the following. For the closed environment, a circular cross-section is assumed. Many hollow organs exhibit a tubular shape, which justifies this as a first approximation. The four electrode distances $d_i', i \in \{00,01,02,03\}$ of one of the sensor rings determine the sensor's location in such an environment. To determine this location, the environment's coordinate system is defined with its origin at the circle's center and its axes aligned with the sensor axis. The geometric relations to derive the localization are depicted in Figure 5.9. Therefrom, the position $\boldsymbol{p}$ of the sensor in this environment is calculated as in

$$\boldsymbol{p} = \begin{bmatrix} p_x \\ p_y \end{bmatrix} = \frac{1}{2} \begin{bmatrix} d_{02}' - d_{00}' \\ d_{01}' - d_{03}' \end{bmatrix}. \tag{5.4}$$

The environment's radius can be calculated from the distances by

$$r_m' = \sqrt{(d_{00}' + p_x)^2 + p_y^2}. \tag{5.5}$$

Given the error-prone, sensed pseudo distances d_i, a resulting *pseudo radius*

$$r_m = \sqrt{d_{02}^2 + (d_{03} - d_{01})^2} \tag{5.6}$$

can be calculated. It is proportional to the actual radius r_m' ($r_m \propto r_m'$) and its proportionality factor is equal to the one from d_i to d_i'. Thus, a relative position $\boldsymbol{p}_n$ of the sensor inside the

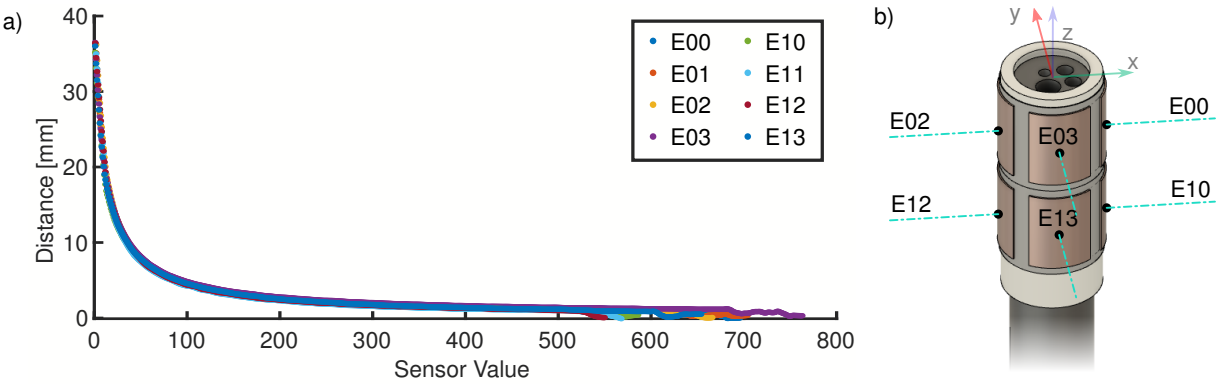

Figure 5.8 – a) Calibration curves for all eight electrodes of the proximity sensor. From characterization experiments, each sensor's raw value gets a distance assigned by a lookup table. The plot shows the mapping from sensor value to distance for each electrode. b) The positions of the electrodes on the sensor and the sensor coordinate frame. Adapted from [10].

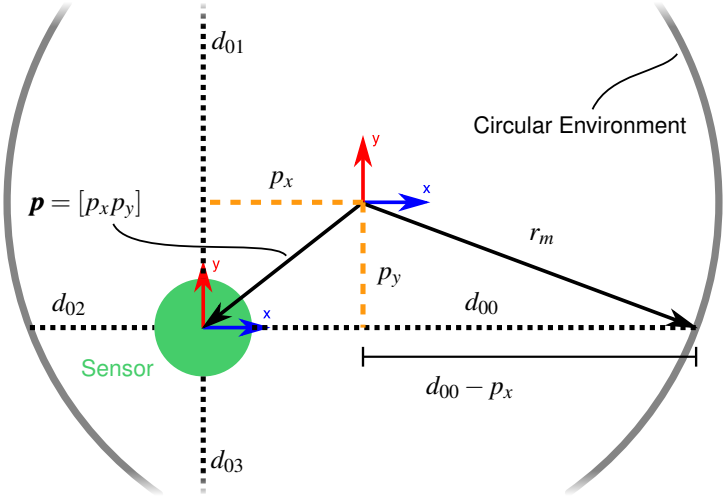

Figure 5.9 – Model for deriving the sensor location $\boldsymbol{p} = [p_x p_y]$ and the environment's radius r_m. From the three distances d_{00} to d_{03}, measured by the sensor, the relations in Equation 5.6 and 5.7 can be derived.

environment can be calculated by

$$\boldsymbol{p_n} = \begin{bmatrix} \frac{p_x}{r_m'} \\ \frac{p_y}{r_m'} \end{bmatrix} = \frac{1}{2} \begin{bmatrix} \frac{d_{02}-d_{00}}{r_m} \\ \frac{d_{03}-d_{01}}{r_m} \end{bmatrix}. \tag{5.7}$$

This position $\boldsymbol{p}_n$ can be calculated from the output of the sensor and allows to denote the sensor's relative position inside of the detected environment.

5.2.4 Sensor Evaluation

To evaluate the designed sensor and localization algorithm, a similar experimental setup as for calibration is utilized (see Figure 5.7). Instead of a plane phantom, a cylindrical phantom with an inner radius of $r_P = 25\,\text{mm}$ is used. Just like the calibration phantom, it is also 3D-printed, covered with an adhesive layer of copper on the inside, and grounded. The robot is used to move the sensor to known positions inside of the phantom and then compare the output of the localization algorithm to the reference from the robot.

To register the robot and sensor location to the phantom, an initial referencing motion is conducted before an experiment: The sensor is placed on the robot's TCP, inside of the phantom. Then, the robot drives from this initial position in each of its x- and y-axis' positive and negative directions until the FTS registers a contact. From these four coordinates of contact, the phantom's position in the robot's coordinate frame can be calculated. For the evaluation experiment, the robot is driven to 72 locations inside of the phantom: The phantom's inner space is sampled in polar coordinates, with the origin in the phantom's center. Angles from 45° to 360° are sampled in 45°-intervals, at radii from 10% to 90% radius at increments of 10%. At each location, the sensor samples the relative position from the sensor and the reference from the robot for evaluation.

To be able to compare these results to a more realistic scenario, the experiment is repeated with an ex vivo tissue phantom. For such a phantom, a layer of fresh poultry is added to the inside of the cylindrical copper phantom. This way the, reaction of the sensor to ex vivo tissue can be observed. The experiment is conducted in the same way as for the copper phantom: An initial referencing motion is conducted and then sensor values at 72 set points are sampled. For a statistical accuracy analysis, the experiments are repeated $n_C = 14$ times for the copper phantom and $n_{\mathrm{EX}} = 6$ for the ex vivo tissue phantom.

Figure 5.10 shows a plot of the reference points and the locations measured by the sensor for the copper phantom and the ex vivo tissue phantom. One exemplary experiment run is depicted for each phantom. The sample points (robot reference) are graphed as grey dots on a polar coordinate system and the measured locations are graphed as blue dots. Figure 5.11 shows the mean values and standard deviations of the distance from the phantom's center, measured by the sensor. This evaluation is presented for each of the major and minor axes over all n_C and n_{EX} runs. The numerical results for the accuracy statistics, including the maximum error E_m over all experiments of the analysis, are listed in Table 5.2.

To evaluate the localization accuracy in a more dynamic context, an additional experiment is conducted. In the same setup as in the previous evaluations, the localization data is continuously sampled at a rate of 10 Hz, during robot motion from the Stewart Platform. To cover the phantom's inner volume in a continuous motion, an Archimedean spiral pattern from r = 0 % to r = 80 % in 2.5 revolutions, is conducted with the robot. To evaluate localization quality during these experiments, the measured distance from the phantom's center is compared to the reference, given from the robot position. The average absolute error over the whole spiral trajectory is evaluated as a metric for accuracy. While the experiment in the ex vivo tissue phantom exhibits an average error of (9.8 ± 5.1) % with a maximum error of 22.0 %, the copper phantom's experiments showed an average error of (7.2 ± 3.2) % and 15.5 % maximum error. The traced locations, as well as the robot reference from both experiments, are plotted in Figure 5.12.

For qualitative evaluation closer to a medical use case and as a demonstration of sensor integration, a third experiment is conducted. The sensor is mounted on the tip of a flexible

Table 5.2 – Results of the experimental localization accuracy evaluation.

Values are provided as % radius		**45°-Axis**	**90°-Axis**	**135°-Axis**	**180°-Axis**	**total**
Phantom	E_C	-8.08	-5.51	-0.40	6.01	**-2.0**
n = 14	σ_C	1.45	1.27	1.52	1.46	**1.4**
	$E_{C,m}$	4.27	10.07	13.36	15.84	**15.84**
Ex Vivo	E_{EX}	-6.44	-0.76	2.96	0.70	**1.6**
n = 6	σ_{EX}	2.06	2.00	2.73	2.49	**2.3**
	$E_{\mathrm{EX,m}}$	3.79	12.26	14.80	18.95	**18.95**

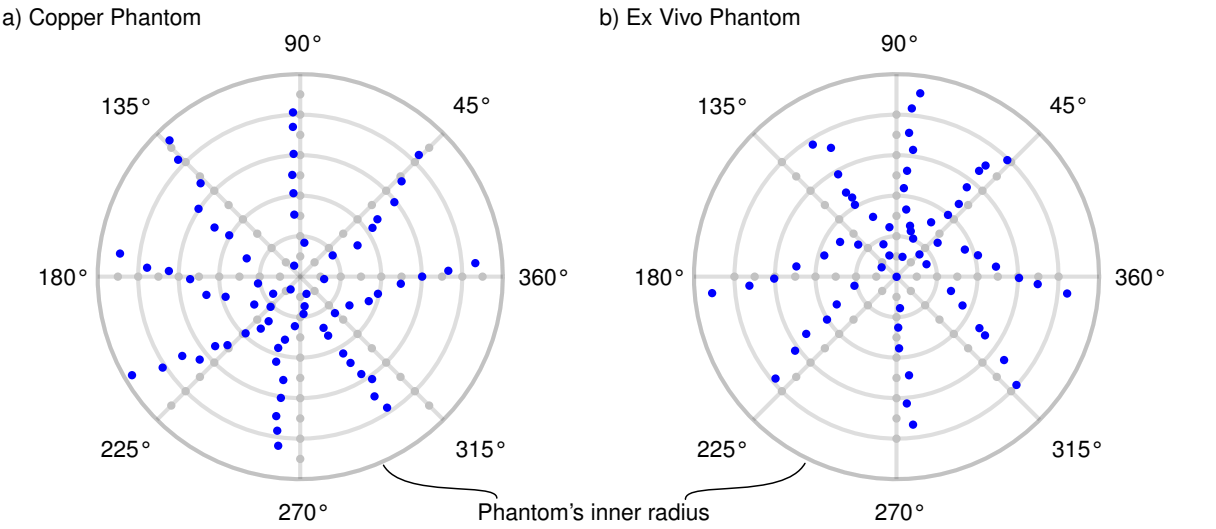

Figure 5.10 – Plot of an exemplary experiment run of the accuracy analysis. The gray dots denote the reference positions approached by the robot. The blue dots mark the measured position from the sensor. a) shows the copper phantom, b) the data for the ex vivo phantom [10].

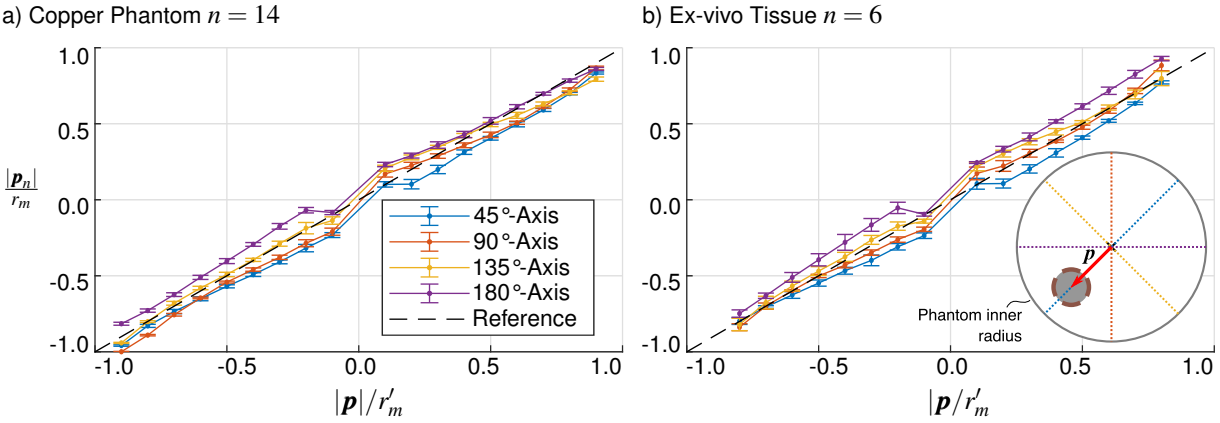

Figure 5.11 – Accuracy analysis for the proximity sensor. The sensed relative position $\frac{|\boldsymbol{p}_n|}{r_m}$ is compared to the real relative distance from the center $|\boldsymbol{p}|/r'_m$. The graph shows the mean values and standard deviations for all n runs for a) the copper phantom and b) the ex vivo phantom, separately for each of the phantom's four axes. As a reference, the dashed black line marks a hypothetical errorless sensor reading. The sketch in b) visualizes the axes and the analyzed metrics [10].

gastroscope and moved in proximity to a fresh piece of poultry tissue. As the sensor scaffold is fit to the endoscope's tip it can simply be placed on the endoscope's tip. The cables are guided along the endoscope's body. The sensor's raw values are observed while the endoscope is manually moved toward the tissue, using the gastroendoscope's handpiece. This motion is visualized in a series of photos in Figure 5.13. Simultaneously, the sensor's raw data is recorded. It is plotted in Figure 5.13c with the time points of the photographs marked. It can be seen, that the sensor values increase (i.e., due to the inverse proportionality to the distance) as the sensor approaches the tissue. Furthermore, it can be observed, that the electrode facing the tissue shows the highest amplitude compared to electrodes facing away from the tissue. This demonstration also supports the applicability of the sensor to standard-of-care instrumentation without further effort. Further affirmation is provided in the next section, transferring the sensing principle to a contact sensor and presenting an in vivo follow-up experiment.

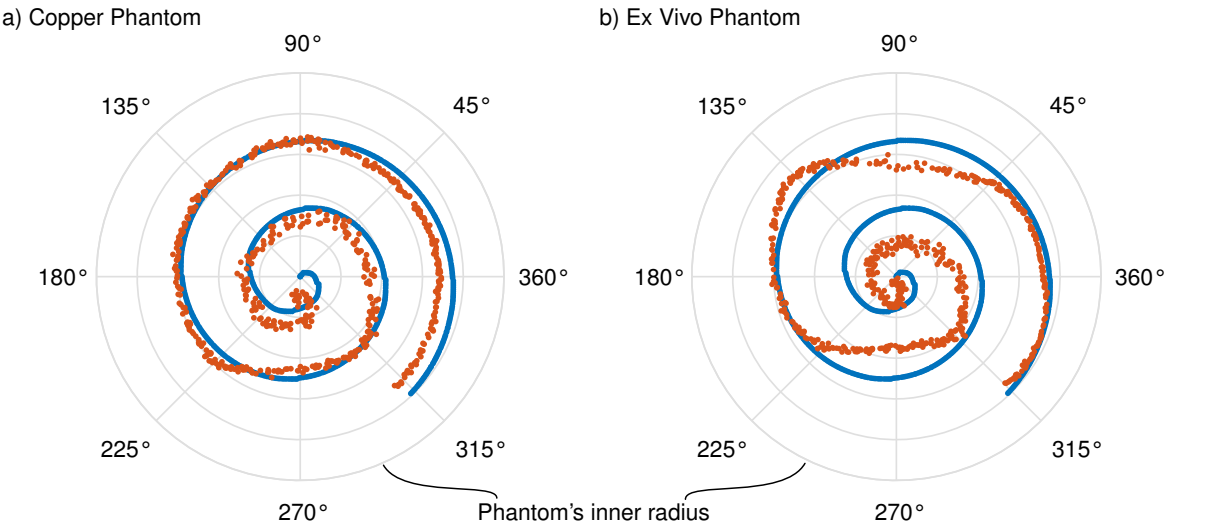

Figure 5.12 – Results of the dynamic evaluation. The blue dots mark the sensor position given from the robot. The red dots represent the measured location from the sensor. a) depicts the data from the copper phantom experiments, b) the data from ex vivo phantom experiments [10].

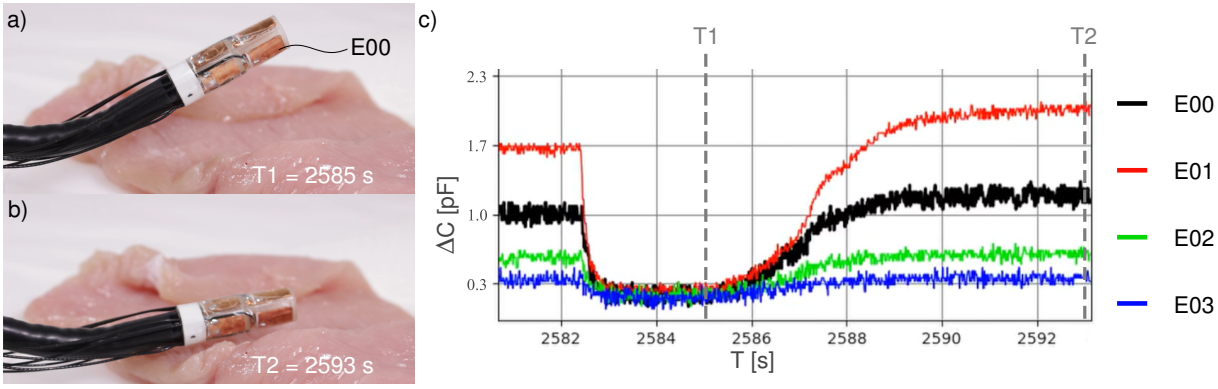

Figure 5.13 – Ex vivo experiment. a) and b) show two time points of the endoscope approaching the tissue. In c) the course of the capacitive proximity signal during the process is plotted. Adapted from [10]

5.3 Minimally Invasive Contact Sensing

In the following, the proximity sensor's principle is applied in an in vivo experiment. The sensing modality's versatility is demonstrated by applying the sensor to another type of minimally invasive robotic system, providing multi-touch information rather than proximity.

The robotic system in which the sensor is to be integrated is a development by the STORM lab at the University of Leeds, UK [36, 201]. The Magnetic Flexible Endoscope (MFE) consists of a 7-DOF serial robot arm with an actuating permanent magnet and localization circuit as an end-effector. This is used to control an invasive endoscopic capsule comprising magnetic sensing for proprioceptive localization, a camera, illumination, lens cleaning, insufflation, and a therapeutic channel. To allow for actuation, the capsule contains a smaller permanent magnet, which is manipulated by the external magnetic field. A localization circuit and algorithm allow for closed-loop control of the MFE. A soft tether connects the capsule to power, data, and water interfaces. To provide the system with information on contact to the situs at multiple locations, this section investigates the integration of capacitive sensing capabilities into the capsule robot.

In this experiment, the area of interest is the upper surface of the MFE's capsule. During colonoscopy sensing modalities for tissue diagnostics (e.g., ultrasound) could be integrated in

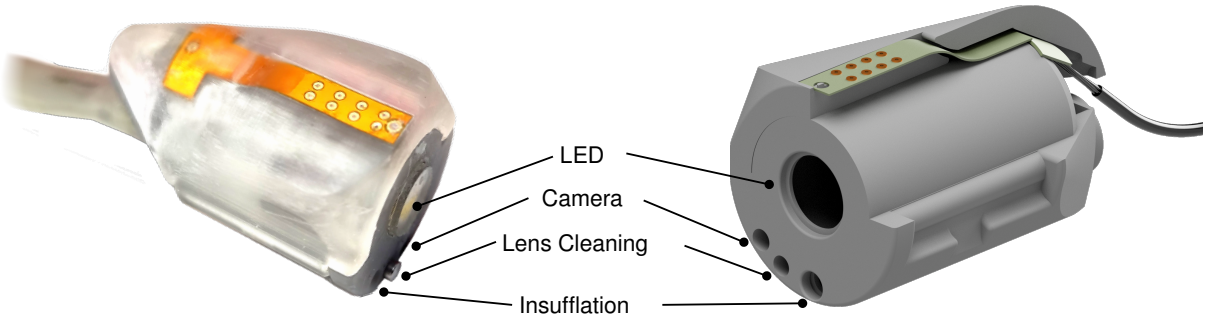

Figure 5.14 – The MFE's capsule with the integrated contact sensor. Left) The capsule with the integrated sensor. Right) Sensor integration and placement in the capsule scaffold.

such a location and provide information of the tissue, when in contact with the wall of the colon. On a surface of 4 mm by 26 mm, contact information should be provided. Due to the curved surface (see Figure 5.14), multi-point contact is of interest to derive information on the capsule's orientation in relation to the tissue in contact.

The sensor concept is based on the principle described in Section 5.2. The sensing unit is utilized in a similar manner. For this approach, the electrode's design is adapted to provide eight electrodes in the area of interest. From Equation 5.1 it can be seen that the sensor sensitivity, and therefore also its range, decreases with a smaller electrode size A. In the given case, small electrodes were insensitive to approaching tissue and a significant signal resulted only from direct contact. This allows the classification of such a signal, as contact and non-contact, for each of the sensor's electrodes.

Figure 5.14 shows a cut CAD model of the MFE's capsule, with the sensor integration visualized. The sensor is positioned at the top surface, as here contact information is of interest. To not rely on manual manufacturing, the electrode is designed and manufactured as a Printed Circuit Board (PCB). The sensing surface is split into eight contact sections, and based on the shape of the sensing area, a 2×4 pattern is chosen. Figure 5.15 shows the PCB's design and electrode arrangement. Each section integrates a circular electrode surface of 1 mm diameter, for capacitive sensing. To improve sensing accuracy, two sections are combined into one sensing pad. This way, the four quarters of the sensing area allow for the characterization of roll and yaw motion, when only three or fewer pads are in contact. Next to and below the circular sensing electrodes, layers of shielding electrodes are located to suppress signals not resulting from pad contact. To avoid short-circuiting in an in vivo humid environment, the PCB is sprayed with insulation spray. The sensor-PCB is then mounted in a notch at the top of the capsule so that its electrodes are flush with the capsule's surface. A mounting hole in the PCB helps to align and secure the sensor in the notch. The PCB comprises solder pads for the connection of cables to the sensor unit. The PCB's section with the solder pads is located in the capsules inside and the opening is sealed with glue. To connect the electrodes to the sensing unit, a shielded multi-core cable is used. As the individual channels of the sensing unit are sampled in series (see Section 5.2.2), channel cross-talk can be neglected. The common shield protects all channels from outer influences. Such a cable can be fed through the capsule's tether, which has a length of 2 m. Proximally, the channels are connected to the sensing unit, which is connected to a computer via USB.

In this experiment, the sensor was not calibrated beforehand. To classify contact and non-contact, the sensor values are analyzed after the experiment. To acquire contact information for the pads of the sensor, the capacitive sensor readings were processed as follows: The time series of the sensor readings $E_i(t)$ were normalized to a range from 0 to 1 for all eight electrodes. A

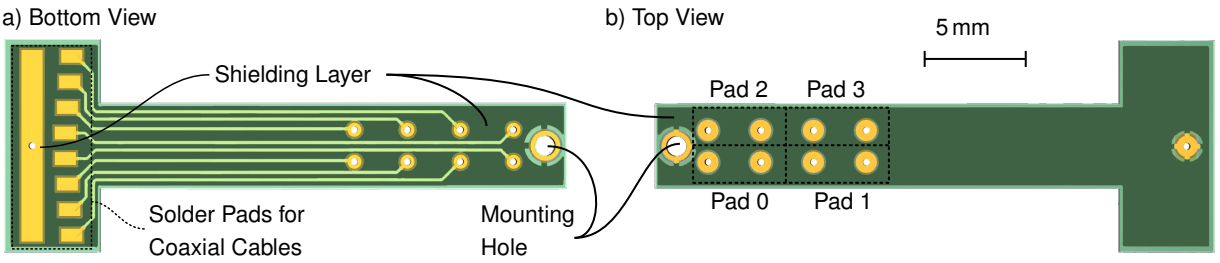

Figure 5.15 – Layout of the PCB for the sensing electrodes. a) Bottom view with solder pads and shielding layer b) Top view with contact sensing pads and groups.

contact threshold $\tau_i = M_i - 0.45\sigma_i$ was estimated from the median M_i and standard deviation σ_i from values $E_i(t)$ of electrode i. The contact value c_i for each electrode was calculated by

$$c_i(t) = E_i(t) - \tau_i. \tag{5.8}$$

To combine two electrodes into a pad, each electrode's contact value is weighted by a confidence a_i, before they are added to another. This a_i confidence is calculated by fitting a twofold Gaussian mixture model to the distribution of the sensor values. This results in two means μ_{i1} and μ_{i2} from the Gaussians for each electrode. As a confidence a_i, the distance of both means is then utilized as in

$$a_i = \mu_{i1} - \mu_{i2} \tag{5.9}$$

The contact value q_g for a pad (g) is then given by

$$q_g = a_{2g}c_{2g} + a_{2g+1}c_{2g+1}, \qquad g \in \{0,1,2,3\} \tag{5.10}$$

The sign of q_g determines the classification as contact (positive) or non-contact (negative).

The sensor is evaluated in an animal trial, conducted in Leeds, UK. The MFE was applied in a colonoscopy of an 34 kg female porcine model. The sensorized MFE setup was set up in a veterinary OR. The pig was sedated and enema was conducted. The MFE was inserted through the pig's rectum and an additional conventional colonoscope allowed observation of the capsule robot. The MFE's tracking data and the sensor's contact data were recorded while sweeping motions were conducted with the capsule. These trials were conducted under the home office (UK) license (procedure project license: PF5151DAF) in accordance with the animal (scientific procedures) act 1986 [11].

In Figure 5.16, the sensor information from the contact sensors is plotted over the time of motion. The data resulted from two sweeping motions along the colon's upper wall. Contact is indicated for each of the pads.

Further aim of the animal trial, was the restoration of the capsule's restoration of a Roll-DOF for better navigation and scanning motion in an endoscopic procedure. This research is submitted for publication at RAL [11].

5.4 Chapter Discussion

Chapter 5 demonstrates the utilization of capacitive measurements for proximity and multi-contact sensing, with application in endoscopic scenarios. A facile electrode implementation

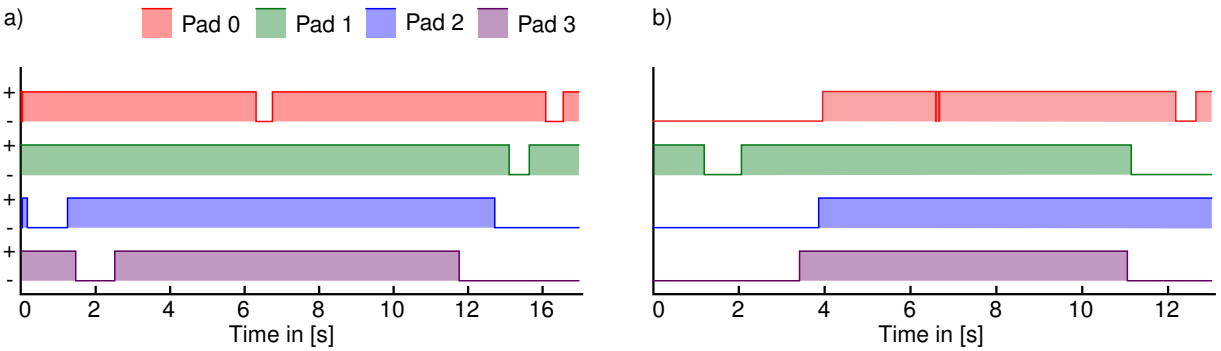

Figure 5.16 – Resulting time series from the in vivo experiments. Two exemplary motions are depicted respectively in a) and b). For each of the contact sensors, contact information is plotted. A positive signal correlates to the pad being in contact.

and versatile design allow for the application of such sensing in a proximity sensor for a gastroscopic device. By enabling relative localization, this can be crucial information in manual endoscopic interventions. In robot exteroception, such a sensing modality could offer high potential for automation in robotic endoscopy or general surgery. As a demonstration of the method's versatility, it was adapted to a multi-contact sensor for a magnetic capsule endoscope. The underlying technology is equivalent in both sensing modalities, yet through electrode design and processing, it can be applied to sense proximity or contact. In the following discussion, proximity (Section 5.4.1) and contact sensing (Section 5.4.2) are discussed separately, then a comparison of both methods is presented in Section 5.4.3.

5.4.1 Proximity Sensor

The accuracy results for the proximity sensor demonstrated, that even a complex trajectory could be recreated. In the copper phantom, the accuracy is higher than in the ex vivo phantom. This is expected as the ex vivo phantom exhibits a more inhomogeneous and non-ideal environment. The phantom's surface deviates stronger from a perfectly circular cross-section than the copper phantom's printed surface, and inhomogeneities in the tissue could affect local conductivity. Over the time of the experiments drying of the tissue was observed, presumably, increasing this effect.

The presented electrode fabrication method highlights the adaptability of the sensor to almost arbitrary geometries. The main consideration for a sensor design is the electrode area, being the main factor influencing the sensor's sensibility and range. The presented sensor manufacturing suffers from the manual fabrication process. Such a manufacturing process possibly introduces inaccuracies and differences in electrode sensibility. However, as the only requirement for a suitable electrode is a conductive layer, various manufacturing processes are applicable as future alternatives. As demonstrated for the contact sensor, a commercially manufactured PCB is a suitable option for future versions of such a proximity sensor. Conventional PCBs would restrict electrode geometry to a planar surface. The possibility of manufacturing flexible PCBs enables also equipping curved surfaces with sensor electrodes.

Even more flexibility could be achieved by 3D-printing electrodes from conductive filament or electroplating of 3D-printed structures. For the latter, preliminary studies for feasibility were conducted: A flexible SLA print was sprayed with graphite spray for priming and then immersed in a copper sulfate ($CuSO_4$) solution. The surface of the print is contacted by a cathode (negatively charged), the anode (positively charged) is immersed in the solution without further

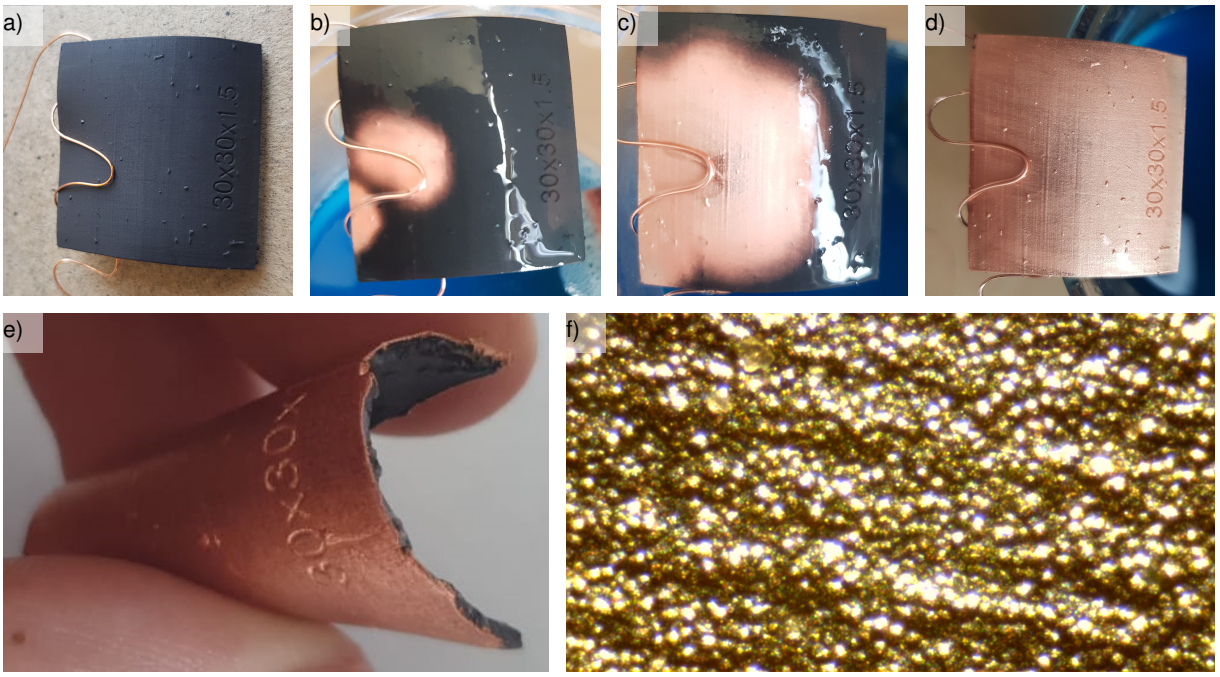

Figure 5.17 – The process of electroplating of a 3D-printed 30 mm × 30 mm electrode surface. a) The sample before plating, b) after 5 min, c) 15 min, and d) finished after 45 min. e) The sample maintains its elasticity. f) Shows a magnified image (40x) of the copper deposit.

contacting. A voltage of 0.6 V is applied for the copper to deposit on the print's surface. Figure 5.17 shows the progress of the electroplating process. After electroplating, the surface could be contacted and successfully used for proximity measurement. Such a method allows to convert any arbitrary (i.e., 3D-printable) surface into an electrode. A copper deposit also provides the beneficial characteristic of being well suited for soldering, i.e., the connection of cables. In the future, such a manufacturing method could enable full design freedom in electrode geometry and further improve the integration of capacitive proximity sensing into a robotic structure, even under tight spatial restrictions.

With the presented method for sensor calibration, differences in the electrodes from manufacturing can be balanced for the most part. It should be noted, however, that the presented calibration is lengthy, and for repetition, the robotic setup needs to be available. This conflicts with the observations of the sensor exhibiting drift over time and decalibration when the sensor is mounted or dismounted. These effects require a repetition of the calibration after several hours of operation. Future work should therefore investigate a facilitated calibration method that can be repeated in a facile manner and without requiring specialized equipment.

The four proximity values, provided by the sensor, not only allow for the estimation of a circular environment but could also approximate an elliptic environment. While such a calculation would result in the same estimation of the environment's center, it could provide additional feedback on the shape of the environment and pass it to a user or high-level controller, in a future version of the sensor.

In the proposed method, the localization algorithm only made use of four of the sensor's eight sensing elements. The data of the second sensor ring could be used to improve the sensing range while maintaining the presented sensing method. To achieve this, the sensor module allows to combine multiple channels and use them as a single electrode with the combined electrode area. An alternative benefit would be to utilize the second set of sensor electrodes for an estimation of the sensor's tilt. When the sensor is tilted in relation to a tubular environment,

the localization of both rings results in a localization offset in both rings. From this offset, the sensor's tilt can be estimated. Such a tilt measurement could serve as additional information for navigation and input autonomous camera alignment.

The demonstrated capabilities of the sensor are suitable for integration into a robotic system. The localization feedback can be utilized for closed-loop control, which allows to center the sensor in a minimally invasive environment. A method for such a controller and the demonstration in a continuum robotic system is presented in Chapter 6.

5.4.2 Contact Sensor

The integration of capacitive sensing into the presented capsule endoscope demonstrated the sensor's versatility. The sensor principle was successfully transferred to a flexible PCB design, and made integration possible in a system with even more stringent spatial constraints, as in the proximity sensor. The sensor setup could also address another issue of practical relevance: For the animal trials, it was necessary to connect the electrode to the sensing unit via cables of more than 2 m length. As part of the design process, the connection of the electrodes to the sensing unit with single-core coaxial cables and a commonly shielded multi-core cable were compared. In these evaluations, no major deviation in the signal quality was found. Furthermore, it could be shown, that an increased overall length of either cable hardly affects the sensor readings (comparing the proximity sensor's 30 cm length to the capsule robot's 200 cm length). For future designs, this finding allows for more freedom in the sensor design regarding the method for cabling the sensor. Additionally, it proves applicability to systems which require a long distance from the location of in situ sensing to an instrument's or robot's proximal end.

While the presented contact sensor could still work as a proximity sensor, it showed, that due to the size reduction of the electrodes, the range was limited substantially. Through the processing, the capacitive signal was solely utilized for the characterization of contact. This did not require any preceding calibration, due to the data-driven characterization of the data. However, this method was only demonstrated for a retrospective analysis of the sensor data. Future work should investigate the application of this method for an online characterization. The recorded history of the data could be used to classify new raw data online and combine an ongoing calibration and an online classification.

5.4.3 Comparison

The proximity sensor could demonstrate the data processing for online processing, suitable for integration into a closed-loop controlled system. However, its calibration method is cumbersome and might result in challenges like sensor drift. While the contact sensor's processing was unsuitable for the delivery of online values, it demonstrated the feasibility of a calibration-free classification. Even though it is in a rudimentary state, it could serve as a starting point for future work, combining the online processing of the raw data with an online calibration, based on the sensor data history.

Regarding manufacturing, the manual proof of concept for the proximity sensor's electrode manufacturing could be developed further by the implementation as a PCB. Together with the preliminary study on electroplated 3D prints and further manufacturing methods in research such as 3D printing and stretchable electrodes, a variety of methods can be chosen from [202].

The facile and space-saving integration makes capacitive sensing a well-suited candidate for continuum robots. Future improvements should look into online calibration methods to counteract drift and the sensing modality's susceptibility to various changes in the environment. Furthermore, the sensor can be further developed to incorporate not only proximity or contact sensing but also combine proximity and tactility, taking the force of a contact into account. Fundamentals of a suitable electrode architecture have been presented in [166] and could be investigated for adoption in minimally invasive instruments and robots. Such a development could result in a useful sensing technology for manual and autonomous endoscopy or MIS, as in many scenarios, contact does not necessarily need to be prevented, but rather contact needs to be limited.

6 Proximity Controlled Continuum Robot

Chapter 4 and Chapter 5 presented a robot platform and a proximity sensor, respectively. As advertised in the respective discussions, and as a logical consequence, the combination of both methods is now presented and evaluated. Next to the physical integration of the robot and the sensor, a kinematic model and a controller are presented, which allow for proximity control of the developed CR. The implementations required for this integration were considerably supported by Maximilian Themistocli in his work as a student assistant. The accomplished methods and results are submitted for publication at IEEE - Transaction on Medical Robotics and Bionics (TMRB) [12].

Table 6.1 – Overview of symbols used in this chapter. When applicable, symbols from Chapter 4 and Chapter 5 where taken over.

Symbol	Parameter	Symbol	Parameter
$D = [d_1, d_2]^T$	Tendon shortenings	$S_h(E_h)$	Calibration Function
$\boldsymbol{q} = [\theta_x, \theta_y]^T$	Actuator space	$\boldsymbol{p}_C$	Goal in TCP frame
α, β, γ	Task Space Angles	$\boldsymbol{p}_B$	Goal in base frame
t_x, t_y, t_z	Task Space Translations	$\boldsymbol{p}_0$	TCP position in base frame
T_{CR}	Transformation Matrix CR	n	Controller Iteration
$\rho = \sqrt{\theta_x^2 + \theta_y^2}$	Substitution to improve display	m	Video Frames
$\boldsymbol{p}_{\text{TCP}}$	CR TCP position	k	Current Frames
$h \in \{X+, Y+, X-, Y-\}$	Sensor channels	q_{acc}	Quality Mean Distance
$s_{X+}, s_{Y+}, s_{X-}, s_{Y-}$	Sensor distances	q_{wall}	Quality Percentage on wall
$\varepsilon A_h, C_{0,h}$	Calibration parameters		

6.1 Introduction

In typical interventions with flexible endoscopes, the surgeon screens the endoscope's image for potentially malignant nodules, lesions, or polyps. In this process, a complex instrument control can be a distraction and expose the surgeon to additional cognitive as well as physiological stress [7]. The introduction of robotic systems in MIS is well suited to address the aspect of ergonomics and can provide intuitive surgeon's consoles for control, tailored to an ergonomic posture. As such systems are mostly teleoperated, they still challenge the surgeon regarding the control of the available DOFs. Thus a highly actuated flexible robotic system, such as needed for endoscopic interventions, would still result in a high cognitive load for control. To address this issue, a flexible robotic instrument's control can be enhanced by autonomous functions. Aiming to reduce the number of control inputs, this could support the surgeon in navigation and manipulation during an intervention. Such supportive functions are rarely implemented as of now. Therefore, this chapter introduces a self-centering capability in a minimally invasive continuum robot, based on capacitive proximity sensing. With the robot presented in Chapter 4 and the sensor introduced in Chapter 5, methods are presented that integrate both in one setup. To control this system, a suitable control algorithm is developed and implemented. Similar

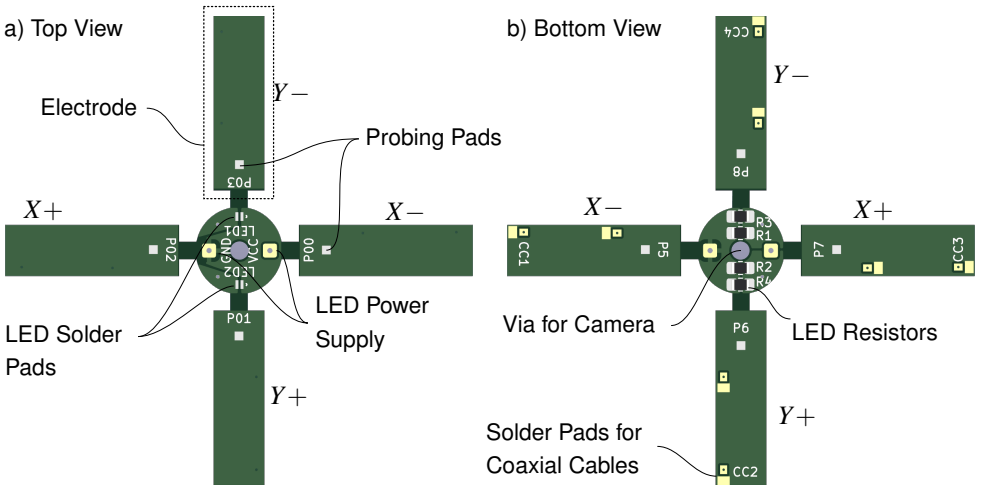

Figure 6.1 – Layout data of the end-effector PCB. a) Top view with pads for LEDs and front of electrodes. b) Bottom view with pads for LED resistors. The PCB integrates capacitive electrodes, illumination, and camera mount.

methods for control based on spatial sensing have been demonstrated, based on an endoscope's image [55–58]. Utilizing an endoscope's camera, however, only allows for the acquisition of spatial information in the front-facing field of view. Lateral obstructions can only be considered from intraoperative maps. However, in soft tissue interventions, such maps are often rendered invalid very fast as the tissue is moving. To gain lateral spatial information, fiber-based optical distance sensors have been applied for closed-loop control of a continuum robot [132, 133]. Such sensors are strongly reliant on the varying reflectivity of the tissue to be sensed. To overcome such issues, the method presented in the following applies capacitive proximity sensing for control.

6.2 Sensorized Continuum Robot

The sensor, developed in Chapter 5, has been designed as an add-on sensor for a commercial endoscope. Integration into a continuum robotic device should comprise more than the sensor just being attached to the robot's top. The aim of this chapter is to design a complete robotic system, that comes close to providing the functional features, expected from an endoscopic device. Therefore, the robot's tip, from chapter 4 is redesigned into a multi-functional end-effector, providing vision, illumination, and proximity sensing.

Sensorized Tip As discussed in Section 5.4.1, the sensor's electrode manufacturing depends on manual precision during assembly. To reduce this dependence, the sensor electrodes are integrated into a manufactured PCB. This allows for better repeatability of sensor manufacturing and more efficient use of space. The shielding and sensing electrodes can be realized as a two-layer PCB. Solder pads on the inner layer are designed to fit the employed coaxial cables, a via connects the cable's inner conductor to the outer sensing electrode. To maximize the sensor range, the sensor area is increased in a trade-off for the second ring of electrodes. In this thesis, proximity control is presented without the use of tilt information of the sensor. Thus, the sensor comprises only four electrodes with an area of 7 mm × 20 mm. Figure 6.1 shows the sensor-PCB layout. The PCB is manufactured on a flexible substrate. This allows to manufacture the 3-dimensional tip assembly as a single PCB. The center of the PCB contains footprints on

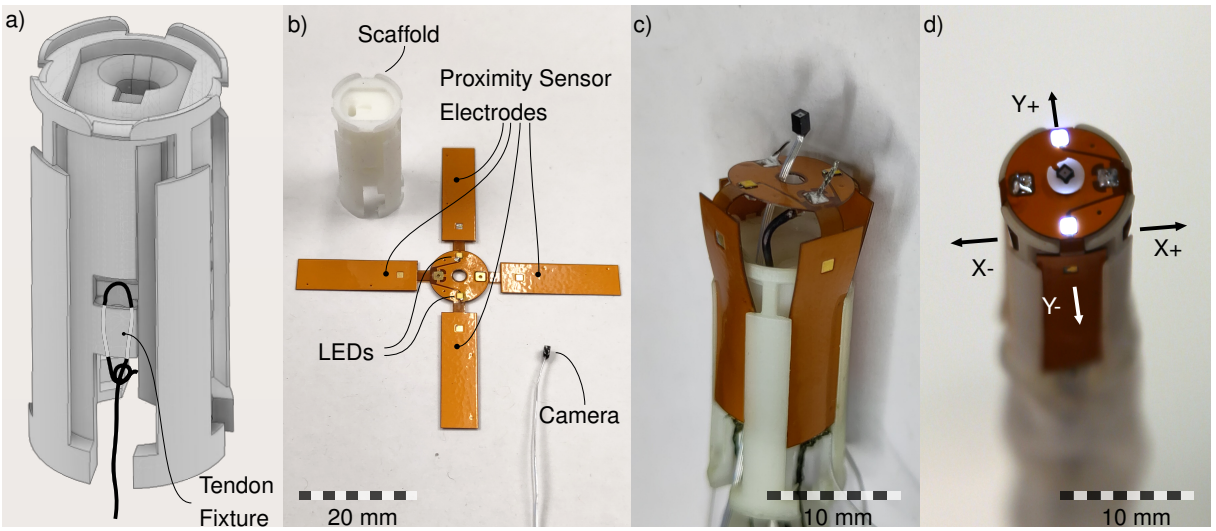

Figure 6.2 – a) The end-spacer design (CAD) with camera cable guidance and tendon fixture. b) The separate components before assembly. c) Intermediate assembly process with electrodes be pushed in the mount. d) The finished sensorized head of the CR. Adapted from [12].

its top, for two high-power white LEDs (GW VJLPE1.EM, Osram, Germany) with a size of 1.08 mm $\times$ 1.08 mm. The backside integrates four 2012 (metric) footprints for SMD resistors to limit LED-current. A central via of 2 mm diameter allows a miniature camera to be placed in the PCB.

The sensor electrodes are connected to the sensing unit with coaxial cables (Coaxial Cable 9442 WH033, Alphawire, USA) with 0.3 mm diameter. These small-diameter cables were chosen to minimize the effect of the cable stiffness on the robot's motion. The LEDs circuit is connected to the power supply via flexible silicone cables. In the central via of the PCB, a miniature camera (NanEye 2D, AMS, Premstaetten, Austria) is mounted, using a 3D-printed adapter.

To hold the sensor PCB in place, the robot's end-spacer was redesigned to comprise a scaffold for the end-effector electronics. A notch in its bottom center allows it to be placed on the backbone. The backbone ends on the z-position of the center of the electrodes. Further features allow the fixture of each of the four Segment II tendons. For PCB assembly, the four electrodes are folded downward and slid into tailored mounts in the scaffold. This assembly process is shown in Figure 6.2. When set in place, an electrode's normal point in each of the x- and y-directions. Therefore, in the following, the electrodes are referred to by $X+, Y+, X-$, and $Y-$ (see Figure 6.2d). A central channel in the scaffold guides the LED power wires and camera wire from the PCB through the end-spacer. The coaxial cables are attached to the electrodes on their inward-facing surface and can be guided directly to the spacer disks.

To incorporate the cables for the new end-spacer, the robot's spacer disks were fitted with additional holes to guide coaxial and power cables. A T-shaped notch was included to accommodate the camera cable. This allows for the dismounting of the camera without disassembling the robot. The revised spacer layout is depicted in Figure 6.3. The robot base now includes a channel to guide the camera, power, and coaxial cables directly through the base to the substruction. To provide protection and demonstrate the possibility of sealing the robot, a 3D-printed cover was fitted over the base and load cell units. The robot's body is protected by a silicone drape. It was manufactured by molding silicone (EcoFlex 0030, KauPo Plankenhorn e.K., Spaichingen, Germany) onto a 8 mm aluminum rod. For curing it was held upright for excess

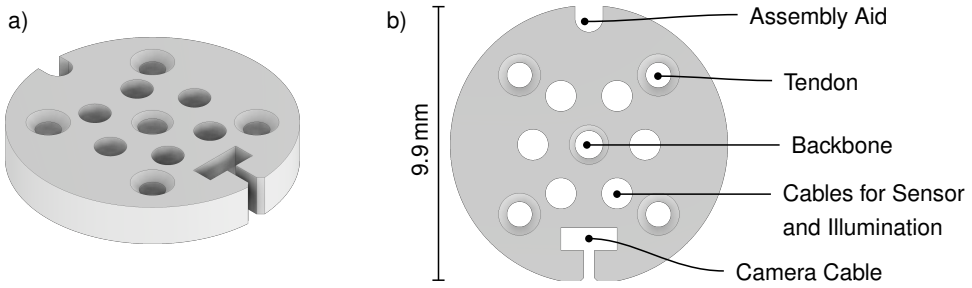

Figure 6.3 – The revised spacer design for the sensorized robot in a 3D view a) and an annotated top view b). Besides the holes for the backbone and the tendons, the spacers comprise channels for the cables of the sensor and the illumination at the robot's tip. For the camera's flat ribbon cable, a T-shaped notch allows the dismounting of the camera without the disassembly of the robot.

Table 6.2 – Serial commands for controlling the CR with their parameters P1 and P2.

CMD	P 1	P 2	Function
`s`	`[0,1,2,3]`	`[0 - 180]`	Set motor P1 to position P2 [1]
`f`	`[0,1]`	-	Enable (P1 = 1) or disable (P1 = 2) the robot servos
`l`	`[0-255]`	-	Set end-effector illumination to power level P1
`m`	`[0,1,2,3]`	-	Get the current motor position of motor P1

silicone to flow off and form a thin layer. The process was repeated three times to gain a thin (< 1 mm) but resistant silicone layer. For demolding, magnesium carbonate is used to reduce the silicone's adhesiveness. Figure 6.4 shows the fully set up robot including cover and drape.

Adaptions to the Robot Body and Base The coaxial cables for the sensing unit are fed through a central hole of the substruction's bottom plate and can be connected to the sensing unit as shown in Figure 5.5. In this case, only the first four channels ($i = 00$ to $i = 03$) are used. To power and control the LEDs for camera illumination, the Arduino shield of the robot is adapted: The LEDs are driven with a current of approximately 50 mA. PWM of the current allows to dim the LED's intensity. As the Arduino cannot directly provide such a high current, the amplifier circuit, depicted in Figure 6.5 is implemented on the Arduino shield. The figure also shows the assembled shield. The end-effector camera is read out by the NanoUSB2 Eval Kit (AMS, Premstaetten, Austria), which provides the images over USB to a PC. The image has a resolution of 250×250 pixels, the image quality strongly depends on the illumination of the scene. As a preliminary experiment, the integrated camera was tested in a phantom to evaluate the image quality and suitability of the illumination. The robot's tip was placed inside the inferior vena cava of a plastic heart model, facing the right atrium (see Figure 6.6a). The model was closed to test the illumination of the robot's tip (Figure 6.6b). For a sufficient illumination of the scene, at approximately 10 mm distance, an intensity value of 25 (i.e., 9.8 %) of the LEDs was required. The resulting image of the atrium is shown in Figure 6.6c.

Robot Firmware The control of the robot system is implemented in the latest ROS version, which was `foxy` at the time of development. For this version, the `rosserial` package, used in Section 4.3, is not available anymore. Furthermore, data transmission between the µC and a PC through ROS-topics results in an unnecessary overhead for this peer-to-peer use case. Therefore, a custom serial interface is implemented with control commands as listed in Table 6.2. It

[1] The range of 0 - 180 is mapped to the servo's available range. i.e., 0° - 270° in the presented case.

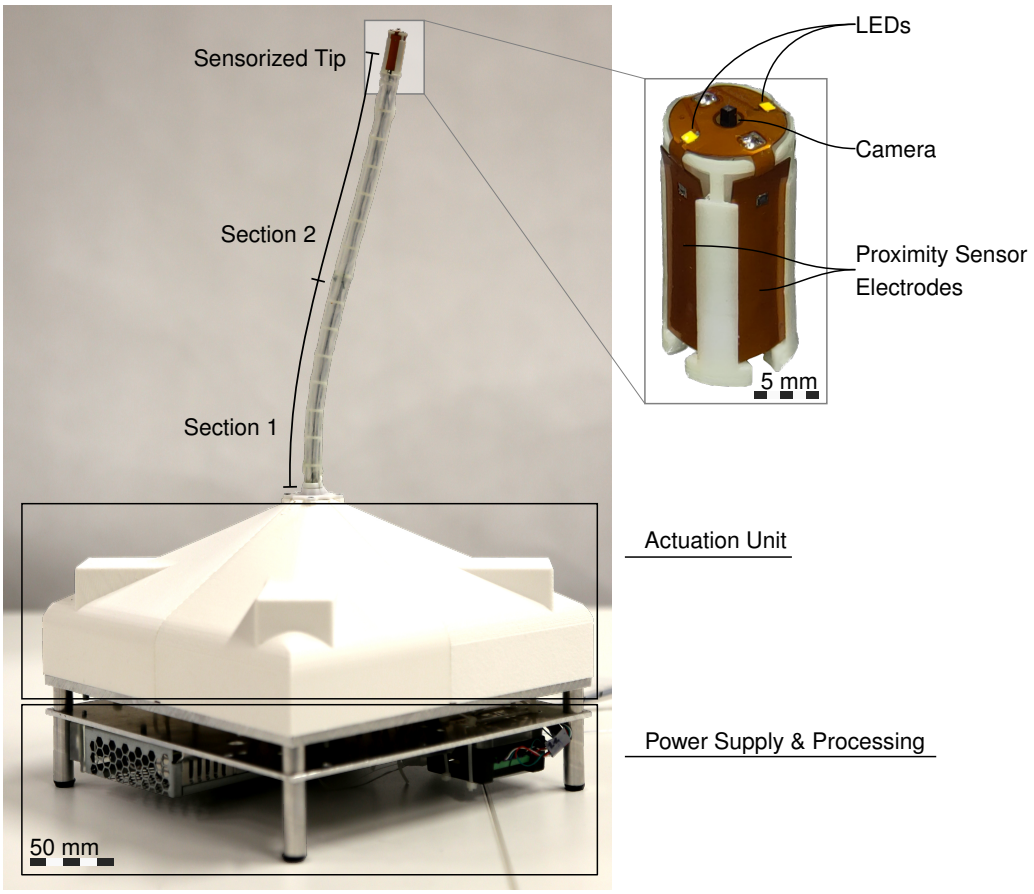

Figure 6.4 – The continuum robotic platform with the capacitive proximity sensor, camera, and illumination integrated into the robot's tip. Adapted from [12].

operates at a rate of 57600 Bd and allows to set each motor's position, set the LED's brightness, and query a motor's current position. Furthermore, it provides functionality to enable and disable the robot. In its disabled state the robot does not accept new position commands, the current state is shown by the robot's signaling LEDs.

6.3 Proximity Control

A demonstrator of the sensorized continuum robotic system is further evaluated for proximity control in an endoscopic scenario. As discussed in Chapter 2 such a controller could form a useful extended functionality for robotic endoscopic devices to support surgeons with an optimal view for navigation, less cognitive load for endoscope control, and a lower risk of injury. The following section describes the derivation of a kinematic robot model and the utilization of localization information from the sensor. Both are then combined in a control algorithm that aims to center the robot TCP in a hollow organ. Unless explicitly noted, the definitions of the symbols from Chapter 4 and Chapter 5 are applied here, respectively.

6.3.1 Kinematic Model

The robot is modeled as a single-segment robot, whose backbone takes the shape of a constant curve. To augment the presented, two segment robot to such a model, the Segment II servo

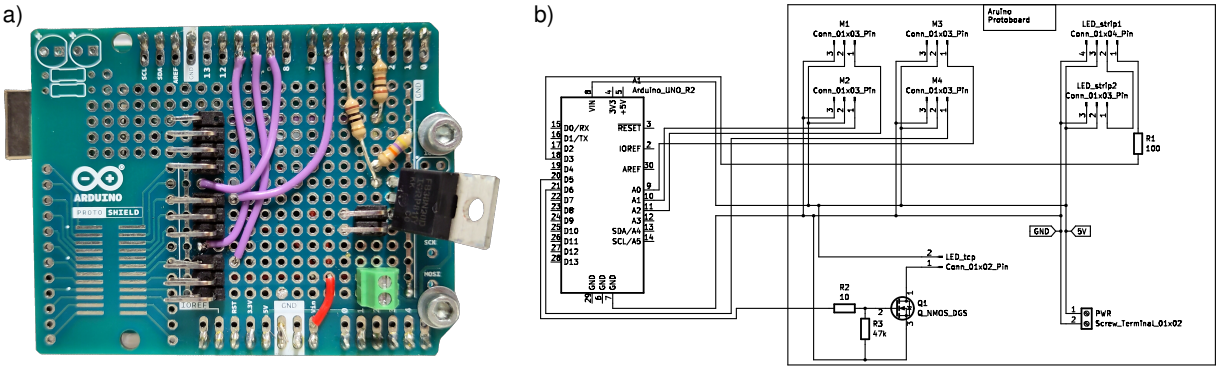

Figure 6.5 – a) Photo and b) circuit diagram of the Arduino shield. It provides the amplifier circuit for the end-effector's LED control and connectors for the motors and signaling LEDs.

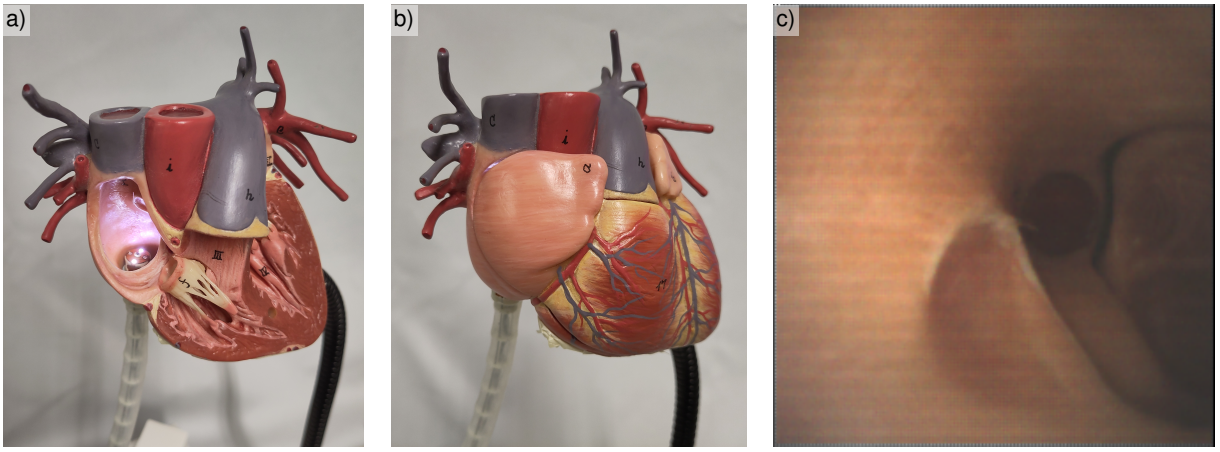

Figure 6.6 – Preliminary evaluation of the integrated image sensor. a) The robot's tip is placed in a plastic heart model. b) The closed model with the robot inserted. c) An image of the right atrium from inside the closed model, taken by the robot's image sensor using the integrated illumination.

positions θ_{X2} and θ_{Y2} are controlled in dependence of the Segment I servo positions θ_{X1} and θ_{Y1} by the following control rules:

$$\theta_{X1} = \frac{1}{2}\theta_{X2} \qquad \text{and} \qquad \theta_{Y1} = \frac{1}{2}\theta_{Y2}. \tag{6.1}$$

This ensures, that $T_{(x+)1}$, $T_{(x-)1}$, $T_{(y+)1}$ and $T_{(y-)1}$ follow the backbone shape determined by $T_{(x+)2}$, $T_{(x-)2}$, $T_{(y+)2}$ and $T_{(y-)2}$ and do not apply an interfering force.

To set up the robot model and the forward and inverse kinematics, the following spaces are defined corresponding to Section 3.1.4:

- **Actuator Space** $\mathbb{Q}$**:** It comprises the motor positions $\theta_x = \theta_{X2}$ and $\theta_y = \theta_{Y2}$. Due to the control rule in Equation 6.1, θ_{X1} and θ_{Y1} are not defined as part of the actuator space.
- **Configuration Space** $\mathbb{C}$**:** It comprises parameters describing the constant curvature robot configuration: κ as the constant curvature and the direction of deflection as angle ϕ from the positive x-axis.
- **Task Space** $\mathbb{T}$**:** It comprises a homogeneous 3D transformation T_{CR} defining the TCP coordinate frame in the robot's base coordinate frame

The kinematic concept and the robot's parameters are visualized in Figure 6.7. The robot is assumed to form a constant curve κ in the direction of ϕ. The tendon displacements d_1, d_2

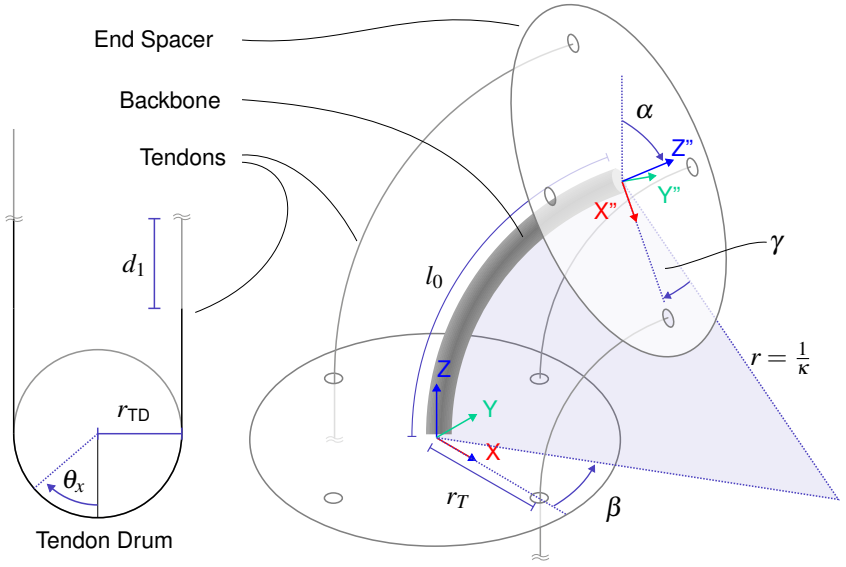

Figure 6.7 – Visualization of the kinematic model applied. A tendon displacement d_1 causes the backbone to bend in the bending direction determined by β. In doing so, the backbone assumes a constant curvature arc with a radius r. The robot's forward kinematic maps the tendon drum rotations θ_x (and θ_y, not shown here) to a homogeneous transformation from the robot's base coordinate frame XYZ to the TCP frame X"Y"Z". [12]

resulting from tendon drum rotation (see Equation 4.1) are given by

$$d_1 = \theta_X r_{\text{TD}} \qquad \text{and} \qquad d_2 = \theta_Y r_{\text{TD}}. \tag{6.2}$$

The robot's TCP coordinate frame can be described by three translations from the robot's base coordinate frame t_x, t_y, t_z, and three rotations $R_Z(\beta)R_Y(\alpha)R_{Z''}(\gamma)$ (i.e., a global rotation of α around the global y-axis, a rotation of β around the global z-axis, and a rotation of γ around the local z-axis). From the geometric relation (see Figure 6.7) it can be derived, that $\gamma = -\beta$. Then, this transformation can be expressed as a homogeneous transformation matrix T_{CR} as in

$$T_{\text{CR}} = \begin{bmatrix} \cos^2\beta\cos\phi + \sin^2\beta & \cos\beta\cos\phi\sin\beta - \sin\beta\cos\beta & \sin\phi\cos\beta & t_x \\ \cos\phi\sin\beta\cos\beta - \sin\beta\cos\beta & \cos\phi\sin^2\beta + \cos^2\beta & \sin\phi\sin\beta & t_y \\ -\sin\phi\cos\beta & -\sin\phi\sin\beta & \cos\phi & t_z \\ 0 & 0 & 0 & 1 \end{bmatrix} \tag{6.3}$$

For a mapping $\mathbb{C} \mapsto \mathbb{T}$, the following relations can be geometrically derived:

$$\alpha = \frac{\kappa}{l_0} \qquad \beta = \phi \tag{6.4}$$

$$t_x = (1-\cos(\kappa l_0))\frac{1}{\kappa}\cos\beta \qquad t_y = (1-\cos(\kappa l_0))\frac{1}{\kappa}\sin\beta \qquad t_z = \sin(\kappa l_0)\frac{1}{\kappa} \tag{6.5}$$

T_{CR} from Equation 6.3 can now be expressed as a mapping from actuator to task space $\mathbb{Q} \mapsto \mathbb{T}$. Therefore, the following relations of the configuration space parameters κ, β are applied:

$$\kappa = \frac{\sqrt{d_2^2 + d_1^2}}{l_0 r_T} \qquad \beta = \arctan\frac{d_2}{d_1} \tag{6.6}$$

Equations 6.6 in combination with Equation 6.2 allows to express Equation 6.3 as forward kinematic, projecting an actuator space position $\boldsymbol{q} = [\theta_x, \theta_y]^T$ to task space:

$$T_{\mathrm{CR}}(\boldsymbol{q}) = \begin{bmatrix} \cos(\frac{r_{\mathrm{TD}}\rho}{r_T})\frac{\theta_x^2}{\rho^2} + \frac{\theta_y^2}{\rho^2} & \cos(\frac{r_{\mathrm{TD}}\rho}{r_T})\frac{\theta_x\theta_y}{\rho^2} - \frac{\theta_y\theta_x}{\rho^2} & \sin(\frac{r_{\mathrm{TD}}\rho}{r_T})\frac{\theta_x}{\rho} & (1-\cos(\frac{r_{\mathrm{TD}}\rho}{r_T}))\frac{l_0 r_T \theta_x}{r_{\mathrm{TD}}\rho^2} \\ \cos(\frac{r_{\mathrm{TD}}\rho}{r_T})\frac{\theta_y\theta_x}{\rho^2} - \frac{\theta_y\theta_x}{\rho^2} & \cos(\frac{r_{\mathrm{TD}}\rho}{r_T})\frac{\theta_y^2}{\rho^2} + \frac{\theta_x^2}{\rho^2} & \sin(\frac{r_{\mathrm{TD}}\rho}{r_T})\frac{\theta_y}{\rho} & (1-\cos(\frac{r_{\mathrm{TD}}\rho}{r_T}))\frac{l_0 r_T \theta_y}{r_{\mathrm{TD}}\rho^2} \\ -\sin(\frac{r_{\mathrm{TD}}\rho}{r_T})\frac{\theta_x}{\rho} & -\sin(\frac{r_{\mathrm{TD}}\rho}{r_T})\frac{\theta_y}{\rho} & \cos(\frac{r_{\mathrm{TD}}\rho}{r_T}) & \sin(\frac{r_{\mathrm{TD}}\rho}{r_T})\frac{l_0 r_T}{r_{\mathrm{TD}}\rho} \\ 0 & 0 & 0 & 1 \end{bmatrix} \tag{6.7}$$

Here ρ is calculated as

$$\rho = \sqrt{\theta_x^2 + \theta_y^2}. \tag{6.8}$$

From T_{CR}'s fourth column, the TCP's position $\boldsymbol{p}_{\mathrm{TCP}}$ is derived by

$$\begin{bmatrix} \boldsymbol{p}_{\mathrm{TCP}}(\boldsymbol{q}) \\ 1 \end{bmatrix} = \begin{bmatrix} (1-\cos(\frac{r_{\mathrm{TD}}\rho}{r_T}))\frac{l_0 r_T \theta_x}{r_{\mathrm{TD}}\rho^2} \\ (1-\cos(\frac{r_{\mathrm{TD}}\rho}{r_T}))\frac{l_0 r_T \theta_y}{r_{\mathrm{TD}}\rho^2} \\ \sin(\frac{r_{\mathrm{TD}}\rho}{r_T})\frac{l_0 r_T}{r_{\mathrm{TD}}\rho} \\ 1 \end{bmatrix} \tag{6.9}$$

As Equation 6.9 is undefined for $\theta_x = \theta_y = 0$, this singularity is counteracted by defining

$$\boldsymbol{p}_{\mathrm{TCP}}\left(\begin{bmatrix} 0 \\ 0 \end{bmatrix}\right) = \begin{bmatrix} 0 \\ 0 \\ l_0 \end{bmatrix}. \tag{6.10}$$

6.3.2 Sensor Data Processing

The sensor data is processed similarly to the method presented in Section 5.2. The four electrodes $h \in \{X+, Y+, X-, Y-\}$ are used to provide a new goal state for the CR's TCP position. The work presented in Chapter 5 showed, that the sensor values are prone to a shift (constant over all electrodes) over time, likely due to environmental changes. Thus, calibration is required to be repeated for the sensor to work reliably. Conducting the calibration based on a sensor characterization, as presented in Section 5.2.2 is costly in terms of time and equipment required and unsuitable for repeated calibration, especially with regard to an application in the clinic. Therefore, a simplified calibration method, suitable for sensor calibration on the CR is required. As suggested by Equation 5.1 and supported by the data presented in Figure 5.8, the mapping of the sensor's raw value E_h to the sensor distance s_h is reciprocal. Thus, a calibration function $S_h : E_h \mapsto s_h$ is needed for each electrode h fitting the model function

$$s_h = \frac{\varepsilon A_h}{E_h - C_{0,h}}. \tag{6.11}$$

As this model is used as an approximation of the physical setup, εA_h and $C_{0,h}$ purely represent calibration parameters with no direct physical representation in the sensor setup. C_0 can be determined at a clearance measurement where $s_h \to \infty$ can be assumed, and $C_{0,h} = E_h$ can be set. Despite $C_{0,h}$ being set at a clearance measurement, noise can result in values of $E_h > C_{0,h}$. As a result, the denominator in Equation 6.11 could assume small negative numbers and result in $s_h \ll 0$. This does not correspond to a representation in the physical setup. To prevent this, an

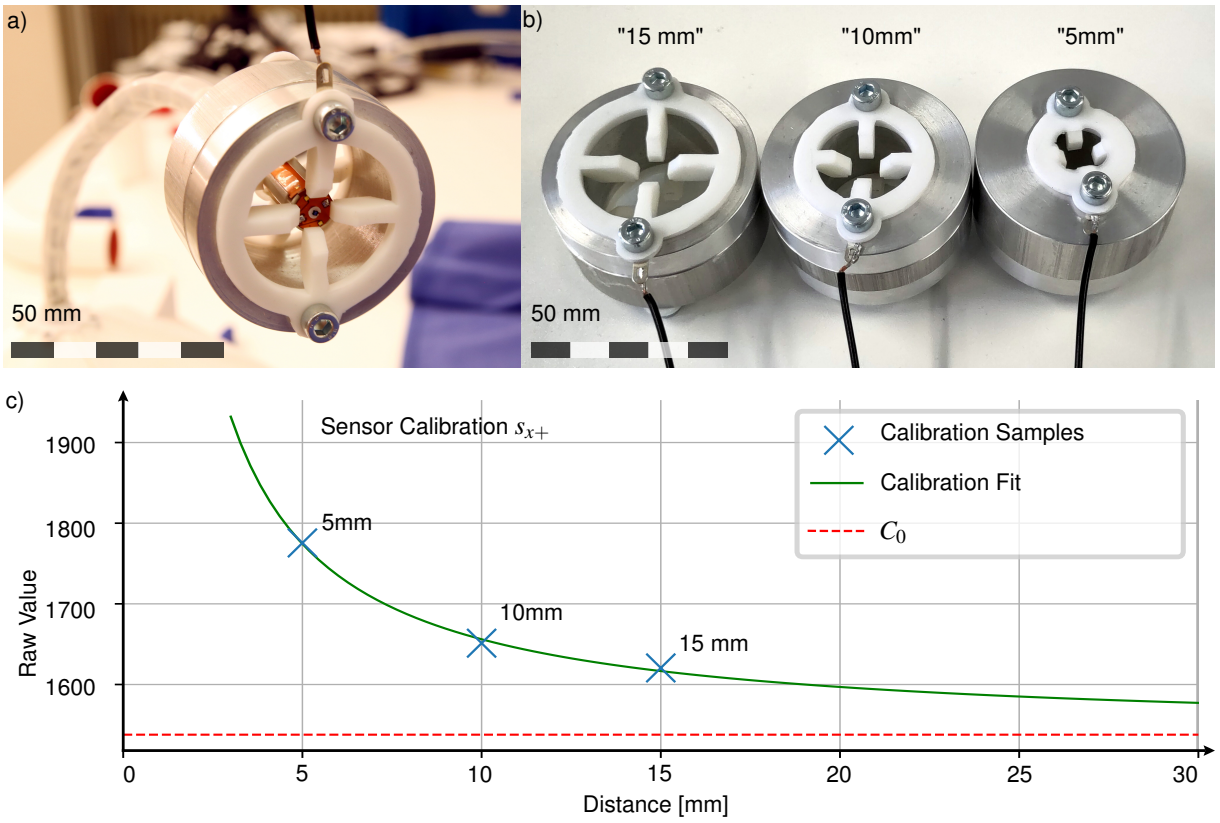

Figure 6.8 – a) The application of the calibration bodies on the robot. b) The three calibration bodies, used for calibration of the sensor. c) An exemplary calibration as least square fit through the three calibration samples. Adapted from [12]

upper limit $s_{\max}$ is defined. Above this level, all raw value changes are considered as noise and the sensor output is set to $s_{\max}$. This provides an equivalent representation to no object detection or an object being out of range. Hence, the calibration functions S_h mapping the raw values to distance values are defined as

$$S_h(E_h) = s_h = \min\left\{\frac{\varepsilon A_h}{|E_h - C_{0,h}|}, s_{\max}\right\}. \tag{6.12}$$

εA_h can now be determined by calibration measurements with an object at known distances. To conduct such an experiment in a simple fashion and with the sensor attached to the robot system, three calibration bodies, shown in Figure 6.8, are designed. These consist of aluminum cylinders with 40 mm, 30 mm, and 20 mm inner radius, respectively. For conducting a calibration, a calibration body is grounded and placed on the robot's sensorized tip. A 3D-printed inlet keeps the sensor centered. This way, each electrode has a distance of 15 mm, 10 mm, or 5 mm to the calibration body's wall. The calibration is repeated for each of the three calibration bodies. The number of samples was chosen to cover the close-, far-, and mid-range of the sensor and as a trade-off of accuracy and practicability. With these three known distances, εA_h can be fitted to the resulting raw values for each electrode using a least-square optimizer. To account for sensor noise, the raw value used for calibration is averaged over a measurement of 50 values. Figure 6.8c plots the resulting calibration curve for an exemplary calibration process.

The calibrated sensor now provides four distance values $s_{X+}, s_{Y+}, s_{X-}, s_{Y-}$. These allow determination of the surrounding's center as in Equation 5.4. Figure 6.9 depicts this principle.

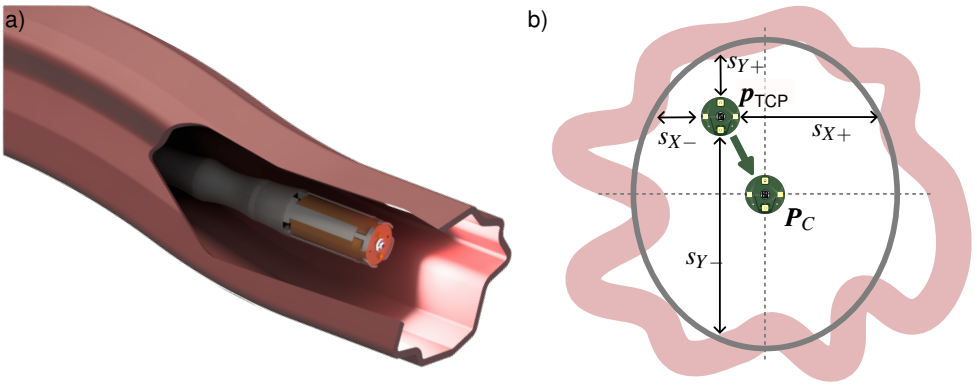

Figure 6.9 – Visualization of the goal determination of the controller. a) The robot should be centered in a hollow organ. b) Therefore, the environment is approximated by an ellipse and the center $\boldsymbol{p}_C$ is targeted. [12]

The determined center is expressed in the TCP's coordinate frame by

$$\boldsymbol{p}_C = \frac{1}{2}\begin{pmatrix} s_{X+} - s_{X-} \\ s_{Y+} - s_{Y-} \\ 0 \end{pmatrix}. \tag{6.13}$$

These center coordinates $\boldsymbol{p}_C$ are passed to the controller as goal state and are then processed as described in the following section.

6.3.3 Controller

The controller's task is to continuously calculate a new actuator configuration $\boldsymbol{q}$ from the current sensor input. Therefore, the sensor provides the current goal position $\boldsymbol{p}_C$ in the TCP's coordinate frame. In each iteration n, $\boldsymbol{p}_C$ is transformed into the robot's base frame and then passed to a solver which solves the linearized inverse kinematics to approximate the new actuator pose $\boldsymbol{q}_{n+1}$. This is then passed to the hardware interface, controlling the servo motors, and a new iteration $n+1$ is started.

The goal position, $\boldsymbol{p}_C$, is provided in the TCP's coordinate frame. To transpose these to robot base frame coordinates $\boldsymbol{p}_b$, the forward kinematics at the current robot configuration $\boldsymbol{q}_n$, given by Equation 6.7, is applied as follows:

$$\begin{bmatrix} \boldsymbol{p}_b \\ 1 \end{bmatrix} = T_{\mathrm{CR}}(\boldsymbol{q}_n)\begin{bmatrix} \boldsymbol{p}_c \\ 1 \end{bmatrix}. \tag{6.14}$$

To create a control command for the motors, a new actuator configuration $\boldsymbol{q}_{n+1}$ needs to be found which minimizes the TCP's deviation e from the goal position:

$$e = T_{\mathrm{CR}}(\boldsymbol{q}_{n+1})\hat{e}_4 - \boldsymbol{p}_b \tag{6.15}$$

with $\hat{e}_4$ being the fourth dimension's unit vector. As the inverse function of $T_{\mathrm{CR}}(\boldsymbol{q})$ does not have a closed form solution, $T_{\mathrm{CR}}(\boldsymbol{q})$ is linearized at the current robot configuration $\boldsymbol{q}_n$, such that the pseudoinverse Jacobian $J^+ = J^T(JJ^T)^{-1}$ can be used to solve for the configuration's derivative $\dot{\boldsymbol{q}}$ as in

$$\begin{bmatrix} \dot{\theta}_x \\ \dot{\theta}_y \end{bmatrix} = \dot{\boldsymbol{q}} = J^T(JJ^T)^{-1}\dot{\boldsymbol{p}}_{\mathrm{b}}. \tag{6.16}$$

For the given CR, the servos do not provide a velocity interface to which $\dot{\boldsymbol{q}}$ could be assigned to. Instead, only a position interface is available. To derive a position command, that can be passed to the robot at the end of the current control cycle, Equation 6.16 is integrated over the duration from control cycle start t_n to the control cycle end t_{n+1}:

$$\boldsymbol{q}_{n+1} = \int_{t_n}^{t_{n+1}} \dot{\boldsymbol{q}} dt = J^{+} \int_{t_n}^{t_{n+1}} \dot{\boldsymbol{p}}_{\mathrm{b}} dt = J^{+}(\boldsymbol{p}_0 - \boldsymbol{p}_{\mathrm{b}}). \tag{6.17}$$

Here, $\boldsymbol{p}_0$ is the robot's current position. Due to the linearization, Equations 6.16 and Equation 6.17 are only valid for small deviations of $\boldsymbol{p}_{\mathrm{b}}$ from $\boldsymbol{p}_0$. In implementation and application, the control cycle is kept short and it can be assumed that the environment changes without major discontinuities or abrupt changes, this supports the assumption of small deviations from the current position to the goal position.

The control loop is implemented in a custom `ROS2-control` controller. It subscribes to the sensor raw values which are published at a rate of 100 Hz. The controller runs at 5 Hz, which allows the usage of a 20-value mean sensor raw value as input for the controller to reduce noise. `ROS2-control` architecture prescribes a hardware interface for the robot. This was implemented as a wrapper of the interface described in Table 6.2. The hardware interface allows loading the robot model parameters from an Unified Robot Description Format (urdf) file and passes them to the implemented kinematic model. This allows for the adaptability of the software to a changed robot design and variations.

6.4 Evaluation

To evaluate the sensorized robot and the controller, an initial qualitative evaluation of the robot's capability for obstacle avoidance is presented. Then, a qualitative analysis is conducted in which the controller's accuracy is evaluated in a dynamic environment.

Obstacle Avoidance Due to limiting the sensed distance to a defined range $s_{\max}$, by Equation 6.12, the sensor is expected to remain at rest when located in open space. However, as the sensor is prone to noise, choosing $s_{\max}$ too large results in the sensor measuring a distance lower than $s_{\max}$ even when operating in open space. This can cause the proximity controller to jitter or drift. Experimentally, $s_{\max} = 40\,\mathrm{mm}$ was found to represent a reliable upper limit of $s_{\max}$, where the system is still stable in open space. With this limit set, the robot is able to conduct motions for obstacle avoidance when an object is approaching. The respective electrode(s) measure a distance below $s_{\max}$ and from Equation 6.13, it can be seen that a new goal is set on the opposite side to the approaching obstacle. Figure 6.10 shows a series of images from such an evasive motion away from an approaching hand. This experiment also demonstrates the sensor's responsiveness to tissue.

Accuracy Evaluation In the following, an experimental setup and an evaluation of the robot's accuracy are presented. In these experiments, the controlled system's position is compared to the ideal center point of a closed environment. The setup for conducting accuracy analysis is shown in Figure 6.11. It consists of a serial manipulator (UR10e, Universal Robots, Ordense, DK), a cylindrical phantom, and an optical tracking setup. To simulate a dynamic environment, in which the proximity controlled CR should center itself, a tubular phantom of 50 mm is created.

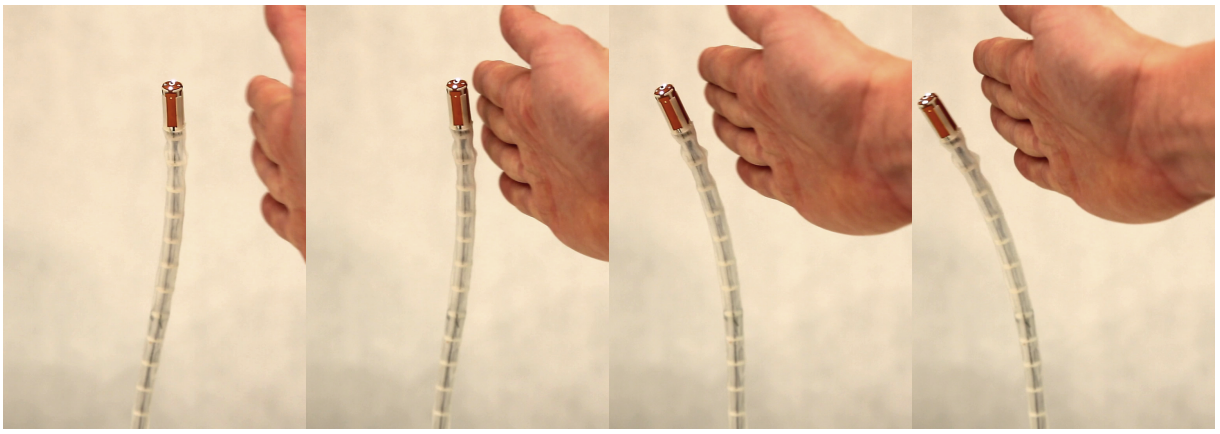

Figure 6.10 – To demonstrate receptiveness to tissue, obstacle avoidance is demonstrated with a hand. The robot conducts evasive motion when approached by a hand. [12]

As presented in Section 5.2.4, the phantom is made from a 3D-printed base with the inner surface revetted with copper foil that is grounded. The phantom is moved by the serial robotic arm on predefined trajectories. The tracking system, described below, is used to track the CR's TCP position relative to the phantom. The tracking system's cameras are rigidly attached to the phantom and the serial robot's end-effector. This allows to compare the trajectory of the phantom's center (i.e., the proximity controller's desired goal) to the actual TCP position during the experiment.

The tracking system consists of two Raspberry Pi 4 (Raspberry Pi Foundation, Cambridge, UK) with a Raspberry Pi HQ camera attached to each. The cameras are equipped with a 6 mm objective lens and are mounted on a rigid frame which also holds the phantom. The cameras are aligned for their fields of view to fully overlap in the phantom's center plane. After mounting, the cameras are intrinsically and extrinsically calibrated. Intrinsic calibration is conducted with a checkerboard pattern, using the default methods by the OpenCV library [203]. For extrinsic calibration, a 3D-printed calibration body is designed, which attaches to the phantom. It consists of nine markers at predefined locations in relation to the phantom's origin. In a subsequent calibration process, the markers are selected in each of the camera's images as user input. This allows to conduct an extrinsic calibration of each of the cameras to the phantom's coordinate frame. This process indirectly provides the cameras' calibration to each other. A tracking algorithm makes use of the CR's camera LEDs: The cameras' objective lenses are set to a small aperture, such that only the LEDs' light is pictured as bright spots and environmental light is suppressed. This facilitates segmentation of the LEDs' location. The center point between the two LEDs marks the CR's TCP. Both cameras record a video during an experiment. Subsequently, the videos can be further processed to provide 3D TCP localization data: The videos are synchronized by the detection of the moment when the LEDs are switched on at the beginning of each experiment. Using the extrinsic calibration, the tracked TCP locations from each image are triangulated to a 3D position of the TCP. Due to the extrinsic calibration to the phantom's coordinate system, the traced coordinates x_k, y_k, z_k for each frame k represent the TCP location as a distance from the phantom's center.

Equipped with this tracking, the phantom is now moved around the CR and in a predefined x-y-pattern, parallel to the table. To achieve this, the phantom and tracking frame are mounted to the serial robot arm's flange. The traced trajectory starts at the CR's TCP, in a neutral position. During the execution of the trajectory, the proximity controller is running. Therefore, the proximity controller causes the CR's tip to follow the trajectory of the phantom's center point,

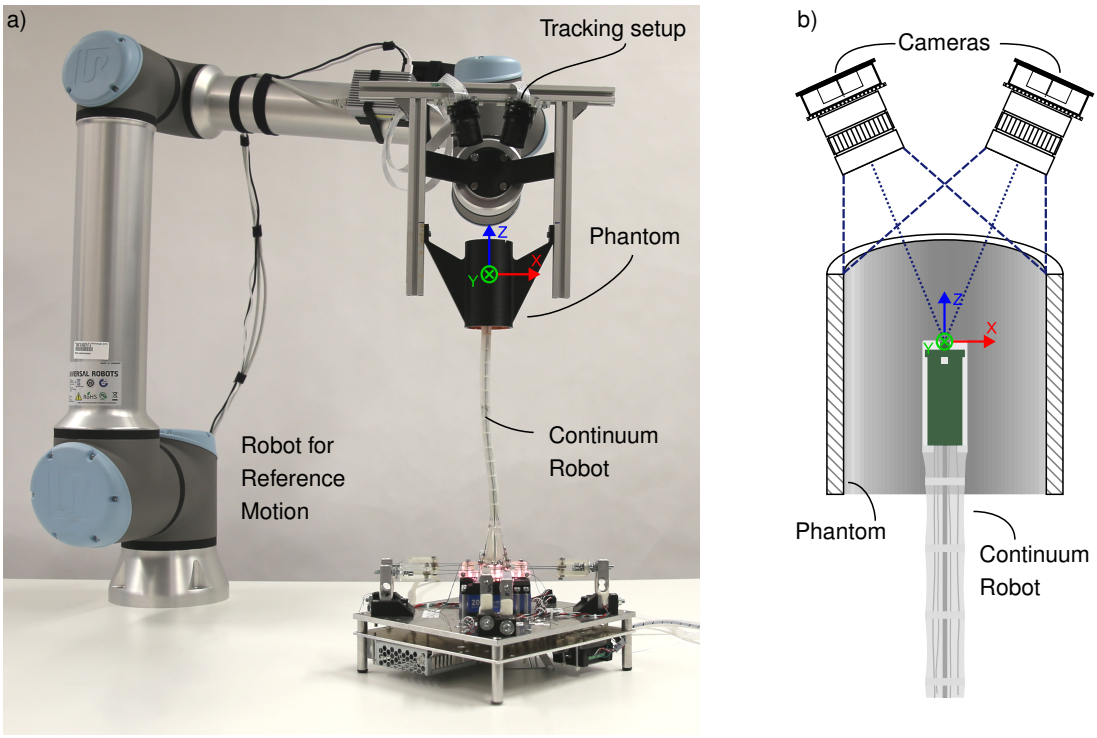

Figure 6.11 – The setup used for accuracy evaluation of the CR. a) The full setup: A robot arm holds the phantom and the tracking setup. The CR's sensorized tip is placed inside of the phantom. As the phantom is moved with the robot arm, the tracking system can evaluate the CR's tip position while the proximity controller is active. b) Concept of the tracking system. For the stereo camera setup, two cameras are aligned to have an overlapping field of view inside of the phantom. A detection algorithm for the CR's tip tracks the robot's motion in relation to the phantom.

during phantom motion. To quantify the controller's accuracy, the tracking system tracks the deviation from the ideal position over time. As a metric for accuracy q_{acc}, the mean Euclidean distance over all m frames

$$q_{\text{acc}} = \frac{1}{m} \sum_{k=1}^{m} \sqrt{x_k^2 + y_k^2} \tag{6.18}$$

is calculated.

As a more practical quantification of controller quality, the relative time of the sensor in contact with the phantom's wall, q_{contact}, is estimated by evaluating

$$q_{\text{contact}} = \frac{1}{m} \sum_{k=1}^{m} \begin{cases} 1, & \text{if } \sqrt{x_k^2 + y_k^2} = 20\,\text{mm}, \\ 0, & \text{otherwise.} \end{cases} \tag{6.19}$$

A sensor distance of 20 mm corresponds to the sensor being in contact with the wall, as the phantom's radius is 25 mm and the sensor exhibits a radius of 5 mm.

The experiment is conducted for a cross-shaped trajectory with an extend of 12 mm and a square-shaped trajectory with 10 mm side length. The coordinates, traced for these trajectories, are listed in Table 6.3, denoted in the CR's TCP coordinate frame, when it is in an upright neutral position. For the execution of the trajectories, the serial robot moves the phantom at a speed of 10 mm.

The results for the square and cross trajectory are visualized in Figure 6.12a and Figure 6.12b. The plots show the trajectory of the phantom's center and the sensor position from

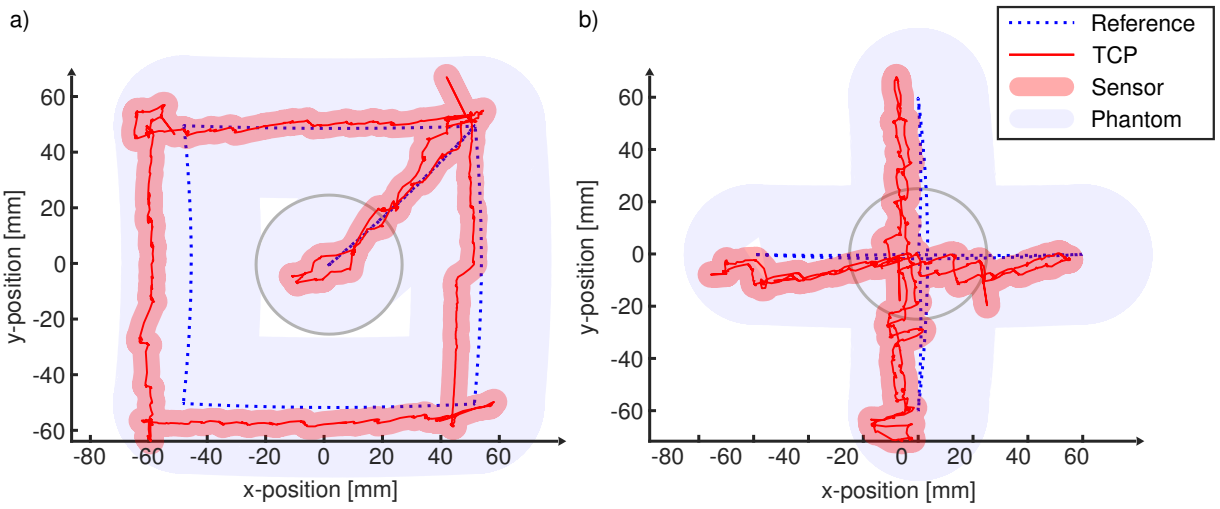

Figure 6.12 – The results of the dynamic accuracy evaluation for the square trajectory a) and the cross trajectory b). The phantom is represented by the trace of its center line (blue dotted line) and the trace of its inner volume (blue shaded area). The motion of the CR's tip, as a result of the proximity control, is traced by the red line (TCP trace) and the red shaded area (sensor volume trace) [12].

the optical tracking system as lines. The spaces occupied by the phantom and the sensor during the experiment are traced as shaded areas. To visualize the phantom's inner size, it is plotted as a circle at the start position. The runs were evaluated with the metric from Equation 6.18. For the square trajectory, an accuracy of (10.37 ± 0.49) mm was calculated. During the execution of the cross trajectory, the controller performed at an average accuracy of (9.62 ± 0.38) mm. Contact could be avoided most of the experiment's time: The square trajectory resulted in $q_{\text{contact}} = 2.07\,\%$. The cross trajectory exhibited a lower contact value of $q_{\text{contact}} = 0.96\,\%$.

To help understand the temporal behavior of the controller, for the square trajectory, the position of the phantom and sensor as well as the positional error are plotted over time, in Figure 6.13.

Centering in a Tubular Environment As an additional, qualitative experiment, further evaluating the system towards an application, an insertion process of the CR into a bent section of an organ is simulated. It aims to provide a proof of concept for the implementation of a controller navigating a CR through a hollow organ. Therefore, a second phantom was created similarly to the one from the previous experiment: The phantom is tubular but with a smaller diameter of 40 mm and the center line following a 40° bend with a bending radius of 40 mm. To provide a responsive inner surface, it is coated with copper. To provide a physiological look for the endoscopic camera, the phantom is additionally coated with a thin layer (<1 mm) of silicone (EcoFlex 0030, KauPo Plankenhorn e.K., Spaichingen, Germany) with red coloring pigments to represent tissue. The phantom is mounted to the serial robot arm's flange and positioned above the CR in a neutral position and with active proximity control. The serial robot then executes a downward motion with the phantom which simulates the insertion of the CR into the phantom.

Table 6.3 – Coordinates of the evaluation trajectories. Units are mm. The coordinates are denoted in the TCP's frame when in the neutral position.

Position #	**1**	**2**	**3**	**4**	**5**	**6**	**7**
Cross	[0, 0]	[-60, 0]	[60, 0]	[0, 0]	[0, -60]	[0, 60]	[0, 0]
Square	[0, 0]	[50, 50]	[-50, 50]	[-50, -50]	[50, -50]	[50, 50]	[0, 0]

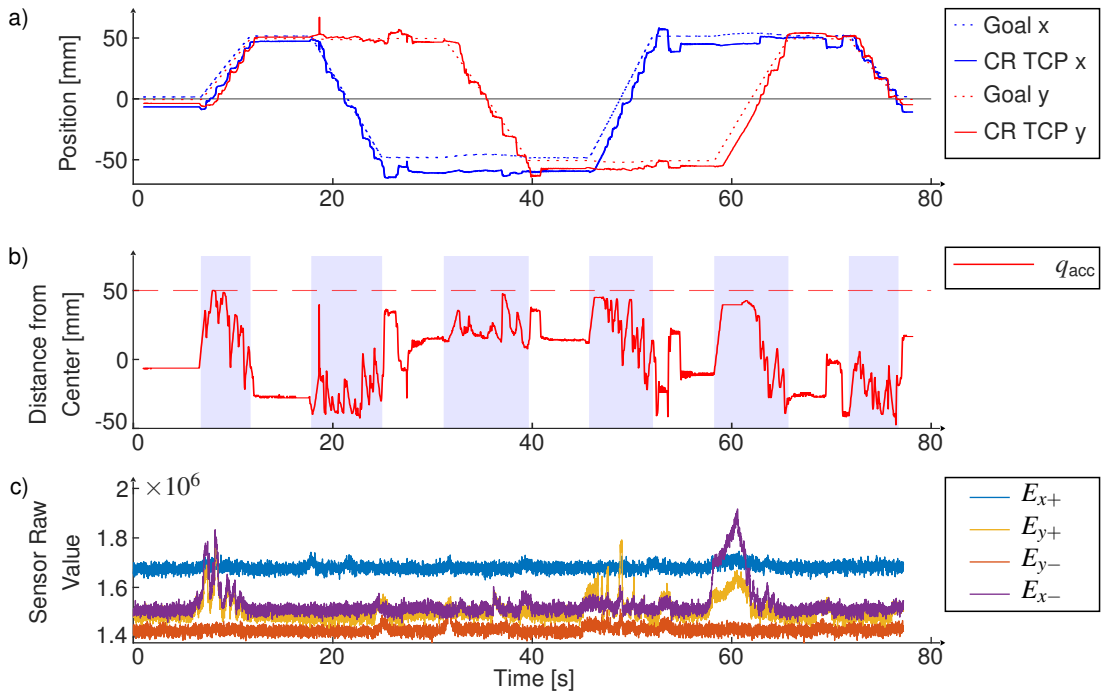

Figure 6.13 – Temporal course of the cross trajectory for accuracy evaluation. a) x- and y-position of CR TCP and the phantom's center as ideal controller goal. b) Course of q_{acc} during the experiment. c) The sensor raw values for all four electrodes. Adapted from [12].

During the insertion process, the controller is tasked with keeping the phantom centered. In this case, this means the robot should follow the phantom's center line and reproduce the phantom's curve.

Figure 6.14a shows the setup and Figure 6.14b, as a result, the CR's end position after passing the phantom. In the endoscopic camera, the corrective movements of the CR to center the robot during the passing of the bent section can be observed.

6.5 Chapter Discussion

The combined system of sensor and CR can be controlled to evade obstacles autonomously and to center itself in a closed environment. The evaluation presented shows significant deviations from the goal state, which partially leads to contact with the phantom's wall. To improve accuracy, further optimization is required. However, the system could demonstrate the applicability of a combination of capacitive, exteroceptive sensing, and continuum robotic actuation. In an endoscopic intervention, no highly dynamic motion of the environment is expected and endoscope control does not necessarily require highly accurate absolute positioning but rather spatial exteroception to refrain from wall contact, and centering to improve visibility of the situs. Yet, for advanced autonomy features, various points could be addressed to improve accuracy. As listed in Section 5.4.1, the sensor could provide a more accurate signal when electrode geometry is optimized, and online calibration could be implemented. Noise in the sensor signal may cause oscillation in the determined goal position $\boldsymbol{p}_c$ and the derived control commands. To address this issue, approaches for improving sensing hardware or digital filtering should be investigated.

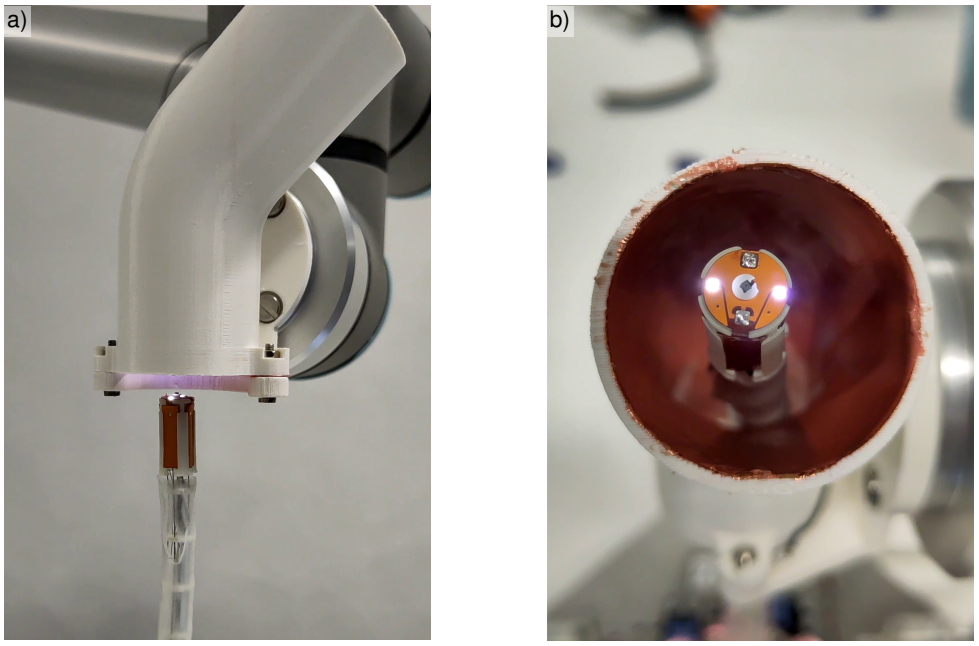

Figure 6.14 – The experiment for center line following. a) The CR before introduction into the curved phantom. b) At the end of the curved phantom, centered at the phantom's exit [12].

Besides sensor signal accuracy, also robot accuracy offers potential for improvement. A fairly simple kinematic robot model was applied for the sake of computation time and simplicity. Applying a more complex model would improve the representation of the robot in the controller. However, to be able to apply the control method presented, the robot's forward model $T_{\mathrm{CR}}(\boldsymbol{q})$ should still be representable in a closed form (cf. Equation 6.7). Only for this case, it is possible to form an analytic solution of the Jacobian J and its pseudoinverse J^{+}. Otherwise, numerical methods have to be applied to solve Equation 6.16.

The robot structure and hardware itself most likely also contribute to the system's error. Overshoots through the compliant structure are not regarded by the controller. Therefore, they can be observed in Figure 6.13 at the times when the phantom is at rest, but the CR tracking shows periodical oscillations. Further investigation could research the introduction of dampening elements in the robot structure or the introduction of dynamics in the robot model.

The combination of proximity sensor and CR creates a system that can conduct evasive motion autonomously and without any user input. The same controller serves for obstacle avoidance in open spaces and centering in closed environments. With the given sensor setup and CR kinematics, the system is restricted in its DOFs concerning motion but also regarding its sensing. As sensing is restricted to four electrodes in $X+, Y+, X-$, and $Y-$ directions, an evasive motion can only be calculated in 2D (i.e., the plane perpendicular to the sensor's center axis). A second ring of sensors would allow the determination of the relative position of the system to an environment in two locations along the CR's body and derive an orientation in three dimensions. As the set-up kinematic model includes the full homogeneous transformation matrix T_{CR} the controller can be easily extended to not only take a goal position into account but also consider a goal with orientation information.

The third experiment demonstrates a proof-of-concept of the controller's capability to allow for center-line following, but also shows limits of the robot's kinematic setup, as contact of proximal parts of the robot, below the robot's tip cannot be avoided. This does not affect the quality of navigation and situs visibility as the tip can still be centered. However, to achieve

a contact-free advancement, a robotic system would require additional DOFs and additional sensors along its body to be able to sense the centralization of a respective robot body part and to allow for null space optimization (i.e., to maintain the robot's TCP at its pose while conducting evasive motion with a proximal part of the CR). Another approach to this issue is the implementation of kinematics which allows for a *follow-the-leader* motion. With this, the robot conducts a non-holonomic motion, i.e., its body only occupies space which is part of the TCP's trajectory during advancement. Approaches, addressing this issue are for example presented in [99].

7 Discussion

In this chapter, the presented results are discussed collectively and their significance for the overall goal of this thesis is elaborated. Section 7.1 discusses common aspects of accuracy and calibration in the presented methods, and provides a comparison to the state of the art. Section 7.2 addresses mutual limitations and their interaction focusing on actuation (Section 7.2.1) and sensing (Section 7.2.2). Section 7.3 projects the thesis' findings on the research questions of this thesis, introduced in Section 1.2.

7.1 Consolidated Analysis and Discussion

Each method of this thesis presents a discussion of its results. To link the individual results, the following section discusses the interdependence of the results and findings and puts them into the application's perspective.

Accuracy A general challenge all presented methods are facing is low accuracy. The systems presented are developed for a proof of concept, and the underlying principles were to be demonstrated. This resulted in an overall system that still offers various working points for optimization as illustrated in each method's discussion. However, it should also be pointed out, that in such a demanding field of application, such as MIS, absolute accuracy is not the primary concern. During an endoscopic intervention, a surgeon does not rely on precise information about the position of the endoscope's tip in relation to the handpiece (or robot base). Similarly, in colonoscopy, the exact distance of the camera to the colon's wall is not of primary interest, as long as centering of the distal tip provides sufficient sight and reduces the risk of perforation or constriction. The fact that only a few to no systems are available that provide such information (even at low accuracy), highlights the need for research in the field of sensor-actor systems with in situ spatial exteroception for MIS. Despite the low accuracy presented, Section 8.2 will point out, that there are many promising points of action to improve the accuracy of the investigated systems. Especially, advanced robotic applications and surgical process automation would benefit from reliable sensor values and precise robot actuation.

The presented method of exteroception-based control competes with similar methods especially based on vision (i.e., the integrated camera) [55–57] and optical fiber sensors [132, 133]. Both are sensing modalities that can hardly present highly accurate measurements. The cited works do not provide results that allow for a directed comparison of the accuracy, but their findings report similar challenges. Van der Stap et al. evaluate their approach by comparing the image-based target pose to an experienced surgeon's choice and evaluate their systems *success rate* of conforming to this choice by an intra-class correlation analysis as a metric for image similarity. They could present a success rate of 84.7 % to 98.8 % [56]. Chen et al. could demonstrate their system's ability to avoid touching the wall (a distance of $> 0.8\,\mathrm{mm}$ could be maintained) while being inserted into a tubular phantom. An accuracy measurement is not

presented. For the comparison of this system, and the CR presented in Chapter 4 it should be noted, that the aspect ratio of length to width of a continuum robotic system plays a crucial role in its stability and ability for accurate control. While Chen's presented system comprises an approximate actuated length of 100 mm[1] and a diameter of 17 mm, it comprises an aspect ratio of 5.8. In contrast, the robot presented in this thesis comprises a length of 260 mm and a diameter of 10 mm, resulting in an aspect ratio of 26. The controlled system by Liu et al. could present an average error of –0.93 mm for maintaining a nominal distance of 5.2 mm to an object. Their system comprises an aspect ration of $360\,\text{mm}/20\,\text{mm} = 18$. Here, as diameter the average diameter was used as the robot is cone-shaped with a diameter range of 30 mm to 10 mm diameter.

This comparison to the literature shows, that accuracy is a general challenge in this field of research. The robot presented in this thesis already comprises one of the highest aspect ratios compared to similar robotic systems researched. A higher aspect ratio correlates with a higher effect of leveraging, impeding accurate control. Nevertheless, such an aspect ratio is required for endoscopy and MIS and should be aimed for in minimally invasive robotic systems. For comparison, the commercial gastroendoscope utilized in Chapter 5 (see Figure 2.1b) comprises a length of 2000 mm and 9.2 mm diameter (aspect ratio of 217). This illustrates the need for high aspect ratio robotic systems and the contribution of the presented method.

Sensor Calibration In this thesis, three different methods for the mapping of the capacitive raw value to a proximity or contact value are investigated:

1. Section 5.2 applies an extensive calibration procedure to create a lookup table-based calibration.
2. Section 5.3 achieves a binary classification on a purely data-driven method without the need for a preceding calibration process.
3. Section 6.3.2 introduces an intermediate calibration process based on only a few calibration samples.

Calibration method (1) is associated with the most effort for calibration and requires the robotic setup presented in Figure 5.7. This restricts the versatility of the calibration method, as the sensor needs to be calibrated before integration or needs to be detachable as in the given method. However, this method results in the most accurate mapping of raw value to distance, as for each possible raw value a corresponding distance can be assigned from a physical measurement. Conducting the calibration of the sensor when it is already integrated into the robot would result in a complex calibration method. Considering a calibration method that is more suitable for application in or close to the OR, the calibration process (3) was implemented for the integrated continuum robotic setup. The amount of sample points acquired for calibration is crucially reduced (from the full range of sensor raw values) to three samples. A reciprocal model function, as presented in Equation 6.11, is fitted to these samples as a regression for the mapping from raw value to distance. The model function is derived from a first approximation of the physical setup and respectively a strong simplification. The number of calibration samples (i.e., three) was chosen for practicability and could be varied to improve the sensing results. As an investigation of further reduction of the sample size, calibration method (3) investigates an approach that requires no calibration. It is based on the a priori knowledge, that the sensor responds to

[1] The precise value is not denoted in the publication and estimated from the images presented in [132].

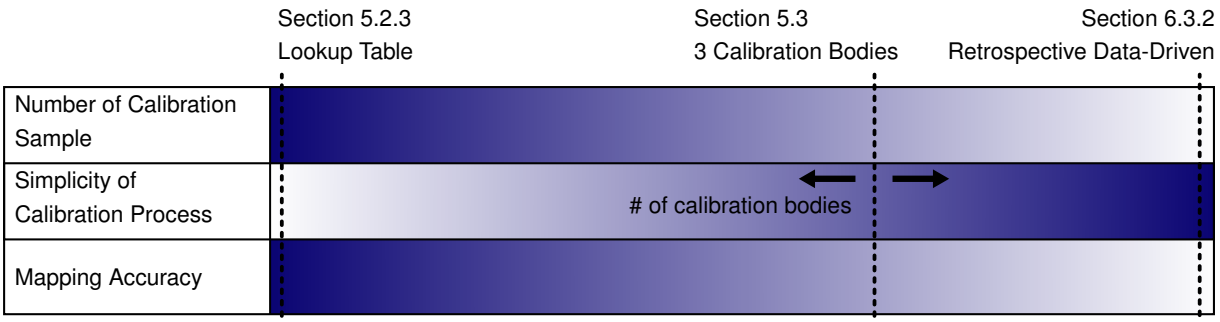

Figure 7.1 – Qualitative comparison of the three investigated calibration methods for sensing. The calibration as lookup table, as presented in Section 5.2.3 trades off a high number of calibration samples and a resulting high mapping accuracy with a high effort for conducting the calibration process. The retrospective data-driven method, presented in Section 5.3, presents contrary features of low accuracy but also low (or none) calibration effort. The usage of calibration bodies as suggested in Section 6.3.2 presents an intermediate method in which effort and accuracy can be varied through the number of calibration bodies utilized.

contact, and a high raw value correlates to contact and a low sensor signal correlates to no contact. On such a base, the sensor signal output is classified as contact and non-contact, using the sensor data history. The presented implementation only allows for a retrospective analysis of the data and is not directly suitable for the mapping to a distance value. Compared to methods (1) and (2) this results in less information provided by the sensor, which was only sufficient for the presented use case of contact classification. The three presented calibration methods demonstrate the versatility available for capacitive sensing concerning raw data processing on the one hand. On the other hand, they highlight the need for careful consideration of the applied calibration method, as typically calibration effort and practicability are in trade-off with achievable accuracy. Figure 7.1 summarizes the comparison of the three calibration methods graphically.

7.2 Limitations

As an addition and summary to the limitations listed in each of the method chapter's discussions, this section discusses limitations of the overall approach, divided into actuation and sensing. In Chapter 8, approaches to address limitations are presented and discussed.

7.2.1 Actuation

The robotic system introduced in Chapter 4 and then integrated into the system from Chapter 6 exhibits drawbacks from being a proof of concept setup. As a research setup, its manufacturing comprises a large portion of manual assembly steps. This results in the introduction of inaccuracies and lack of repeatability for the setup. The studies were conducted with one physical setup, so no statement regarding the repeatability of the setup's manufacturing can be made, and the evaluation of the performance can only be assumed to be transferable to an equal setup.

The imprecision of the selected manufacturing methods also contributes to the hysteresis that could be observed in the robot's motion. Especially, in the robot's neutral position, the clearance in the channels for tendon guidance and backbone fixture results in sudden jumps, as tension changes from one tendon to the antagonistic one. Furthermore, the servo motors also contribute to motion accuracy: As they are controlled with an 8-bit integer PWM value,

they provide a low position resolution of 256 steps over their range of −135° to 135°. For the proximity-controlled robot, this means that the complete workspace only consists of $256 \times 256 = 65536$ possible robot poses, due to the control rule in Equation 6.1. As the controlled system utilizes only a small fraction of the robot's full workspace, discretization effects are likely to affect the system's accuracy. The independent control of both of the robot's segments could improve the accuracy of the controlled system as two additional DOFs could be utilized to control the robot tip's pose. Therefore, another limitation lies in the kinematic model, based on a single constant curvature representation of the robot system. The robot's hardware is prepared for more complex kinematic modeling, taking the tendon forces into account. As a result, the robot model could be extended to deviate from the constant curvature assumption and take tendon forces as well as tendon (or tendon drum) positions into account.

7.2.2 Sensing

As discussed in Section 7.1 the results of the evaluation show limited accuracy. While this is also a challenge in all works that present similar systems for MIS, it does represent a limitation that hinders the application of such spatial sensing in minimally invasive tools and robots. A further limitation of the sensing resulted from a limited range of the sensors. While the required range for colonoscopy could be reached by setting an adequate maximum range, Figure 6.13c indicates the low signal-to-noise ratio that is to be expected for far-range obstacles and environmental borders.

Capacitive sensing in general gains attractiveness for application in surgical interventions through the wide range of options available for integration. A versatile and facile electrode design allows the implementation of disposable and economically efficient electrodes. E.g. in the form of a disposable drape or add-on sensor. While this work could demonstrate a rigid add-on sensor for an endoscope's tip, it lacks the demonstration of electrodes implemented in soft covers or drapes, which would be ideal for surgical applications. In the presented robot, the electrodes were integrated in a manner that would require the disposal of the full robot body in a single-use design, as the electrodes were integrated into the rigid robot tip and not in the elastic drape.

To fully support the thesis that capacitive proximity sensing is a suitable candidate for surgical interventions, more research needs to be conducted, which takes the unidealized circumstances into account. In real-world applications of surgical or therapeutic interventions, the lumens are subject to debris and liquids. Even after an enema in the colon or in the comparably clean trachea or bronchi, humidity and mucosa will be present. This work was limited to phantoms that did not comprise a humid environment or to ex vivo phantoms in situations that could ensure no direct contact with wet objects. Preliminary experiments on the moistening of the sensor surface and successive removal resulted in a reversible offset of the sensor readings. This indicates, that liquid contact does not fully prevent achieving a distance value but knowledge of the context is required to reconstruct a distorted sensor reading. Possible options to achieve this are discussed in Section 8.2.

7.3 Review of the Research Questions and Contributions

In this thesis, the automation of an endoscopic continuum robot, with integrated exteroception for proximity could be demonstrated. The intermediate developments of the continuum robot

platform and the proximity sensor could also contribute its findings to the field of research. The following section summarizes the contributions of this thesis as well as the answers to the research questions introduced in Section 1.2.

Research Question Q1:

How can a continuum robotic platform be designed to be suitable for minimally invasive intervention but also fulfill requirements for sensor integration and sensor-based control?

Chapter 4 addressed question Q1 of how a continuum robot platform can be designed to provide access to the situs in a minimally invasive manner. The presented investigation contributes a method, providing a continuum robotic setup with antagonistic actuation and proprioceptive force sensing on each tendon. Through the antagonistic actuation, the number of motors in the presented robot can be minimized and the footprint is kept small for the setup to be suitable for application in the OR [9].

Research Question Q2:

How can capacitive sensing be applied to provide exteroceptive information such as proximity and contact to a minimally invasive instrument or robotic system?

In Chapter 5 focus was put on question Q2 of how spatial information can be made available in situ when conducting a minimally invasive intervention. While methods from literature for such sensing have only investigated fiber-based optical sensing, this chapter contributes a method based on capacitive proximity sensing as a cost-efficient and versatile sensing modality. This supports the development of disposable endoscopic and therapeutic devices with integrated proximity [10] or contact [11] sensing as feedback for navigation or automation.

Research Question Q3:

How can capacitive sensing and a continuum robot control be integrated into closed-loop control, and how can a method for controlling such a system be formulated?

To leverage the benefits from both preceding contributions, Chapter 6 investigated question Q3 of how capacitive proximity sensing can be integrated into the new continuum robotic system to allow for closed-loop control. As a result, a sensor-actor system and a method for a closed-loop controller that allows for autonomous centering in a hollow organ were presented. The controller provides the capacitive spatial information to an inverse kinematic model of the endoscopic CR to control the robot tip's position for camera view optimization or navigation [12].

Superordinate Research Question:

How can capacitive sensing and continuum robotics form a closed loop controlled system, which can utilize the capacitive sensing as exteroceptive input for automation in MIS?

The combination of these three research questions investigated in this thesis pushes forward the field of sensor systems and methods suitable for application in MIS. Capacitive proximity sensing can be combined with continuum robotic actuation in an endoscopic continuum robot. The controlled system with capacitive exteroceptive feedback demonstrated the presented methods' potential for novel autonomy capabilities in endoscopic and minimally invasive surgical robots.

8 Conclusion

As a closing chapter of this thesis, in the following, the results and their discussion are summed up and an outlook for suggested future research directions is provided. The following Section 8.1 summarizes the thesis' methods and findings as a take-home message for the reader. Building on the limitations presented in Section 7.2, Section 8.2 suggests ideas for future work, necessary to address the presented limitations and to further advance the methods and systems.

8.1 Summary

The three major contributions of this thesis are a novel endoscopic continuum robot (Chapter 4), the acquisition of in situ spatial information by capacitive sensing (Chapter 5), and the presentation of a closed-loop system combining continuum robot and minimally invasive spatial sensing (Chapter 6).

For the design of CRs, a novel actuation method was presented, which applies antagonistic actuation with a single motor per tendon pair, while still providing tendon force sensing on each tendon individually. This results in the compact 4-DOF continuum robotic setup, meeting the requirements for research on surgical continuum robots, shown in Figure 4.2.

To provide a surgeon or an autonomous surgical robot with spatial information on the situs, capacitive sensing is investigated. The resulting sensor could demonstrate its ability to provide localization information in a hollow organ. As an add-on sensor on a conventional endoscope, it can provide centering feedback to an endoscopist.

Integrated into the presented CR, the sensor can provide spatial feedback which is utilized for autonomous centering in a dynamic environment. The developed algorithm implements a proximity controller that transforms the sensor data to a goal position for the CR's inverse kinematics. The controller is then utilized to demonstrate the new centering capabilities in an endoscopic continuum robotic setup, comprising the sensor as well as camera and illumination (see Figure 6.4).

These contributions demonstrate the potential of capacitive sensing in combination with continuum robotic actuation for autonomy in robotic MIS and endoscopy. The remaining challenges mainly concern the optimization of the robot and sensor for improved accuracy and the investigation of the sensor's behavior in humid environments.

8.2 Open challenges

Manufacturing To improve the robotic system's hardware, the robot platform's design could undergo some revisions. The system's accuracy would benefit from the introduction of professional manufacturing processes for the manufacturing of parts. Parts for which not only

precision but also stability is crucial, are the robot's spacer discs, the robot base, and the tendon pulleys. As they are currently 3D printed from plastic material by SLA, their geometry can deviate from the designed shape and they are prone to wear. Micromachining or laser cutting these parts from metal could improve the robot's accuracy and reliability. Similarly, the NiTi backbone is affected by the spacers being glued to it, the research of a suitable joining process could help reduce the robot hysteresis.

Actuation The resolution of the applied servo motors furthermore limits the robot's motion. Here, high-resolution motors and motor drivers could not only benefit a higher resolved workspace but also provide a velocity interface that could be utilized by the controller as in Equation 6.16. This would also be required for the investigation of the dynamic behavior and modeling of the continuum robot indicated in Section 6.5. As CR control is an active field of research, the presented setup can be applied to implement, test, and compare various kinematic models. Here, the robot's force-sensing capabilities can be utilized for a closed-loop kinematic model, based on tendon force proprioception. Such a model also brings the opportunity to improve the robot's position accuracy and leverage its possibilities of fully independent four-DOF actuation.

In the presented approach, tendon-driven actuation was selected as an actuation technology due to its effectivity and simplicity. As an alternative, the intrinsic actuation with solid-state actuators could facilitate increasing the number of DOFs and miniaturizing the CR. Solid-state actuators still require further research to be suitable for a system as presented in this thesis. Nevertheless, these actuators are attractive candidates for continuum robotic designs, as they show the potential for highly miniaturized intrinsic actuation, which would enable highly actuated, small-scale endoscopic CRs. To support this development, research accompanying the work on this thesis has been conducted on light-actuated materials. Such actuators would allow for the design of MRI compatible CRs, additionally to the benefits of miniaturization [204]. (A summary of this work is provided in the Appendix A.2).

Sensor Improving the sensor performance would have a strong influence on the achievable accuracy of the autonomous centering controller. Currently, the sensor circuit is not optimized for this specific use case. In the measurement bridge that is implemented on the sensing unit, a comparative resistor can be tuned to a working point of the nominal capacitance of the robot's sensing electrodes. This would result in an increased signal-to-noise ratio, which is of special relevance for far-range objects. The electrode design itself can also be the focus of further optimization. As investigated in [205], the geometry (especially distance and surface coverage) of the shielding layer has a strong influence on the sensor's directivity and range. Similarly, the electrode surface could be optimized for the given use case, a larger surface will result in an improved sensitivity. The mentioned parameters could be optimized in a parameter study to determine an ideal sensor geometry, improving sensor accuracy and range.

To address the challenge of humidity influence on the sensor. Various countermeasures can be investigated. On a physical level, liquid adhesion to the electrode surface can be reduced by investigation of hydrophobic coatings on the sensor surface. Here, the challenge contains, on the one hand, the examination of the characteristics of the fluids present in a minimally invasive intervention, and its adhesion to a coated surface. On the other hand, a respective coating's biocompatibility for a biomedical application can pose a challenge. On the level of signal processing, the first step to be investigated would be the detection of a liquid contamination of the sensor surface. Knowledge about such could allow for an offsetting of the liquid's influence

or a recalibration. The research on online recalibration in general could be a crucial factor to the applicability of capacitive sensing in MIS. Capacitive signal offsetting can occur due to many influences. A priori knowledge of the sensed scene or input from other sensing modalities could provide valuable information that could be used for an online recalibration of the capacitive sensing system. Hereby, also the capacitive signal's history could be investigated for pattern detection on possible indications for recalibration. Data-driven methods could leverage the respective detection and determine updated calibration parameters. The classification conducted for contact information in Section 5.3 can be seen as a first, very basic approach and could be developed further to be not only used for retrospective classification but for online recalibration of the sensor.

The hypothesis, that capacitive sensing could also work in a humid or wet environment is supported by reports on fish which discover their environment using electrical field sensing organs [206]. Such observation can be researched to implement biomimetic approaches as suggested by Smith et al. Based on such a principle they developed a sensor and control algorithm for pretouch alignment of a robotic gripper [207]. While their approach addresses a dry environment, further investigation of the biological sensing mechanisms in these fish could be transferred to humid and wet environments for approaches in MIS.

For the application in endoscopic devices, the fusion of the presented capacitive sensing method with image-based localization methods should be investigated. As in most minimally invasive interventions, a camera (i.e., an endoscope) is present, visual information is almost always available. Section 3.3.2 shortly introduced research investigating visual spatial feedback for instrument or robot localization. As a foundation of a suitable image processing method in future research, the acquisition of displacement sensing in a surgical scenario was also investigated during the work on this thesis. The findings have been published in [208] and are summarized in Appendix A.1.

Transfer to an Application As an ultimate evaluation of the system's suitability for application in surgery, the full system has to be evaluated in its dedicated use cases and under review by the surgical experts it is aimed at. In the end, the system will only be relevant to the field of therapeutics or surgery, if surgeons find its usage helpful and supportive. Consequently, user studies should be conducted to evaluate the system's practicability in scenarios close the real-world applications. As a starting point, this could be phantom experiments on artificial models of the trachea or colon, in which endoscopic interventions can be simulated with the system and its autonomy capabilities. They could be conducted similarly to the evaluation presented in [57, 58]. Such studies result in user feedback on the practicable usage and are likely to also address aspects of ergonomics and human-machine interfaces [209]. Only if such aspects are successfully addressed in the development of an automated minimally invasive continuum robot, it can unfold its potential for restoring the restricted access and restricted perception in MIS and support surgery for surgeon and patient.

Bibliography

[1] A. Gamal, M. C. Moschovas, A. R. Jaber, et al. “Clinical Applications of Robotic Surgery Platforms: A Comprehensive Review”. In: *Journal of Robotic Surgery* 18.1 (Jan. 2024), p. 29. ISSN: 1863-2491. DOI: 10.1007/s11701-023-01815-4. URL: https://doi.org/10.1007/s11701-023-01815-4.

[2] M. Yip, S. Salcudean, K. Goldberg, et al. “Artificial Intelligence Meets Medical Robotics”. In: *Science* 381.6654 (2023), pp. 141–146. DOI: 10.1126/science.adj3312. URL: https://www.science.org/doi/abs/10.1126/science.adj3312.

[3] J. Burgner-Kahrs, D. C. Rucker, and H. Choset. “Continuum Robots for Medical Applications: A Survey”. In: *IEEE Transactions on Robotics* 31.6 (2015), pp. 1261–1280. DOI: 10.1109/TRO.2015.2489500.

[4] C. Winters, V. Subramanian, and P. Valdastri. “Robotic, Self-Propelled, Self-Steerable, and Disposable Colonoscopes: Reality or Pipe Dream? A State of the Art Review”. en. In: *World J Gastroenterol* 28.35 (Sept. 2022), pp. 5093–5110.

[5] A. Darzi and Y. Munz. “The Impact of Minimally Invasive Surgical Techniques”. In: *Annual Review of Medicine* 55.1 (2004). PMID: 14746519, pp. 223–237. DOI: 10.1146/annurev.med.55.091902.105248. URL: https://doi.org/10.1146/annurev.med.55.091902.105248.

[6] A. Trecca, F. Catalano, A. Bella, et al. “Robotic Colonoscopy: Efficacy, Tolerability and Safety. Preliminary Clinical Results from a Pilot Study”. In: *Surgical Endoscopy* 34 (2020), pp. 1442–1450. DOI: 0.1007/s00464-019-07332-6.

[7] A. Shergill and C. Harris Adamson. “Failure of an Engineered System: The Gastrointestinal Endoscope”. In: *Techniques in Gastrointestinal Endoscopy* 21.3 (2019), pp. 116–123. DOI: 10.1016/j.tgie.2019.02.001.

[8] E. L. White, M. C. Yuen, J. C. Case, et al. “Low-Cost, Facile, and Scalable Manufacturing of Capacitive Sensors for Soft Systems”. In: *Advanced Materials Technologies* 2.9 (2017), p. 1700072. DOI: https://doi.org/10.1002/admt.201700072. URL: https://onlinelibrary.wiley.com/doi/abs/10.1002/admt.201700072.

[9] C. **Marzi**, F. Buck, and F. Mathis-Ullrich. “Continuum Robot Actuation by a Single Motor per Antagonistic Tendon Pair: Workspace and Repeatability Analysis”. In: *at - Automatisierungstechnik* 71.7 (2023), pp. 528–536. DOI: 10.1515/auto-2023-0066. URL: https://doi.org/10.1515/auto-2023-0066.

[10] C. **Marzi**, H. Alagi, O. Rau, et al. “Capacitive Proximity Sensor for Non-Contact Endoscope Localization”. In: *2022 International Conference on Robotics and Automation (ICRA)*. May 2022, pp. 9614–9620. DOI: 10.1109/ICRA46639.2022.9811734.

[11] N. Greenidge, J. Martin, C. **Marzi**, et al. “Restoring the Sixth Degree of Freedom in the Robotic Manipulation of Mesoscale Magnetic Devices Using the Oloid Shape”. In: *IEEE Robotics and Automation Letters* (2024). Currently prepared for publication.

[12] C. **Marzi**, M. Themistocli, B. Hein, et al. “Proximity Servoed Minimally Invasive Continuum Robot for Endoscopic Interventions”. In: *IEEE Transactions on Medical Robotics and Bionics* (2024), pp. 1–1. DOI: 10.1109/TMRB.2024.3464127.

[13] K. H. Fuchs. “Minimally Invasive Surgery”. EN. In: *Endoscopy* 34.02 (Aug. 2002), pp. 154–159. ISSN: 0013-726X. DOI: 10.1055/s-2002-19857. URL: https://doi.org/10.1055/s-2002-19857.

[14] R. Berguer, W. D. Smith, and Y. H. Chung. “Performing Laparoscopic Surgery is Significantly More Stressful for the Surgeon than Open Surgery”. In: *Surgical Endoscopy* 15.10 (Oct. 2001), pp. 1204–1207. ISSN: 1432-2218. DOI: 10.1007/s004640080030. URL: https://doi.org/10.1007/s004640080030.

[15] F. Powell and A. Khaund. “Laparoscopy and Laparoscopic Surgery”. In: *Obstetrics, Gynaecology & Reproductive Medicine* 26.10 (2016), pp. 297–303. ISSN: 1751-7214. DOI: https://doi.org/10.1016/j.ogrm.2016.07.004. URL: https://www.sciencedirect.com/science/article/pii/S1751721416301737.

[16] J. P. Pearl and J. L. Ponsky. “Natural Orifice Translumenal Endoscopic Surgery: A Critical Review”. In: *Journal of Gastrointestinal Surgery* 12.7 (July 2008), pp. 1293–1300. ISSN: 1873-4626. DOI: 10.1007/s11605-007-0424-4. URL: https://doi.org/10.1007/s11605-007-0424-4.

[17] P. Merloz, J. Troccaz, H. Vouaillat, et al. “Fluoroscopy-Based Navigation System in Spine Surgery”. In: *Proceedings of the Institution of Mechanical Engineers, Part H: Journal of Engineering in Medicine* 221.7 (2007). PMID: 18019467, pp. 813–820. DOI: 10.1243/09544119JEIM268. URL: https://doi.org/10.1243/09544119JEIM268.

[18] V. J. Weiss and A. B. Lumsden. “Minimally Invasive Vascular Surgery: Review of Current Modalities”. In: *World Journal of Surgery* 23.4 (Apr. 1999), pp. 406–414. ISSN: 1432-2323. DOI: 10.1007/PL00012316. URL: https://doi.org/10.1007/PL00012316.

[19] M. J. Mack. “Minimally Invasive Cardiac Surgery”. In: *Surgical Endoscopy And Other Interventional Techniques* 20.2 (Apr. 2006), S488–S492. ISSN: 1432-2218. DOI: 10.1007/s00464-006-0110-8. URL: https://doi.org/10.1007/s00464-006-0110-8.

[20] E. P. W. .-. van der Putten, R. H. M. Goossens, J. J. Jakimowicz, et al. “Haptics in Minimally Invasive Aurgery – A Review”. In: *Minimally Invasive Therapy & Allied Technologies* 17.1 (2008). PMID: 18270873, pp. 3–16. DOI: 10.1080/13645700701820242. URL: https://doi.org/10.1080/13645700701820242.

[21] T. A. d. C. Visconti, J. P. Otoch, and E. L. d. A. Artifon. “Robotic Endoscopy. A Review of the Literature”. en. In: *Acta Cir Bras* 35.2 (Apr. 2020), e202000206.

[22] P. P. Rao. “Robotic Surgery: New Robots and Finally some Real Competition!” In: *World Journal of Urology* 36.4 (Apr. 2018), pp. 537–541. ISSN: 1433-8726. DOI: 10.1007/s00345-018-2213-y. URL: https://doi.org/10.1007/s00345-018-2213-y.

[23] I. Intuitive Surgical. *Intuitive Annual Report 2022*. https://isrg.intuitive.com/. Nov. 2023.

[24] N. Mayor, A. S. Coppola, and B. Challacombe. “Past, present and future of surgical robotics”. In: *Trends in Urology & Men’s Health* 13.1 (2022), pp. 7–10. DOI: https://doi.org/10.1002/tre.834. URL: https://wchh.onlinelibrary.wiley.com/doi/abs/10.1002/tre.834.

[25] B. S. Peters, P. R. Armijo, C. Krause, et al. “Review of Emerging Surgical Robotic Technology”. In: *Surgical Endoscopy* 32.4 (Apr. 2018), pp. 1636–1655. ISSN: 1432-2218. DOI: 10.1007/s00464-018-6079-2. URL: https://doi.org/10.1007/s00464-018-6079-2.

[26] C. P. Pox, L. Altenhofen, H. Brenner, et al. “Efficacy of a Nationwide Screening Colonoscopy Program for Colorectal Cancer”. English. In: *Gastroenterology* 142.7 (2012). Cited by: 228, 1460–1467.e2. ISSN: 00165085. DOI: 10.1053/j.gastro.2012.03.022. URL: https://www.scopus.com/inward/record.uri?eid=2-s2.0-84861639726&doi=10.1053%2fj.gastro.2012.03.022&partnerID=40&md5=a303e3d9d10a452089a9d62b1515de32.

[27] J. L. Ponsky and A. T. Strong. “A History of Flexible Gastrointestinal Endoscopy”. In: *Surgical Clinics of North America* 100.6 (2020). Endoscopic Surgery, pp. 971–992. ISSN: 0039-6109. DOI: https://doi.org/10.1016/j.suc.2020.08.013. URL: https://www.sciencedirect.com/science/article/pii/S0039610920301092.

[28] G. Berci and K. A. Forde. “History of Endoscopy”. In: *Surgical Endoscopy* 14.1 (Jan. 2000), pp. 5–15. ISSN: 1432-2218. DOI: 10.1007/s004649900002. URL: https://doi.org/10.1007/s004649900002.

[29] S. G. Lim. “The Development of Robotic Flexible Endoscopic Platforms”. In: *Int J Gastrointest Interv* 9.1 (2020), pp. 9–12. DOI: doi.org/10.18528/ijgii190022.

[30] N. Kurniawan and M. Keuchel. “Flexible Gastro-intestinal Endoscopy — Clinical Challenges and Technical Achievements”. In: *Computational and Structural Biotechnology Journal* 15 (2017), pp. 168–179. ISSN: 2001-0370. DOI: https://doi.org/10.1016/j.csbj.2017.01.004. URL: https://www.sciencedirect.com/science/article/pii/S2001037016300617.

[31] K. Kume. “Flexible Robotic Endoscopy for Treating Gastrointestinalneoplasms”. en. In: *World J Gastrointest Endosc* 15.6 (June 2023), pp. 434–439.

[32] G. Ciuti, K. Skonieczna-Żydecka, W. Marlicz, et al. “Frontiers of Robotic Colonoscopy: A Comprehensive Review of Robotic Colonoscopes and Technologies”. In: *Journal of Clinical Medicine* 9.6 (2020). ISSN: 2077-0383. DOI: 10.3390/jcm9061648. URL: https://www.mdpi.com/2077-0383/9/6/1648.

[33] W. Marlicz, X. Ren, A. Robertson, et al. “Frontiers of Robotic Gastroscopy: A Comprehensive Review of Robotic Gastroscopes and Technologies”. en. In: *Cancers (Basel)* 12.10 (Sept. 2020).

[34] I. Boškoski, B. Orlandini, L. G. Papparella, et al. “Robotics and Artificial Intelligence in Gastrointestinal Endoscopy: Updated Review of the Literature and State of the Art”. In: *Current Robotics Reports* 2.1 (Mar. 2021), pp. 43–54. ISSN: 2662-4087. DOI: 10.1007/s43154-020-00040-3. URL: https://doi.org/10.1007/s43154-020-00040-3.

[35] F. Carpi, N. Kastelein, M. Talcott, et al. “Magnetically Controllable Gastrointestinal Steering of Video Capsules”. en. In: *IEEE Trans Biomed Eng* 58.2 (Oct. 2010), pp. 231–234.

[36] J. W. Martin, B. Scaglioni, J. C. Norton, et al. “Enabling the Future of Colonoscopy with Intelligent and Autonomous Magnetic Manipulation”. In: *Nature Machine Intelligence* 2.10 (Oct. 2020), pp. 595–606. ISSN: 2522-5839. DOI: 10.1038/s42256-020-00231-9. URL: https://doi.org/10.1038/s42256-020-00231-9.

[37] I. De Falco, G. Tortora, P. Dario, et al. “An Integrated System for Wireless Capsule Endoscopy in a Liquid-Distended Stomach”. In: *IEEE Transactions on Biomedical Engineering* 61.3 (2014), pp. 794–804. DOI: 10.1109/TBME.2013.2290018.

[38] H. Liang, Y. Guan, Z. Xiao, et al. “A Screw Propelling Capsule Robot”. In: *2011 IEEE International Conference on Information and Automation*. 2011, pp. 786–791. DOI: 10.1109/ICINFA.2011.5949101.

[39] S. B. and A. P. “Recent Developments in Wireless Capsule Endoscopy Imaging: Compression and Summarization Techniques”. In: *Computers in Biology and Medicine* 149 (2022), p. 106087. ISSN: 0010-4825. DOI: https://doi.org/10.1016/j.compbiomed.2022.106087. URL: https://www.sciencedirect.com/science/article/pii/S0010482522007958.

[40] T. Takamatsu, Y. Endo, R. Fukushima, et al. “Robotic Endoscope with Double-Balloon and Double-Bend Tube for Colonoscopy”. In: *Scientific Reports* 13.1 (June 2023), p. 10494. ISSN: 2045-2322. DOI: 10.1038/s41598-023-37566-3. URL: https://doi.org/10.1038/s41598-023-37566-3.

[41] A. Sahafi, Y. Wang, C. L. M. Rasmussen, et al. “Edge Artificial Intelligence Wireless Video Capsule Endoscopy”. In: *Scientific Reports* 12.1 (Aug. 2022), p. 13723. ISSN: 2045-2322. DOI: 10.1038/s41598-022-17502-7. URL: https://doi.org/10.1038/s41598-022-17502-7.

[42] G. Ciuti, R. Caliò, D. Camboni, et al. “Frontiers of Robotic Endoscopic Capsules: A Review”. In: *Journal of Micro-Bio Robotics* 11.1 (June 2016), pp. 1–18. ISSN: 2194-6426. DOI: 10.1007/s12213-016-0087-x. URL: https://doi.org/10.1007/s12213-016-0087-x.

[43] L. Manfredi. “Endorobots for Colonoscopy: Design Challenges and Available Technologies”. In: *Frontiers in Robotics and AI* 8 (2021), p. 209. ISSN: 2296-9144. DOI: 10.3389/frobt.2021.705454. URL: https://www.frontiersin.org/article/10.3389/frobt.2021.705454.

[44] X. Yang, J. F. Lovell, and Y. Zhang. “Ingestible Contrast Agents for Gastrointestinal Imaging”. In: *ChemBioChem* 20.4 (2019), pp. 462–473. DOI: https://doi.org/10.1002/cbic.201800589. URL: https://chemistry-europe.onlinelibrary.wiley.com/doi/abs/10.1002/cbic.201800589.

[45] M. A. Bettmann, P. D. Bourdillon, W. H. Barry, et al. “Contrast Agents for Cardiac Angiography: Effects of a Nonionic Agent vs. a Standard Ionic Agent.” In: *Radiology* 153.3 (1984). PMID: 6387783, pp. 583–587. DOI: 10.1148/radiology.153.3.6387783. URL: https://doi.org/10.1148/radiology.153.3.6387783.

[46] O. Erin, M. Boyvat, M. E. Tiryaki, et al. “Magnetic Resonance Imaging System–Driven Medical Robotics”. In: *Advanced Intelligent Systems* 2.2 (2020), p. 1900110. DOI: https://doi.org/10.1002/aisy.201900110. URL: https://onlinelibrary.wiley.com/doi/abs/10.1002/aisy.201900110.

[47] D. Blero and J. Devière. “Endoscopic Complications—Avoidance and Management”. In: *Nature Reviews Gastroenterology & Hepatology* 9.3 (Mar. 2012), pp. 162–172. ISSN: 1759-5053. DOI: 10.1038/nrgastro.2012.3. URL: https://doi.org/10.1038/nrgastro.2012.3.

[48] J. Striegel, R. Jakobs, J. Van Dam, et al. “Determining Scope Position during Colonoscopy without Use of Ionizing Radiation or Magnetic Imaging: The Enhanced Mapping Ability of the NeoGuide Endoscopy System”. In: *Surgical Endoscopy* 25.2 (Feb. 2011), pp. 636–640. ISSN: 1432-2218. DOI: 10.1007/s00464-010-1245-1. URL: https://doi.org/10.1007/s00464-010-1245-1.

[49] N. Gluck, A. Melhem, Z. Halpern, et al. “A Novel Self-propelled Disposable Colonoscope is Effective for Colonoscopy in Humans (with Video)”. In: *Gastrointestinal Endoscopy* 83.5 (2016), 998–1004.e1. ISSN: 0016-5107. DOI: https://doi.org/10.1016/j.gie.2015.08.083.

[50] J. Pfeffer, R. Grinshpon, D. Rex, et al. “The Aer-O-Scope: Proof of the Concept of a Pneumatic, Skill-Independent, Self-Propelling, Self-Navigating Colonoscope in a Pig Model”. In: *Endoscopy* 38.2 (2006), pp. 144–148. DOI: 10.1055/s-2006-925089.

[51] K. Siau, N. D. Hawkes, and P. Dunckley. “Training in Endoscopy”. In: *Current Treatment Options in Gastroenterology* 16.3 (Sept. 2018), pp. 345–361. ISSN: 1534-309X. DOI: 10.1007/s11938-018-0191-1. URL: https://doi.org/10.1007/s11938-018-0191-1.

[52] S. Larsen, A. Kalloo, and S. Hutfless. “The Hidden Cost of Colonoscopy Including Cost of Reprocessing and Infection Rate: The Implications for Disposable Colonoscopes”. In: *Gut* 69.2 (2020), pp. 197–200. ISSN: 0017-5749. DOI: 10.1136/gutjnl-2019-319108. URL: https://gut.bmj.com/content/69/2/197.

[53] M. Ciocîrlan. “Low-cost Disposable Endoscope: Pros and Cons”. EN. In: *Endosc Int Open* 07.09 (Aug. 2019), E1184–E1186. ISSN: 2364-3722. DOI: 10.1055/a-0959-6003. URL: https://doi.org/10.1055/a-0959-6003.

[54] X. Luo, K. Mori, and T. M. Peters. “Advanced Endoscopic Navigation: Surgical Big Data, Methodology, and Applications”. en. In: *Annu Rev Biomed Eng* 20 (Mar. 2018), pp. 221–251.

[55] N. van der Stap, E. D. Rozeboom, H. J. M. Pullens, et al. “Feasibility of Automated Target Centralization in Colonoscopy”. In: *International Journal of Computer Assisted Radiology and Surgery* 11.3 (Mar. 2016), pp. 457–465. ISSN: 1861-6429. DOI: 10.1007/s11548-015-1301-3. URL: https://doi.org/10.1007/s11548-015-1301-3.

[56] N. van der Stap, C. H. Slump, I. A. M. J. Broeders, et al. “Image-Based Navigation for a Robotized Flexible Endoscope”. In: *Computer-Assisted and Robotic Endoscopy*. Ed. by X. Luo, T. Reichl, D. Mirota, et al. Cham: Springer International Publishing, 2014, pp. 77–87. ISBN: 978-3-319-13410-9.

[57] H. J. M. Pullens, N. van der Stap, E. D. Rozeboom, et al. “Colonoscopy with Robotic Steering and Automated Lumen Centralization: A Feasibility Study in a Colon Model”. In: *Endoscopy* 48.3 (2016), pp. 286–290. DOI: 10.1055/s-0034-1392550.

[58] H. J. Pullens, N. Van Der Stap, E. D. Rozeboom, et al. “Colonoscopy with Robotic Steering and Automated Lumen Centralization Compared with Conventional Colonoscopy: Results of a Randomized In Vitro Pilot Study”. In: *Gastrointestinal Endoscopy* 81.5, Supplement (2015). DDW 2015 ASGE Program and Abstracts, AB326. ISSN: 0016-5107. DOI: https://doi.org/10.1016/j.gie.2015.03.1451. URL: https://www.sciencedirect.com/science/article/pii/S0016510715016740.

[59] G. Robinson and J. Davies. “Continuum Robots - A State of the Art”. In: *Proceedings 1999 IEEE International Conference on Robotics and Automation (Cat. No.99CH36288C)*. Vol. 4. 1999, 2849–2854 vol.4. DOI: 10.1109/ROBOT.1999.774029.

[60] Z. Li, L. Wu, H. Ren, et al. “Kinematic Comparison of Surgical Tendon-Driven Manipulators and Concentric Tube Manipulators”. In: *Mechanism and Machine Theory* 107 (2017), pp. 148–165. ISSN: 0094-114X. DOI: https://doi.org/10.1016/j.mechmachtheory.2016.09.018. URL: https://www.sciencedirect.com/science/article/pii/S0094114X16302580.

[61] S. Li and G. Hao. “Current Trends and Prospects in Compliant Continuum Robots: A Survey”. In: *Actuators* 10.7 (2021). ISSN: 2076-0825. DOI: 10.3390/act10070145. URL: https://www.mdpi.com/2076-0825/10/7/145.

[62] M. Russo, S. M. H. Sadati, X. Dong, et al. “Continuum Robots: An Overview”. In: *Advanced Intelligent Systems* 5.5 (2023), p. 2200367. DOI: https://doi.org/10.1002/aisy.202200367. URL: https://onlinelibrary.wiley.com/doi/abs/10.1002/aisy.202200367.

[63] M. T. Chikhaoui and J. Burgner-Kahrs. “Control of Continuum Robots for Medical Applications: State of the Art”. In: *ACTUATOR 2018; 16th International Conference on New Actuators*. 2018, pp. 1–11.

[64] P. E. Dupont, B. J. Nelson, M. Goldfarb, et al. “A Decade Retrospective of Medical Robotics Research from 2010 to 2020”. In: *Science Robotics* 6.60 (2021), eabi8017. DOI: 10.1126/scirobotics.abi8017. URL: https://www.science.org/doi/abs/10.1126/scirobotics.abi8017.

[65] A. Pistone, D. Ludovico, L. De Mari Casareto Dal Verme, et al. “Modelling and Control of Manipulators for Inspection and Maintenance in Challenging Environments: A Literature Review”. In: *Annual Reviews in Control* 57 (2024), p. 100949. ISSN: 1367-5788. DOI: https://doi.org/10.1016/j.arcontrol.2024.100949. URL: https://www.sciencedirect.com/science/article/pii/S136757882400018X.

[66] A. Yeshmukhametov, K. Koganezawa, Y. Yamamoto, et al. “Development of Continuum Robot Arm and Gripper for Harvesting Cherry Tomatoes”. In: *Applied Sciences* 12.14 (2022). ISSN: 2076-3417. DOI: 10.3390/app12146922. URL: https://www.mdpi.com/2076-3417/12/14/6922.

[67] M. Russo. "Continuum Robots for Space Applications". In: *Design Advances in Aerospace Robotics*. Ed. by M. Ceccarelli, L. Santo, M. Paoloni, et al. Cham: Springer Nature Switzerland, 2023, pp. 129–139. ISBN: 978-3-031-28447-2.

[68] J. L. Sitler and L. Wang. "A Modular Open-Source Continuum Manipulator for Underwater Remotely Operated Vehicles". In: *Journal of Mechanisms and Robotics* 14.6 (Apr. 2022), p. 060906. ISSN: 1942-4302. DOI: 10.1115/1.4054309. URL: https://doi.org/10.1115/1.4054309.

[69] Y. Chen, B. Wu, J. Jin, et al. "A Variable Curvature Model for Multi-Backbone Continuum Robots to Account for Inter-Segment Coupling and External Disturbance". In: *IEEE Robotics and Automation Letters* 6.2 (2021), pp. 1590–1597. DOI: 10.1109/LRA.2021.3058925.

[70] B. He, Z. Wang, Q. Li, et al. "An Analytic Method for the Kinematics and Dynamics of a Multiple-Backbone Continuum Robot". In: *International Journal of Advanced Robotic Systems* 10.1 (2013), p. 84. DOI: 10.5772/54051. URL: https://doi.org/10.5772/54051.

[71] H. Alfalahi, F. Renda, and C. Stefanini. "Concentric Tube Robots for Minimally Invasive Surgery: Current Applications and Future Opportunities". In: *IEEE Transactions on Medical Robotics and Bionics* 2.3 (2020), pp. 410–424. DOI: 10.1109/TMRB.2020.3000899.

[72] Z. Mitros, S. H. Sadati, R. Henry, et al. "From Theoretical Work to Clinical Translation: Progress in Concentric Tube Robots". In: *Annual Review of Control, Robotics, and Autonomous Systems* 5.1 (2022), pp. 335–359. DOI: 10.1146/annurev-control-042920-014147. URL: https://doi.org/10.1146/annurev-control-042920-014147.

[73] M. Babaiasl, F. Yang, and J. P. Swensen. "Robotic Needle Steering: State-of-the-art and Research Challenges". In: *Intelligent Service Robotics* 15.5 (Oct. 2022), pp. 679–711. DOI: 10.1007/s11370-022-00446-2. URL: https://doi.org/10.1007/s11370-022-00446-2.

[74] G. Pittiglio, L. Barducci, J. W. Martin, et al. "Magnetic Levitation for Soft-Tethered Capsule Colonoscopy Actuated with a Single Permanent Magnet: A Dynamic Control Approach". In: *IEEE Robotics and Automation Letters* 4.2 (2019), pp. 1224–1231. ISSN: 23773766. DOI: 10.1109/LRA.2019.2894907.

[75] F. Ullrich. "Assistive Robots for Minimally Invasive Ophthalmic Surgery". PhD thesis. ETH Zurich, 2016.

[76] Z. Yang, H. Yang, Y. Cao, et al. "Magnetically Actuated Continuum Medical Robots: A Review". In: *Advanced Intelligent Systems* n/a.n/a (2023), p. 2200416. DOI: https://doi.org/10.1002/aisy.202200416. URL: https://onlinelibrary.wiley.com/doi/abs/10.1002/aisy.202200416.

[77] H. Su, X. Hou, X. Zhang, et al. "Pneumatic Soft Robots: Challenges and Benefits". In: *Actuators* 11.3 (2022). ISSN: 2076-0825. DOI: 10.3390/act11030092. URL: https://www.mdpi.com/2076-0825/11/3/92.

[78] N. Garbin, L. Wang, J. Chandler, et al. "A Disposable Continuum Endoscope using Piston-driven Parallel Bellow Actuator". In: *2018 International Symposium on Medical Robotics (ISMR)*. 2018, pp. 1–6. DOI: 10.1109/ISMR.2018.8333287.

[79] N. Garbin, L. Wang, J. H. Chandler, et al. "Dual-Continuum Design Approach for Intuitive and Low-Cost Upper Gastrointestinal Endoscopy". In: *IEEE Transactions on Biomedical Engineering* 66.7 (2019), pp. 1963–1974. DOI: 10.1109/TBME.2018.2881717.

[80] T. da Veiga, J. H. Chandler, P. Lloyd, et al. "Challenges of Continuum Robots in Clinical Context: A Review". In: *Progress in Biomedical Engineering* 2.3 (July 2020), p. 032003. DOI: 10.1088/2516-1091/ab9f41. URL: https://dx.doi.org/10.1088/2516-1091/ab9f41.

[81] M. A. Khan, S. Shaik, M. H. Tariq, et al. "McKibben Pneumatic Artificial Muscle Robot Actuators - A Review". In: *2023 International Conference on Robotics and Automation in Industry (ICRAI)*. 2023, pp. 1–6. DOI: 10.1109/ICRAI57502.2023.10089581.

[82] B. Jamil, N. Oh, J.-G. Lee, et al. “A Review and Comparison of Linear Pneumatic Artificial Muscles”. In: *International Journal of Precision Engineering and Manufacturing-Green Technology* 11.1 (Jan. 2024), pp. 277–289. ISSN: 2198-0810. DOI: 10.1007/s40684-023-00531-6. URL: https://doi.org/10.1007/s40684-023-00531-6.

[83] E. W. Hawkes, L. H. Blumenschein, J. D. Greer, et al. “A Soft Robot that Navigates its Environment through Growth”. In: *Science Robotics* 2.8 (2017), eaan3028. DOI: 10.1126/scirobotics.aan3028. URL: https://www.science.org/doi/abs/10.1126/scirobotics.aan3028.

[84] M. M. Coad, L. H. Blumenschein, S. Cutler, et al. “Vine Robots”. In: *IEEE Robotics & Automation Magazine* 27.3 (2020), pp. 120–132. DOI: 10.1109/MRA.2019.2947538.

[85] S. A. Coleman, M. Pakleppa, and A. Cuschieri. “Hydro-Jet Propelled Colonoscopy: Proof of Concept in a Phantom Colon”. In: *Surgical Endoscopy* 35.2 (2021), pp. 989–995. DOI: 10.1007/s00464-020-08089-z.

[86] F. Campisano, A. A. Remirez, C. A. Landewee, et al. “Teleoperation and Contact Detection of a Waterjet-Actuated Soft Continuum Manipulator for Low-Cost Gastroscopy”. In: *IEEE Robotics and Automation Letters* 5.4 (2020), pp. 6427–6434. DOI: 10.1109/LRA.2020.3013900.

[87] M. A. Mandolino, Y. Goergen, P. Motzki, et al. “Design and Characterization of a Fully Integrated Continuum Robot Actuated by Shape Memory Alloy Wires”. In: *2022 IEEE 17th International Conference on Advanced Motion Control (AMC)*. 2022, pp. 6–11. DOI: 10.1109/AMC51637.2022.9729267.

[88] D. J. S. Ruth, J.-W. Sohn, K. Dhanalakshmi, et al. “Control Aspects of Shape Memory Alloys in Robotics Applications: A Review over the Last Decade”. In: *Sensors* 22.13 (2022). ISSN: 1424-8220. DOI: 10.3390/s22134860. URL: https://www.mdpi.com/1424-8220/22/13/4860.

[89] R. Cortez, M. A. Sandoval-Chileño, N. Lozada-Castillo, et al. “Snake Robot with Motion Based on Shape Memory Alloy Spring-Shaped Actuators”. In: *Biomimetics* 9.3 (2024). ISSN: 2313-7673. DOI: 10.3390/biomimetics9030180. URL: https://www.mdpi.com/2313-7673/9/3/180.

[90] Y. Xia, Y. He, F. Zhang, et al. “A Review of Shape Memory Polymers and Composites: Mechanisms, Materials, and Applications”. In: *Advanced Materials* 33.6 (2021), p. 2000713. DOI: https://doi.org/10.1002/adma.202000713. URL: https://onlinelibrary.wiley.com/doi/abs/10.1002/adma.202000713.

[91] Q. Jacquemin, Q. Sun, D. Thuau, et al. “Design and Control of a New Electrostrictive Polymer Based Continuum Actuator for Endoscopic Robot”. In: *Journal of Intelligent Material Systems and Structures* 34.12 (2023), pp. 1355–1365. DOI: 10.1177/1045389X221142090. URL: https://doi.org/10.1177/1045389X221142090.

[92] G. Stoychev, A. Kirillova, and L. Ionov. “Light-Responsive Shape-Changing Polymers”. In: *Advanced Optical Materials* 7.16 (2019), p. 1900067. DOI: https://doi.org/10.1002/adom.201900067. URL: https://onlinelibrary.wiley.com/doi/abs/10.1002/adom.201900067.

[93] M. Pan, C. Yuan, X. Liang, et al. “Triboelectric and Piezoelectric Nanogenerators for Future Soft Robots and Machines”. In: *iScience* 23.11 (2020), p. 101682. ISSN: 2589-0042. DOI: https://doi.org/10.1016/j.isci.2020.101682. URL: https://www.sciencedirect.com/science/article/pii/S2589004220308749.

[94] K.-W. Kwok, K. Hung Tsoi, V. Vitiello, et al. “Dimensionality Reduction in Controlling Articulated Snake Robot for Endoscopy Under Dynamic Active Constraints”. In: *IEEE Transactions on Robotics* 29.1 (2013), pp. 15–31. DOI: 10.1109/TRO.2012.2226382.

[95] L. Yin, S. Wang, and S. Zuo. “Water-Jet Outer Sheath with Braided Shape Memory Polymer Tubes for Upper Gastrointestinal Tract Screening”. In: *The International Journal of Medical Robotics and Computer Assisted Surgery* 14.6 (2018). e1944 RCS-18-0032.R2, e1944. DOI: https://doi.org/10.1002/rcs.1944. URL: https://onlinelibrary.wiley.com/doi/abs/10.1002/rcs.1944.

[96] M. Langer, E. Amanov, and J. Burgner-Kahrs. “Stiffening Sheaths for Continuum Robots”. In: *Soft Robotics* 5.3 (2018). PMID: 29498586, pp. 291–303. DOI: 10.1089/soro.2017.0060. URL: https://doi.org/10.1089/soro.2017.0060.

[97] Y. Fan, D. Liu, and L. Ye. “A Novel Continuum Robot With Stiffness Variation Capability Using Layer Jamming: Design, Modeling, and Validation”. In: *IEEE Access* 10 (2022), pp. 130253–130263. DOI: 10.1109/ACCESS.2022.3228775.

[98] E. Amanov, T.-D. Nguyen, and J. Burgner-Kahrs. “Tendon-Driven Continuum Robots with Extensible Sections—A Model-Based Evaluation of Path-Following Motions”. In: *The International Journal of Robotics Research* 40.1 (2021), pp. 7–23. DOI: 10.1177/0278364919886047. URL: https://doi.org/10.1177/0278364919886047.

[99] E. Amanov, J. Granna, and J. Burgner-Kahrs. “Toward Improving Path Following Motion: Hybrid Continuum Robot Design”. In: *2017 IEEE International Conference on Robotics and Automation (ICRA)*. 2017, pp. 4666–4672. DOI: 10.1109/ICRA.2017.7989542.

[100] N. Fischer, M. Becher, L. Höltge, et al. “A Self-Assembling Extendable Tendon-Driven Continuum Robot With Variable Length”. In: *IEEE Robotics and Automation Letters* 8.12 (2023), pp. 8518–8524. DOI: 10.1109/LRA.2023.3325781.

[101] J. Starke, E. Amanov, M. T. Chikhaoui, et al. “On the Merits of Helical Tendon Routing in Continuum Robots”. In: *2017 IEEE/RSJ International Conference on Intelligent Robots and Systems (IROS)*. 2017, pp. 6470–6476. DOI: 10.1109/IROS.2017.8206554.

[102] R. M. Grassmann, P. Rao, Q. Peyron, et al. “FAS—A Fully Actuated Segment for Tendon-Driven Continuum Robots”. In: *Frontiers in Robotics and AI* 9 (2022). ISSN: 2296-9144. DOI: 10.3389/frobt.2022.873446. URL: https://www.frontiersin.org/articles/10.3389/frobt.2022.873446.

[103] T. Ginoya, Y. Maddahi, and K. Zareinia. “A Historical Review of Medical Robotic Platforms”. In: *Journal of Robotics* 2021 (Jan. 2021), p. 6640031. ISSN: 1687-9600. DOI: 10.1155/2021/6640031. URL: https://doi.org/10.1155/2021/6640031.

[104] C. Ren and D. Sun. “Robot-Assisted Single-Port Laparoscopic Bilateral Ovarian Cystectomy Using the Shurui(R) System: A Case Report”. In: *Intelligent Surgery* 3 (2022), pp. 9–13. ISSN: 2666-6766. DOI: https://doi.org/10.1016/j.isurg.2022.06.001. URL: https://www.sciencedirect.com/science/article/pii/S2666676622000497.

[105] C. F. Graetzel, A. Sheehy, and D. P. Noonan. “Robotic Bronchoscopy Drive Mode of the Auris Monarch Platform”. In: *2019 International Conference on Robotics and Automation (ICRA)*. 2019, pp. 3895–3901. DOI: 10.1109/ICRA.2019.8793704.

[106] J. Y. Y. Wong and K. Y. Ho. “Robotics for Advanced Therapeutic Colonoscopy”. In: *Clin Endosc* 51.6 (2018), pp. 552–557. DOI: 10.5946/ce.2018.089. URL: http://www.e-ce.org/journal/view.php?number=7134.

[107] A. Eickhoff, J. van Dam, R. Jakobs, et al. “Computer-Assisted Colonoscopy (the NeoGuide Endoscopy System): Results of the First Human Clinical Trial (“PACE study”)”. en. In: *Am J Gastroenterol* 102.2 (Dec. 2006), pp. 261–266.

[108] D. A. Troncoso, J. A. Robles-Linares, M. Russo, et al. “A Continuum Robot for Remote Applications: From Industrial to Medical Surgery With Slender Continuum Robots”. In: *IEEE Robotics & Automation Magazine* 30.3 (2023), pp. 94–105. DOI: 10.1109/MRA.2022.3223220.

[109] A. Yeshmukhametov, K. Koganezawa, and Y. Yamamoto. “Design and Kinematics of Cable-Driven Continuum Robot Arm with Universal Joint Backbone”. In: *2018 IEEE International Conference on Robotics and Biomimetics (ROBIO)*. 2018, pp. 2444–2449. DOI: 10.1109/ROBIO.2018.8665186.

[110] A. Yeshmukhametov, K. Koganezawa, and Y. Yamamoto. “A Novel Discrete Wire-Driven Continuum Robot Arm with Passive Sliding Disc: Design, Kinematics and Passive Tension Control”. In: *Robotics* 8.3 (2019). ISSN: 2218-6581. DOI: 10.3390/robotics8030051. URL: https://www.mdpi.com/2218-6581/8/3/51.

[111] M.-o. Kim, U. Jeong, D. Choi, et al. “Tendon-Driven Continuum Robot Systems with only A Single Motor and A Radius-Changing Pulley”. In: *2020 20th International Conference on Control, Automation and Systems (ICCAS)*. 2020, pp. 945–949. DOI: 10.23919/ICCAS50221.2020.9268288.

[112] M. Li, R. Kang, S. Geng, et al. “Design and Control of a Tendon-Driven Continuum Robot”. In: *Transactions of the Institute of Measurement and Control* 40.11 (2018), pp. 3263–3272. DOI: 10.1177/0142331216685607. URL: https://doi.org/10.1177/0142331216685607.

[113] W. Hong, F. Feng, L. Xie, et al. “A Two-Segment Continuum Robot With Piecewise Stiffness for Maxillary Sinus Surgery and Its Decoupling Method”. In: *IEEE/ASME Transactions on Mechatronics* 27.6 (2022), pp. 4440–4450. DOI: 10.1109/TMECH.2022.3157041.

[114] Y. Cao, Z. Liu, Z. Liu, et al. “Design and Path Tracking Control of a Continuum Robot for Maxillary Sinus Surgery”. In: *International Journal of Computer Assisted Radiology and Surgery* 18.4 (Apr. 2023), pp. 753–761. ISSN: 1861-6429. DOI: 10.1007/s11548-022-02820-y. URL: https://doi.org/10.1007/s11548-022-02820-y.

[115] X. Zhang, W. Li, P. W. Y. Chiu, et al. “A Novel Flexible Robotic Endoscope with Constrained Tendon-Driven Continuum Mechanism”. In: *IEEE Robotics and Automation Letters* 5.2 (2020), pp. 1366–1372. DOI: 10.1109/LRA.2020.2967737.

[116] X. Dong, D. Axinte, D. Palmer, et al. “Development of a Slender Continuum Robotic System for On-wing Inspection/Repair of Gas Turbine Engines”. In: *Robotics and Computer-Integrated Manufacturing* 44 (2017), pp. 218–229. ISSN: 0736-5845. DOI: https://doi.org/10.1016/j.rcim.2016.09.004. URL: https://www.sciencedirect.com/science/article/pii/S0736584516300801.

[117] T.-D. Nguyen and J. Burgner-Kahrs. “A Tendon-Driven Continuum Robot with Extensible Sections”. In: *2015 IEEE/RSJ International Conference on Intelligent Robots and Systems (IROS)*. 2015, pp. 2130–2135. DOI: 10.1109/IROS.2015.7353661.

[118] Y. Lei, Y. Sugahara, and Y. Takeda. “Design and Inverse Kinematics of a Novel Tendon-Driven Continuum Manipulator Capable of Twisting Motion”. In: *Advances in Robot Kinematics 2022*. Ed. by O. Altuzarra and A. Kecskeméthy. Cham: Springer International Publishing, 2022, pp. 228–236. ISBN: 978-3-031-08140-8.

[119] K. Kume, N. Sakai, and T. Ueda. “Development of a Novel Gastrointestinal Endoscopic Robot Enabling Complete Remote Control of All Operations: Endoscopic Therapeutic Robot System (ETRS)”. In: *Gastroenterology Research and Practice* 2019 (2019). ISSN: 1687630X. DOI: 10.1155/2019/6909547.

[120] K. Kume, T. Kuroki, M. Shingai, et al. “Endoscopic Submucosal Dissection Using the Endoscopic Operation Robot”. en. In: *Endoscopy* 44.S02 (Oct. 2012), pp. 399–400. ISSN: 0013-726X. DOI: 10.1055/s-0032-1310251. URL: https://doi.org/10.1055/s-0032-1310251.

[121] T. Liang, C. Zhang, Y. Wang, et al. “A Novel Miniature Flexible Robotic System for Endoscopic Mucosal Dissection: An Animal Experimental Study”. In: *Journal of Robotic Surgery* 18.1 (Jan. 2024), p. 17. ISSN: 1863-2491. DOI: 10.1007/s11701-023-01793-7. URL: https://doi.org/10.1007/s11701-023-01793-7.

[122] P. Rao, Q. Peyron, S. Lilge, et al. "How to Model Tendon-Driven Continuum Robots and Benchmark Modelling Performance". In: *Frontiers in Robotics and AI* 7.February (2021), pp. 1–20. ISSN: 22969144. DOI: 10.3389/frobt.2020.630245.

[123] Z. Chen, F. Renda, A. L. Gall, et al. "Data-Driven Methods Applied to Soft Robot Modeling and Control: A Review". In: *IEEE Transactions on Automation Science and Engineering* (2024), pp. 1–16. DOI: 10.1109/TASE.2024.3377291.

[124] I. Robert J. Webster and B. A. Jones. "Design and Kinematic Modeling of Constant Curvature Continuum Robots: A Review". In: *The International Journal of Robotics Research* 29.13 (2010), pp. 1661–1683. DOI: 10.1177/0278364910368147. URL: https://doi.org/10.1177/0278364910368147.

[125] J. Zhang, Q. Fang, P. Xiang, et al. "A Survey on Design, Actuation, Modeling, and Control of Continuum Robot". In: *Cyborg and Bionic Systems* 2022 (2022). DOI: 10.34133/2022/9754697. URL: https://spj.science.org/doi/abs/10.34133/2022/9754697.

[126] X. Wang, Y. Li, and K.-W. Kwok. "A Survey for Machine Learning-Based Control of Continuum Robots". In: *Frontiers in Robotics and AI* 8 (2021). ISSN: 2296-9144. DOI: 10.3389/frobt.2021.730330. URL: https://www.frontiersin.org/articles/10.3389/frobt.2021.730330.

[127] F. Janabi-Sharifi, A. Jalali, and I. D. Walker. "Cosserat Rod-Based Dynamic Modeling of Tendon-Driven Continuum Robots: A Tutorial". In: *IEEE Access* 9 (2021), pp. 68703–68719. DOI: 10.1109/ACCESS.2021.3077186.

[128] R. M. Grassmann, C. Shentu, T. Hamoda, et al. "Open Continuum Robotics – One Actuation Module to Create them All". In: *Frontiers in Robotics and AI* 11 (2024). ISSN: 2296-9144. DOI: 10.3389/frobt.2024.1272403. URL: https://www.frontiersin.org/articles/10.3389/frobt.2024.1272403.

[129] L. Fasel, N. Gerig, P. C. Cattin, et al. "Tendon Force Control Evaluation for an Endoscope with Series Elastic Actuation". In: *New Trends in Medical and Service Robotics*. Ed. by G. Rauter, P. C. Cattin, A. Zam, et al. Cham: Springer International Publishing, 2021, pp. 118–126. ISBN: 978-3-030-58104-6.

[130] C. Shi, X. Luo, P. Qi, et al. "Shape Sensing Techniques for Continuum Robots in Minimally Invasive Surgery: A Survey". In: *IEEE Transactions on Biomedical Engineering* 64.8 (2017), pp. 1665–1678. DOI: 10.1109/TBME.2016.2622361.

[131] S. Sefati, C. Gao, I. Iordachita, et al. "Data-Driven Shape Sensing of a Surgical Continuum Manipulator Using an Uncalibrated Fiber Bragg Grating Sensor". In: *IEEE Sensors Journal* 21.3 (2021), pp. 3066–3076. DOI: 10.1109/JSEN.2020.3028208.

[132] G. Chen, M. T. Pham, and T. Redarce. "Sensor-Based Guidance Control of a Continuum Robot for a Semi-Autonomous Colonoscopy". In: *Robotics and Autonomous Systems* 57.6-7 (2009), pp. 712–722. ISSN: 09218890. DOI: 10.1016/j.robot.2008.11.001.

[133] Y. Liu, H. Xie, H. Wang, et al. "Distance Control of Soft Robot Using Proximity Sensor for Beating Heart Surgery". In: *2016 IEEE/SICE International Symposium on System Integration (SII)*. 2016, pp. 403–408. DOI: 10.1109/SII.2016.7844032.

[134] G. A. Giacoppo, L. Schunter, and P. P. Pott. "Impact of the Fiber Cutting Angle on Fiber Optic Proximity Sensors in Endoscopy". In: *Current Directions in Biomedical Engineering* 8.2 (2022), pp. 37–40. DOI: 10.1515/cdbme-2022-1011. URL: https://doi.org/10.1515/cdbme-2022-1011.

[135] A. A. Nazari, K. Zareinia, and F. Janabi-Sharifi. "Visual Servoing of Continuum Robots: Methods, Challenges, and Prospects". en. In: *Int J Med Robot* 18.3 (Mar. 2022), e2384. DOI: 10.1002/rcs.2384.

[136] Y. Lu, R. Wei, B. Li, et al. “Autonomous Intelligent Navigation for Flexible Endoscopy Using Monocular Depth Guidance and 3-D Shape Planning”. In: *2023 IEEE International Conference on Robotics and Automation (ICRA)*. 2023, pp. 1–7. DOI: 10.1109/ICRA48891.2023.10161505.

[137] R. Reilink, S. Stramigioli, and S. Misra. “Image-Based Flexible Endoscope Steering”. In: *2010 IEEE/RSJ International Conference on Intelligent Robots and Systems*. 2010, pp. 2339–2344. DOI: 10.1109/IROS.2010.5652248.

[138] I. Abaspur Kazerouni, L. Fitzgerald, G. Dooly, et al. “A Survey of State-of-the-art on Visual SLAM”. In: *Expert Systems with Applications* 205 (2022), p. 117734. ISSN: 0957-4174. DOI: https://doi.org/10.1016/j.eswa.2022.117734. URL: https://www.sciencedirect.com/science/article/pii/S0957417422010156.

[139] C. Xie, T. Yao, J. Wang, et al. “Endoscope Localization and Gastrointestinal Feature Map Construction Based on Monocular SLAM Technology”. In: *Journal of Infection and Public Health* 13.9 (2020), pp. 1314–1321. ISSN: 1876-0341. DOI: https://doi.org/10.1016/j.jiph.2019.06.028. URL: https://www.sciencedirect.com/science/article/pii/S1876034119302321.

[140] A. Marmol, P. Corke, and T. Peynot. “ArthroSLAM: Multi-Sensor Robust Visual Localization for Minimally Invasive Orthopedic Surgery”. In: *2018 IEEE/RSJ International Conference on Intelligent Robots and Systems (IROS)*. 2018, pp. 3882–3889. DOI: 10.1109/IROS.2018.8593501.

[141] J. Zhao, Y. Luo, Q. Li, et al. “SPSVO: A Self-Supervised Surgical Perception Stereo Visual Odometer for Endoscopy”. In: *Robotica* 41.12 (2023), pp. 3724–3745. DOI: 10.1017/S026357472300125X.

[142] G. Dwyer, F. Chadebecq, M. T. Amo, et al. “A Continuum Robot and Control Interface for Surgical Assist in Fetoscopic Interventions”. In: *IEEE Robotics and Automation Letters* 2.3 (2017), pp. 1656–1663. DOI: 10.1109/LRA.2017.2679902.

[143] Z. Yang, S. Lin, R. Simon, et al. “Endoscope Localization and Dense Surgical Scene Reconstruction for Stereo Endoscopy by Unsupervised Optical Flow and Kanade-Lucas-Tomasi Tracking”. en. In: *Annu Int Conf IEEE Eng Med Biol Soc* 2022 (June 2022), pp. 4839–4842.

[144] S.-J. Nam, Y. J. Lim, J. H. Nam, et al. “3D Reconstruction of Small Bowel Lesions Using Stereo Camera-Based Capsule Endoscopy”. In: *Scientific Reports* 10.1 (Apr. 2020), p. 6025. ISSN: 2045-2322. DOI: 10.1038/s41598-020-62935-7. URL: https://doi.org/10.1038/s41598-020-62935-7.

[145] R. Richa, M. Balicki, R. Sznitman, et al. “Vision-Based Proximity Detection in Retinal Surgery”. en. In: *IEEE Trans Biomed Eng* 59.8 (June 2012), pp. 2291–2301.

[146] M. Antico, F. Sasazawa, L. Wu, et al. “Ultrasound Guidance in Minimally Invasive Robotic Procedures”. In: *Medical Image Analysis* 54 (2019), pp. 149–167. ISSN: 1361-8415. DOI: https://doi.org/10.1016/j.media.2019.01.002. URL: https://www.sciencedirect.com/science/article/pii/S1361841519300027.

[147] O. C. Mora, P. Zanne, L. Zorn, et al. “Steerable OCT Catheter for Real-Time Assistance during Teleoperated Endoscopic Treatment of Colorectal Cancer”. In: *Biomed. Opt. Express* 11.3 (Mar. 2020), pp. 1231–1243.

[148] V. Bințințan, A. Calborean, M. Mocan, et al. “New Inductive Proximity Sensor Platform for Precise Localization of Small Colorectal Tumors”. In: *Materials Science and Engineering: C* 106 (2020), p. 110146. ISSN: 0928-4931. DOI: https://doi.org/10.1016/j.msec.2019.110146. URL: https://www.sciencedirect.com/science/article/pii/S0928493118333861.

[149] M. Sakthivel, B. George, and M. Sivaprakasam. "A New Inductive Proximity Sensor Based Guiding Tool to Locate Metal Shrapnel During Surgery". In: *IEEE Transactions on Instrumentation and Measurement* 63.12 (2014), pp. 2940–2949. DOI: 10.1109/TIM.2014.2326767.

[150] C. Abah, A. L. Orekhov, G. L. H. Johnston, et al. "A Multi-Modal Sensor Array for Human–Robot Interaction and Confined Spaces Exploration Using Continuum Robots". In: *IEEE Sensors Journal* 22.4 (2022), pp. 3585–3594. DOI: 10.1109/JSEN.2021.3140002.

[151] J. Penne, K. Höller, M. Stürmer, et al. "Time-of-Flight 3-D Endoscopy". In: *Medical Image Computing and Computer-Assisted Intervention – MICCAI 2009*. Ed. by G.-Z. Yang, D. Hawkes, D. Rueckert, et al. Berlin, Heidelberg: Springer Berlin Heidelberg, 2009, pp. 467–474. ISBN: 978-3-642-04268-3.

[152] W. Wang, J. Wang, Y. Luo, et al. "A Survey on Force Sensing Techniques in Robot-Assisted Minimally Invasive Surgery". In: *IEEE Transactions on Haptics* 16.4 (2023), pp. 702–718. DOI: 10.1109/TOH.2023.3329172.

[153] G. G. Muscolo and P. Fiorini. "Force–Torque Sensors for Minimally Invasive Surgery Robotic Tools: An Overview". In: *IEEE Transactions on Medical Robotics and Bionics* 5.3 (2023), pp. 458–471. DOI: 10.1109/TMRB.2023.3261102.

[154] U. Seibold, B. Kübler, and G. Hirzinger. "Prototype of Instrument for Minimally Invasive Surgery with 6-Axis Force Sensing Capability". In: *Proceedings - IEEE International Conference on Robotics and Automation* 2005.April (2005), pp. 496–501. ISSN: 10504729. DOI: 10.1109/ROBOT.2005.1570167.

[155] B. Kuebler, U. Seibold, and G. Hirzinger. "Development of Actuated and Sensor Integrated Forceps for Minimally Invasive Robotic Surgery". In: *International Journal of Medical Robotics and Computer Assisted Surgery* 01.03 (2005), p. 96. ISSN: 1478-5951. DOI: 10.1581/mrcas.2005.010305.

[156] Y. Noh, E. L. Secco, S. Sareh, et al. "A Continuum Body Force Sensor Designed for Flexible Surgical Robotics Devices". In: *2014 36th Annual International Conference of the IEEE Engineering in Medicine and Biology Society*. 2014, pp. 3711–3714. DOI: 10.1109/EMBC.2014.6944429.

[157] P. Puangmali, H. Liu, L. D. Seneviratne, et al. "Miniature 3-Axis Distal Force Sensor for Minimally Invasive Surgical Palpation". In: *IEEE/ASME Transactions on Mechatronics* 17.4 (2012), pp. 646–656. DOI: 10.1109/TMECH.2011.2116033.

[158] P. Polygerinos, L. D. Seneviratne, R. Razavi, et al. "Triaxial Catheter-Tip Force Sensor for MRI-Guided Cardiac Procedures". In: *IEEE/ASME Transactions on Mechatronics* 18.1 (2013), pp. 386–396. DOI: 10.1109/TMECH.2011.2181405.

[159] Q. Liu, Y. Dai, M. Li, et al. "FBG-Based Sensorized Surgical Instrument for Force Measurement in Minimally Invasive Robotic Surgery". In: *IEEE Sensors Journal* 24.7 (2024), pp. 11450–11458. DOI: 10.1109/JSEN.2024.3365800.

[160] F. Khan, R. J. Roesthuis, and S. Misra. "Force Sensing in Continuum Manipulators Using Fiber Bragg Grating Sensors". In: *2017 IEEE/RSJ International Conference on Intelligent Robots and Systems (IROS)*. 2017, pp. 2531–2536. DOI: 10.1109/IROS.2017.8206073.

[161] R. Xu, A. Yurkewich, and R. V. Patel. "Curvature, Torsion, and Force Sensing in Continuum Robots Using Helically Wrapped FBG Sensors". In: *IEEE Robotics and Automation Letters* 1.2 (2016), pp. 1052–1059. DOI: 10.1109/LRA.2016.2530867.

[162] G. Fagogenis, M. Mencattelli, Z. Machaidze, et al. "Autonomous Robotic Intracardiac Catheter Navigation Using Haptic Vision". In: *Science Robotics* 4.29 (2019). ISSN: 24709476. DOI: 10.1126/scirobotics.aaw1977.

[163] V. Hacker and C. Sumereder. *Electrical engineering: Fundamentals*. De Gruyter Textbook. München ; De Gruyter Oldenbourg, 2020. URL: http://www.degruyter.com/books/9783110521115.

[164] N. I. of Standards and Technology. *Security Requirements for Cryptographic Modules*. Tech. rep. Federal Information Processing Standards Publications (FIPS PUBS) 140-2, Change Notice 2 December 03, 2002. Washington, D.C.: U.S. Department of Commerce, 2001. DOI: 10.6028/nist.fips.140-2.

[165] P. Hasgall, F. D. Gennaro, C. Baumgartner, et al. *Tissue Properties Database V4.1*. 2022. DOI: 10.13099/VIP21000-04-1. URL: https://itis.swiss/virtual-population/tissue-properties/downloads/database-v4-1/.

[166] H. Alagi, S. E. Navarro, M. Mende, et al. "A Versatile and Modular Capacitive Tactile Proximity Sensor". In: *2016 IEEE Haptics Symposium (HAPTICS)*. 2016, pp. 290–296. DOI: 10.1109/HAPTICS.2016.7463192.

[167] Y. Ye, C. Zhang, C. He, et al. "A Review on Applications of Capacitive Displacement Sensing for Capacitive Proximity Sensor". In: *IEEE Access* 8 (2020), pp. 45325–45342. DOI: 10.1109/ACCESS.2020.2977716.

[168] S. E. Navarro, S. Nagels, H. Alagi, et al. "A Model-Based Sensor Fusion Approach for Force and Shape Estimation in Soft Robotics". In: *IEEE Robotics and Automation Letters* 5.4 (2020), pp. 5621–5628. DOI: 10.1109/LRA.2020.3008120.

[169] S. E. Navarro, S. Mühlbacher-Karrer, H. Alagi, et al. "Proximity Perception in Human-Centered Robotics: A Survey on Sensing Systems and Applications". In: *IEEE Transactions on Robotics* 38.3 (2022), pp. 1599–1620. DOI: 10.1109/TRO.2021.3111786.

[170] H. Yang, B. Wu, X. Liu, et al. "A Closed-Loop Controller for a Continuum Surgical Manipulator Based on a Specially Designed Wrist Marker and Stereo Tracking". In: *2020 IEEE/ASME International Conference on Advanced Intelligent Mechatronics (AIM)*. 2020, pp. 335–340. DOI: 10.1109/AIM43001.2020.9158940.

[171] A. Rivadeneyra and J. A. López-Villanueva. "Recent Advances in Printed Capacitive Sensors". In: *Micromachines* 11.4 (2020). ISSN: 2072-666X. DOI: 10.3390/mi11040367. URL: https://www.mdpi.com/2072-666X/11/4/367.

[172] H. Alagi, S. Ergun, Y. Ding, et al. "Evaluation of On-Robot Capacitive Proximity Sensors with Collision Experiments for Human-Robot Collaboration". In: *2022 IElectric field imaging pre-touch for robotic graspersEEE/RSJ International Conference on Intelligent Robots and Systems (IROS)*. 2022, pp. 6716–6723. DOI: 10.1109/IROS47612.2022.9981490.

[173] S. Ergun, Y. Ding, H. Alagi, et al. "A Unified Perception Benchmark for Capacitive Proximity Sensing Towards Safe Human-Robot Collaboration (HRC)". In: *2021 IEEE International Conference on Robotics and Automation (ICRA)*. 2021, pp. 3634–3640. DOI: 10.1109/ICRA48506.2021.9561224.

[174] J. W. Booth, D. Shah, J. C. Case, et al. "OmniSkins: Robotic Skins that Turn Inanimate Objects into Multifunctional Robots". In: *Science Robotics* 3.22 (2018), eaat1853. DOI: 10.1126/scirobotics.aat1853. URL: https://www.science.org/doi/abs/10.1126/scirobotics.aat1853.

[175] S. Escaida Navarro, M. Schonert, B. Hein, et al. "6D Proximity Servoing for Preshaping and Haptic Exploration using Capacitive Tactile Proximity Sensors". In: *2014 IEEE/RSJ International Conference on Intelligent Robots and Systems*. 2014, pp. 7–14. DOI: 10.1109/IROS.2014.6942533.

[176] S. Escaida Navarro, S. Koch, and B. Hein. "3D Contour Following for a Cylindrical End-effector using Capacitive Proximity Sensors". In: *2016 IEEE/RSJ International Conference on Intelligent Robots and Systems (IROS)*. 2016, pp. 82–89. DOI: 10.1109/IROS.2016.7759038.

[177] Y. Ding, H. Zhang, and U. Thomas. “Capacitive Proximity Sensor Skin for Contactless Material Detection”. In: *2018 IEEE/RSJ International Conference on Intelligent Robots and Systems (IROS)*. 2018, pp. 7179–7184. DOI: 10.1109/IROS.2018.8594376.

[178] Y. Ding, F. Wilhelm, L. Faulhammer, et al. “With Proximity Servoing towards Safe Human-Robot-Interaction”. In: *2019 IEEE/RSJ International Conference on Intelligent Robots and Systems (IROS)*. 2019, pp. 4907–4912. DOI: 10.1109/IROS40897.2019.8968438.

[179] A. Saudabayev and H. A. Varol. “Sensors for Robotic Hands: A Survey of State of the Art”. In: *IEEE Access* 3 (2015), pp. 1765–1782. DOI: 10.1109/ACCESS.2015.2482543.

[180] W. Othman, Z.-H. A. Lai, C. Abril, et al. “Tactile Sensing for Minimally Invasive Surgery: Conventional Methods and Potential Emerging Tactile Technologies”. In: *Frontiers in Robotics and AI* 8 (2022). ISSN: 2296-9144. DOI: 10.3389/frobt.2021.705662. URL: https://www.frontiersin.org/articles/10.3389/frobt.2021.705662.

[181] U. Kim, D.-H. Lee, H. Moon, et al. “Design and Realization of Grasper-Integrated Force Sensor for Minimally Invasive Robotic Surgery”. In: *2014 IEEE/RSJ International Conference on Intelligent Robots and Systems*. 2014, pp. 4321–4326. DOI: 10.1109/IROS.2014.6943173.

[182] O. H. Paydar, C. R. Wottawa, R. E. Fan, et al. “Fabrication of a Thin-Film Capacitive Force Sensor Array for Tactile Feedback in Robotic Surgery”. In: *Proceedings of the Annual International Conference of the IEEE Engineering in Medicine and Biology Society, EMBS* (2012), pp. 2355–2358. ISSN: 1557170X. DOI: 10.1109/EMBC.2012.6346436.

[183] D.-H. Lee, U. Kim, H. Jung, et al. “A Capacitive-Type Novel Six-Axis Force/Torque Sensor for Robotic Applications”. In: *IEEE Sensors Journal* 16.8 (2016), pp. 2290–2299. DOI: 10.1109/JSEN.2015.2504267.

[184] Y. Dai, A. Abiri, S. Liu, et al. “Grasper Integrated Tri-Axial Force Sensor System for Robotic Minimally Invasive Surgery”. In: *2017 39th Annual International Conference of the IEEE Engineering in Medicine and Biology Society (EMBC)*. 2017, pp. 3936–3939. DOI: 10.1109/EMBC.2017.8037717.

[185] U. Kim, Y. B. Kim, D. Y. Seok, et al. “A New Type of Surgical Forceps Integrated with Three-Axial Force Sensor for Minimally Invasive Robotic Surgery”. In: *IEEE International Conference on Intelligent Robots and Systems* 2016-Nov.C (2016), pp. 3684–3689. ISSN: 21530866. DOI: 10.1109/IROS.2016.7759543.

[186] U. Kim, D.-H. Lee, Y. B. Kim, et al. “A Novel Six-Axis Force/Torque Sensor for Robotic Applications”. In: *IEEE/ASME Transactions on Mechatronics* 22.3 (2017), pp. 1381–1391. DOI: 10.1109/TMECH.2016.2640194.

[187] A. S. Naidu, R. V. Patel, and M. D. Naish. “Low-Cost Disposable Tactile Sensors for Palpation in Minimally Invasive Surgery”. In: *IEEE/ASME Transactions on Mechatronics* 22.1 (2017), pp. 127–137. DOI: 10.1109/TMECH.2016.2623743.

[188] U. Kim, Y. B. Kim, J. So, et al. “Sensorized Surgical Forceps for Robotic-Assisted Minimally Invasive Surgery”. In: *IEEE Transactions on Industrial Electronics* 65.12 (2018), pp. 9604–9613. DOI: 10.1109/TIE.2018.2821626.

[189] D.-Y. Seok, Y. B. Kim, U. Kim, et al. “Compensation of Environmental Influences on Sensorized-Forceps for Practical Surgical Tasks”. In: *IEEE Robotics and Automation Letters* 4.2 (2019), pp. 2031–2037. DOI: 10.1109/LRA.2019.2899217.

[190] A. P. Miller, W. J. Peine, J. S. Son, et al. “Tactile Imaging System for Localizing Lung Nodules during Video Assisted Thoracoscopic Surgery”. In: *Proceedings 2007 IEEE International Conference on Robotics and Automation*. 2007, pp. 2996–3001. DOI: 10.1109/ROBOT.2007.363927.

[191] Y.-J. Lo. “A Novel Three-Axis Capacitive Force Sensor for Robot-Assisted Surgery”. In: *2023 5th International Conference on Control and Robotics (ICCR)*. 2023, pp. 7–10. DOI: 10.1109/ICCR60000.2023.10444861.

[192] N. Gorges, S. Escaida Navarro, D. Göger, et al. “Haptic Object Recognition Using Passive Joints and Haptic Key Features”. In: *2010 IEEE International Conference on Robotics and Automation*. 2010, pp. 2349–2355. DOI: 10.1109/ROBOT.2010.5509553.

[193] A. Schmitz, M. Maggiali, L. Natale, et al. “Touch Sensors for Humanoid Hands”. In: *19th International Symposium in Robot and Human Interactive Communication*. 2010, pp. 691–697. DOI: 10.1109/ROMAN.2010.5598609.

[194] I. Mamaev, D. Kretsch, H. Alagi, et al. “Grasp Detection for Robot to Human Handovers Using Capacitive Sensors”. In: *2021 IEEE International Conference on Robotics and Automation (ICRA)*. 2021, pp. 12552–12558. DOI: 10.1109/ICRA48506.2021.9560970.

[195] H.-K. Lee, J. Chung, S.-I. Chang, et al. “Normal and Shear Force Measurement Using a Flexible Polymer Tactile Sensor With Embedded Multiple Capacitors”. In: *Journal of Microelectromechanical Systems* 17.4 (2008), pp. 934–942. DOI: 10.1109/JMEMS.2008.921727.

[196] D. Göger, H. Alagi, and H. Wörn. “Tactile Proximity Sensors for Robotic Applications”. In: *2013 IEEE International Conference on Industrial Technology (ICIT)*. 2013, pp. 978–983. DOI: 10.1109/ICIT.2013.6505804.

[197] S. Macenski, T. Foote, B. Gerkey, et al. “Robot Operating System 2: Design, Architecture, and Uses in the Wild”. In: *Science Robotics* 7.66 (2022), eabm6074. DOI: 10.1126/scirobotics.abm6074. URL: https://www.science.org/doi/abs/10.1126/scirobotics.abm6074.

[198] U. Kim, Y. B. Kim, D.-Y. Seok, et al. “A Surgical Palpation Probe With 6-Axis Force/Torque Sensing Capability for Minimally Invasive Surgery”. In: *IEEE Transactions on Industrial Electronics* 65.3 (2018), pp. 2755–2765. DOI: 10.1109/TIE.2017.2739681.

[199] I. EOS/ESD Association. *ANSI/ESDA/JEDEC JS-001-2017 - ESDA/JEDEC Joint Standard for Electrostatic Discharge Sensitivity Testing - Human Body Model (HBM) - Component Level*. en. Standard. EOS/ESD Association, Inc., JEDEC Solid State Technology Association, 2017.

[200] T. Mang, G. Böhm, and W. Schima. “Normal Colon”. In: *CT Colonography Atlas: For the Practicing Radiologist*. Ed. by E. Neri, L. Faggioni, and C. Bartolozzi. Berlin, Heidelberg: Springer Berlin Heidelberg, 2013, pp. 1–16. ISBN: 978-3-642-11149-5. DOI: 10.1007/978-3-642-11149-5_1. URL: https://doi.org/10.1007/978-3-642-11149-5_1.

[201] P. R. Slawinski, A. Z. Taddese, K. B. Musto, et al. “Autonomously Controlled Magnetic Flexible Endoscope for Colon Exploration”. In: *Gastroenterology* 154.6 (2018), 1577–1579.e1. ISSN: 0016-5085. DOI: https://doi.org/10.1053/j.gastro.2018.02.037. URL: https://www.sciencedirect.com/science/article/pii/S0016508518303123.

[202] S. Hong, S. Lee, and D.-H. Kim. “Materials and Design Strategies of Stretchable Electrodes for Electronic Skin and its Applications”. In: *Proceedings of the IEEE* 107.10 (2019), pp. 2185–2197. DOI: 10.1109/JPROC.2019.2909666.

[203] G. Bradski. “The OpenCV Library”. In: *Dr. Dobb’s Journal of Software Tools* (2000).

[204] C. **Marzi**, N. Fischer, and F. Mathis-Ullrich. “Biocompatible Soft Material Actuator for Compliant Medical Robots”. In: *Current Directions in Biomedical Engineering* 7.1 (2021), pp. 58–62. DOI: 10.1515/cdbme-2021-1013. URL: https://www.degruyter.com/document/doi/10.1515/cdbme-2021-1013.

[205] G. A. Giacoppo, J. Mayer, J. Hartmann, et al. “Actively Shielded Capacitive Proximity Sensor for Endoscopy”. In: *Current Directions in Biomedical Engineering* 9.1 (2023), pp. 93–96. DOI: 10.1515/cdbme-2023-1024. URL: https://doi.org/10.1515/cdbme-2023-1024.

[206] W. Heiligenberg. “Electrolocation of Objects in the Electric fishEigenmannia (Rhamphichthyidae, Gymnotoidei)”. In: *Journal of comparative physiology* 87.2 (June 1973), pp. 137–164. ISSN: 1432-1351. DOI: 10.1007/BF01352158. URL: https://doi.org/10.1007/BF01352158.

[207] J. R. Smith, E. Garcia, R. Wistort, et al. “Electric Field Imaging Pretouch for Robotic Graspers”. In: *2007 IEEE/RSJ International Conference on Intelligent Robots and Systems*. 2007, pp. 676–683. DOI: 10.1109/IROS.2007.4399609.

[208] C. **Marzi**, T. Prinzen, J. Haag, et al. “Continuous Feature-Based Tracking of the Inner Ear for Robot-Assisted Microsurgery”. In: *Frontiers in Surgery* 8 (2021). ISSN: 2296-875X. DOI: 10.3389/fsurg.2021.742160. URL: https://www.frontiersin.org/articles/10.3389/fsurg.2021.742160.

[209] M. Finocchiaro, T. Banfi, S. Donaire, et al. “A Framework for the Evaluation of Human Machine Interfaces of Robot-Assisted Colonoscopy”. In: *IEEE Transactions on Biomedical Engineering* 71.2 (2024), pp. 410–422. DOI: 10.1109/TBME.2023.3301741.

[210] C. **Marzi**, J. Raczkowsky, and F. Mathis-Ullrich. “Intraoperative Data Acquisition through Visual Sensing of Surgical Workflow”. In: *Tagungsband - 18. Jahrestagung der Deutschen Gesellschaft für Computer- und Roboterassistierte Chirurgie e.V. (CURAC 2019). Hrsg.: O. Burgert*. 18. Jahrestagung der Deutschen Gesellschaft für Computer- und Roboterassistierte Chirurgie e.V. CURAC 2019 (Reutlingen, Deutschland, Sept. 19–21, 2019). Hochschule, 2019, pp. 171–172. ISBN: 978-3-00-063717-9.

[211] C. **Marzi**, A. Wachter, and W. Nahm. “Design of an Experimental Four-Camera Setup for Enhanced 3D Surface Reconstruction in Microsurgery”. In: *Current Directions in Biomedical Engineering* 3.2 (2017), pp. 539–542. DOI: 10.1515/cdbme-2017-0185. URL: https://doi.org/10.1515/cdbme-2017-0185.

[212] J. Fischer, D. Andreas, P. Beckerle, et al. “Vibrational Feedback for a Teleoperated Continuum Robot with Non-contact Endoscope Localization”. In: *Current Directions in Biomedical Engineering* 10.1 (2024), pp. 17–20. DOI: doi:10.1515/cdbme-2024-0105. URL: https://doi.org/10.1515/cdbme-2024-0105.

[213] N. Fischer, C. **Marzi**, K. Meisenbacher, et al. “A Sensorized Modular Training Platform to Reduce Vascular Damage in Endovascular Surgery”. In: *International Journal of Computer Assisted Radiology and Surgery* (2023), pp. 1–9.

[214] G. García, N. Fischer, C. **Marzi**, et al. “Robotic Sensorized Gastroendoscopy with Wireless Single-Hand Control”. In: *Current Directions in Biomedical Engineering* 8.1 (2022), pp. 66–69. DOI: 10.1515/cdbme-2022-0017. URL: https://doi.org/10.1515/cdbme-2022-0017.

[215] T. Prinzen, C. **Marzi**, J. Haag, et al. “Erkennung von Bildmerkmalen im Mikroskopbild für robotisch assistierte Mikrochirurgie: Erste Ergebnisse und Klinische Perspektive”. DE. In: *Laryngorhinootologie* 101.S 02 (May 2022). ISSN: 0935-8943. DOI: 10.1055/s-0042-1747120. URL: https://doi.org/10.1055/s-0042-1747120.

[216] N. Fischer, P. Scheikl, C. **Marzi**, et al. “Flexible Facile Tactile Sensor for Smart Vessel Phantoms”. In: *Current Directions in Biomedical Engineering* 7.1 (2021), pp. 87–91. DOI: 10.1515/cdbme-2021-1019. URL: https://doi.org/10.1515/cdbme-2021-1019.

[217] C. Kunz, P. Maurer, F. Kees, et al. “Infrared Marker Tracking with the HoloLens for Neurosurgical Interventions”. In: *Current Directions in Biomedical Engineering* 6.1 (2020), p. 20200027. DOI: 10.1515/cdbme-2020-0027. URL: https://doi.org/10.1515/cdbme-2020-0027.

[218] J. Schmid, C. **Marzi**, V. Lupici-Baltzer, et al. “Influence of Thin Non-Conducting Layers in Electromagnetic Body-phantoms for Imaging Radar”. In: *Biomedical Engineering - Biomedizinische Technik* 59 (2014), S612–S615.

Acronyms

ADC Analog Digital Converter.

AI Artificial Intelligence.

CAD Computer Aided Design.

CE Conformité Européenne.

CR continuum robot.

CT Computed Tomography.

DOF degree of freedom.

EAP Electroactive Polymer.

EDG Esophago-gastro-duodenoscopy.

ESD Electrostatic Discharge.

FBG Fiber-Bragg-Grating.

FDA Food and Drug Administration.

FTS force-torque sensor.

HRI Human Robot Interaction.

I2C Inter-Integrated Circuit.

ICRA International Conference on Robotics and Automation.

LED light emitting diode.

MFE Magnetic Flexible Endoscope.

MIS minimally invasive surgery.

MRI Magnetic Resonance Imaging.

NiTi Nickle Titanium Alloy.

NOTES Natural Orifices Translumenal Endoscopic Surgery.

OCT Optical Coherence Tomography.

OR operation room.

PCB Printed Circuit Board.

PWM pulse width modulation.

RAL Robotics and Automation Letters.

RCM remote center of motion.

ROS Robot Operating System.

SLA stereolithography.

SLAM Simultaneous Localization and Mapping.

SMA Shape-Memory Alloy.

SMD Surface-Mounted Device.

SMP Shape-Memory Polymer.

TCP Tool Center Point.

TMRB IEEE - Transaction on Medical Robotics and Bionics.

TOF Time-of-Flight.

urdf Unified Robot Description Format.

US Ultrasound.

USB Universal Serial Bus.

µC microcontroller.

List of Figures

List of Tables

Appendix

A Summary of Further Publications

As a reference, this section provides summaries of the author's further publications which do not directly relate to the topic of this thesis but to the general field of research of medical robotics. As a summary, the publications' abstracts and summarizing graphics are provided.

A.1 Continuous Feature-Based Tracking of the Inner Ear for Robot-Assisted Microsurgery

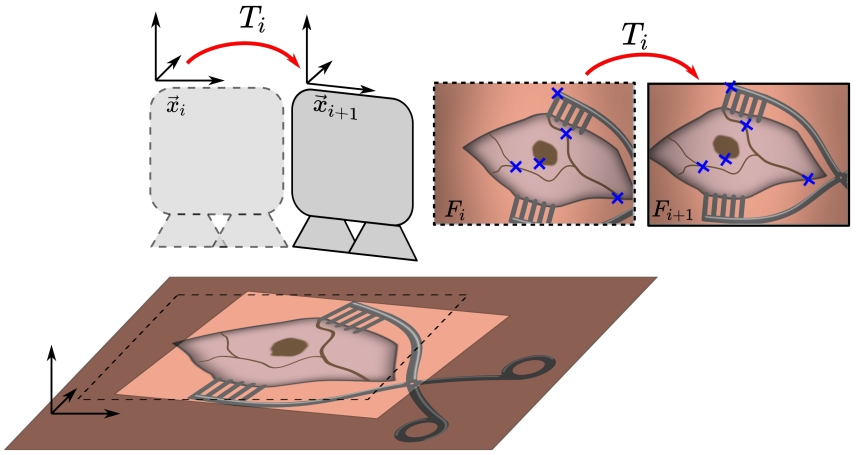

Figure A.1 – Overview of the method presented in [208]. A surgical microscope's displacement is estimated by detecting features in successive images.

Robotic systems for surgery of the inner ear must enable highly precise movement in relation to the patient. To allow for a suitable collaboration between surgeon and robot, these systems should not interrupt the surgical workflow and integrate well in existing processes. As the surgical microscope is a standard tool, present in almost every microsurgical intervention and due to it being in close proximity to the situs, it is predestined to be extended by assistive robotic systems. For instance, a microscope-mounted laser for ablation. As both, patient and microscope are subject to movements during surgery, a well-integrated robotic system must be able to comply with these movements. To solve the problem of online registration of an assistance system to the situs, the standard of care often utilizes marker-based technologies, which require markers being rigidly attached to the patient. This not only requires time for preparation but also increases invasiveness of the procedure and the line of sight of the tracking system may not be obstructed. This work aims at utilizing the existing imaging system for detection of relative movements between the surgical microscope and the patient. The resulting data allows for maintaining registration. Hereby, no artificial markers or landmarks are considered but an

approach for feature-based tracking with respect to the surgical environment in otology is presented. The images for tracking are obtained by a two-dimensional RGB stream of a surgical microscope. Due to the bony structure of the surgical site, the recorded cochleostomy scene moves nearly rigidly. The goal of the tracking algorithm is to estimate motion only from the given image stream. After preprocessing, features are detected in two subsequent images and their affine transformation is computed by a random sample consensus (RANSAC) algorithm. The proposed method can provide movement feedback with up to 93.2 µm precision without the need for any additional hardware in the operating room or attachment of fiducials to the situs. In long term tracking, an accumulative error occurs.

C. **Marzi**, T. Prinzen, J. Haag, T. Klenzner, and F. Mathis-Ullrich. "Continuous Feature-Based Tracking of the Inner Ear for Robot-Assisted Microsurgery". In: *Frontiers in Surgery* 8 (2021). ISSN: 2296-875X. DOI: 10.3389/fsurg.2021.742160. URL: https://www.frontiersin.org/articles/10.3389/fsurg.2021.742160

A.2 Biocompatible Soft Material Actuator for Compliant Medical Robots

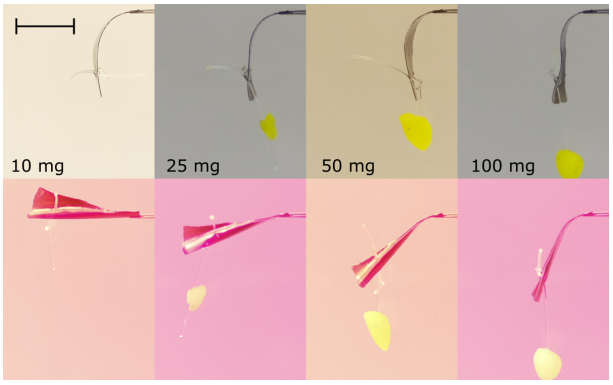

Figure A.2 – The solid state actuator presented in [204]. A graphene oxide enriched silicone elastomer is actuated by illumination with infrared light. The upper series shows the actuator's passive state, the lower its actuated state. From left to right the load is increased.

Robots from material-based actuators offer high potential for small-scale robots with abilities hardly achievable by classical methods like electric motors. Besides excellent scaling to minimally invasive systems, allowing for omission of metallic components, such robots can be applied in imaging modalities such as MRI or CT. To allow for higher accessibility in this field of research, a facile method for fabrication of such soft actuators was developed. It comprises only two materials: graphene oxide and silicone elastomer. The facile fabrication method does not require specialized equipment. The resulting actuator is biocompatible and controllable by light mediated heat. The bending motion can be controlled by the intensity of applied infrared light and the actuator was experimentally shown to move five times its own weight. Thus, providing capabilities for a medical soft robotic actuator.

C. **Marzi**, N. Fischer, and F. Mathis-Ullrich. "Biocompatible Soft Material Actuator for Compliant Medical Robots". In: *Current Directions in Biomedical Engineering* 7.1 (2021), pp. 58–62. DOI: 10.1515/cdbme-2021-1013. URL: https://www.degruyter.com/document/doi/10.1515/cdbme-2021-1013

B Disclaimer on the Usage of (AI) Tools

Guidelines: At the time of the writing of this thesis, the usage of generative Artificial Intelligence (AI) in the creation of a thesis is part of an ongoing discussion. Various institutions engage in creating guidelines for the usage of generative AI in copyright and scientific writing but no general consensus or widely accepted standard is present at the time of the writing of this thesis. For this thesis, AI tools were used with the aim of improving the thesis but without the introduction of invalidated content or content not created by the author. To conform to the scientific best practice of disclosing all used means and methods, the following statement serves to clarify which tools were used and how they contributed to the content of this thesis. All content not listed here was created only by the author himself without the help of any AI tools. No content generated by any AI tools is directly copied into this thesis. Any generated content was critically reviewed and only served as an input for content created by the author.

The following publications served as major guidelines. Concerning a work as this thesis, they agree on the acceptance of the usage of (generative) AI tools on the condition, that generated context is thoroughly reviewed and explicitly annotated when published in direct form.

- The KIT's *Center for Technology-Enhanced Learning* refers to the guidelines published by the Hochschulforum Digitalisierung (HFD): *Leitlinien zum Umgang mit generativer KI*, Jens Tobor (HFD/CHE), 07.02.2024, last accessed on: 25.05.2024.
- The German Federal Ministry of Education and Research (BMBF) references guidelines published by the European Commission: *Living guidelines on the responsible use of generative AI in Research*, 20.03.2024, last accessed 25.05.2024
- The IEEE's Submission and Peer Review Policies provide a paragraph on *Guidelines for Artificial Intelligence (AI)-Generated Text*, last accessed on: 25.05.2024.

Graphics: All images included in this thesis either designate their source in a citation or, if not annotated, were entirely created by the author by editing self-made photographs and renders or creating digital drawings using the following (non-AI) tools:

- GIMP (v2.10.38) for editing of pixel graphics, photographs, and renders.
- Inkscape (v1.3.2) for the creation of vector graphics, sketches, and annotations in photos.
- Autodesk Inventor 2024 for CAD designs of parts, and 3D rendered images.
- Altium Designer 24 and KICAD (v7.0.10) for CAD of PCBs and creation of rendered images of circuits.

Images annotated as *adapted* from a cited source were edited by the author as well using the listed tools, but the image content strongly follows the cited source. This thesis contains no images or parts of images that were generated or edited by generative AI tools.

Text Structure and Wording: The thesis structure, the title of chapters and sections, and sentence variations were discussed with the Chatbot by OpenAI (ChatGPT v3.5). This was done to gain ideas on possible improvements of the wording and find more precise terms and definitions.

Proofreading and Translation: This thesis was typeset in Latex using the online editor by Overleaf. Suggestions from Overleaf's built-in proofreading tool were taken over after review. Additionally, proofreading was conducted by the online tool provided by Grammarly. Text format, grammar, and spelling were kept in conformity with the Chicago Manual of Style (Edition 17). For help with composing an English text, the online translator `https://dict.leo.org/englisch-deutsch/` was utilized to provide German-to-English translation for single words.

C List of Publications

C.1 First Author Publications

- C. **Marzi**, M. Themistocli, B. Hein, and F. Mathis-Ullrich. "Proximity Servoed Minimally Invasive Continuum Robot for Endoscopic Interventions". In: *IEEE Transactions on Medical Robotics and Bionics* (2024), pp. 1–1. DOI: 10.1109/TMRB.2024.3464127
- C. **Marzi**, F. Buck, and F. Mathis-Ullrich. "Continuum Robot Actuation by a Single Motor per Antagonistic Tendon Pair: Workspace and Repeatability Analysis". In: *at - Automatisierungstechnik* 71.7 (2023), pp. 528–536. DOI: 10.1515/auto-2023-0066. URL: https://doi.org/10.1515/auto-2023-0066
- C. **Marzi**, H. Alagi, O. Rau, J. Hampe, J. G. Korvink, B. Hein, and F. Mathis-Ullrich. "Capacitive Proximity Sensor for Non-Contact Endoscope Localization". In: *2022 International Conference on Robotics and Automation (ICRA)*. May 2022, pp. 9614–9620. DOI: 10.1109/ICRA46639.2022.9811734
- C. **Marzi**, T. Prinzen, J. Haag, T. Klenzner, and F. Mathis-Ullrich. "Continuous Feature-Based Tracking of the Inner Ear for Robot-Assisted Microsurgery". In: *Frontiers in Surgery* 8 (2021). ISSN: 2296-875X. DOI: 10.3389/fsurg.2021.742160. URL: https://www.frontiersin.org/articles/10.3389/fsurg.2021.742160
- C. **Marzi**, N. Fischer, and F. Mathis-Ullrich. "Biocompatible Soft Material Actuator for Compliant Medical Robots". In: *Current Directions in Biomedical Engineering* 7.1 (2021), pp. 58–62. DOI: 10.1515/cdbme-2021-1013. URL: https://www.degruyter.com/document/doi/10.1515/cdbme-2021-1013
- C. **Marzi**, J. Raczkowsky, and F. Mathis-Ullrich. "Intraoperative Data Acquisition through Visual Sensing of Surgical Workflow". In: *Tagungsband - 18. Jahrestagung der Deutschen Gesellschaft für Computer- und Roboterassistierte Chirurgie e.V. (CURAC 2019). Hrsg.: O. Burgert*. 18. Jahrestagung der Deutschen Gesellschaft für Computer- und Roboterassistierte Chirurgie e.V.. CURAC 2019 (Reutlingen, Deutschland, Sept. 19–21, 2019). Hochschule, 2019, pp. 171–172. ISBN: 978-3-00-063717-9
- C. **Marzi**, A. Wachter, and W. Nahm. "Design of an Experimental Four-Camera Setup for Enhanced 3D Surface Reconstruction in Microsurgery". In: *Current Directions in Biomedical Engineering* 3.2 (2017), pp. 539–542. DOI: 10.1515/cdbme-2017-0185. URL: https://doi.org/10.1515/cdbme-2017-0185

C.2 Co-Author Publications

- J. Fischer, D. Andreas, P. Beckerle, F. Mathis-Ullrich, and C. **Marzi**. "Vibrational Feedback for a Teleoperated Continuum Robot with Non-contact Endoscope Localization". In: *Current Directions in Biomedical Engineering* 10.1 (2024), pp. 17–20. DOI: doi:10.1515/cdbme-2024-0105. URL: https://doi.org/10.1515/cdbme-2024-0105
- N. Greenidge, J. Martin, C. **Marzi**, D. Chathuranga, B. Scaglioni, K. L. Obstein, F. Mathis-Ullrich, and P. Valdastri. "Restoring the Sixth Degree of Freedom in the Robotic Manipulation of Mesoscale Magnetic Devices Using the Oloid Shape". In: *IEEE Robotics and Automation Letters* (2024). Currently prepared for publication.

- N. Fischer, C. **Marzi**, K. Meisenbacher, A. Kisilenko, T. Davitashvili, M. Wagner, and F. Mathis-Ullrich. "A Sensorized Modular Training Platform to Reduce Vascular Damage in Endovascular Surgery". In: *International Journal of Computer Assisted Radiology and Surgery* (2023), pp. 1–9
- G. García, N. Fischer, C. **Marzi**, and F. Mathis-Ullrich. "Robotic Sensorized Gastroendoscopy with Wireless Single-Hand Control". In: *Current Directions in Biomedical Engineering* 8.1 (2022), pp. 66–69. DOI: 10.1515/cdbme-2022-0017. URL: https://doi.org/10.1515/cdbme-2022-0017
- T. Prinzen, C. **Marzi**, J. Haag, F. Mathis-Ullrich, J. Schipper, and T. Klenzner. "Erkennung von Bildmerkmalen im Mikroskopbild für robotisch assistierte Mikrochirurgie: Erste Ergebnisse und Klinische Perspektive". DE. in: *Laryngorhinootologie* 101.S 02 (May 2022). ISSN: 0935-8943. DOI: 10.1055/s-0042-1747120. URL: https://doi.org/10.1055/s-0042-1747120
- N. Fischer, P. Scheikl, C. **Marzi**, B. Galindo-Blanco, A. Kisilenko, B. P. Müller-Stich, M. Wagner, and F. Mathis-Ullrich. "Flexible Facile Tactile Sensor for Smart Vessel Phantoms". In: *Current Directions in Biomedical Engineering* 7.1 (2021), pp. 87–91. DOI: 10.1515/cdbme-2021-1019. URL: https://doi.org/10.1515/cdbme-2021-1019
- C. Kunz, P. Maurer, F. Kees, P. Henrich, C. **Marzi**, M. Hlaváč, M. Schneider, and F. Mathis-Ullrich. "Infrared Marker Tracking with the HoloLens for Neurosurgical Interventions". In: *Current Directions in Biomedical Engineering* 6.1 (2020), p. 20200027. DOI: 10.1515/cdbme-2020-0027. URL: https://doi.org/10.1515/cdbme-2020-0027
- J. Schmid, C. **Marzi**, V. Lupici-Baltzer, M. Jalilvand, and O. Doessel. "Influence of Thin Non-Conducting Layers in Electromagnetic Body-phantoms for Imaging Radar". In: *Biomedical Engineering - Biomedizinische Technik* 59 (2014), S612–S615